AN ABSTRACT OF THE THESIS OF

Sangmoon Park for the degree of Doctor of Philosophy in Chemistry presented on July 22, 2002.

Title: Synthesis and Study of Oxides and Chalcogenides: Thin Films and Crystals.

Abstract approved: Redacted for privacy

Douglas A. Keszler

Several types of solid-state inorganic materials are prepared and characterized. By using the SILAR (Successive Ionic Layer Adsorption and Reaction) deposition method in conjunction with hydrothermal dehydration both low-temperature deposition and crystallization of oxide thin films are achieved. Various aspects of new transparent p-type materials are studied by examining both powders and thin films. Delafossite type compounds, $CuMO_{2+\delta}$ (M=Ga, Sc, In), are synthesized by unique methods, yielding single-phase materials. The conductivity, mobility, and carrier concentration in $BaCu_2S_2$ thin films are described and p-type conductivity in the wide band-gap sulfide fluoride, BaCuSF, is examined. Structural and conducting properties of the various polymorphs of In_2Se_3 and the related structure of Sb_2Te_2Se are considered. Structural characterization and cation ordering in Langasite derivatives, $La_3SnGa_5O_{14}$ and $La_3SnGa_3Al_2O_{14}$, is described. Finally, selected aspects of the synthesis, structural characterization, and

luminescence properties of $Y_3(SiO_4)_2Cl$, $Mn:Zn_2SiO_4$, and $Eu:Y_6WO_{12}$ are summarized.

Synthesis and Study of Oxides and Chalcogenides:

Thin Films and Crystals

by

Sangmoon Park

A THESIS

Submitted to

Oregon State University

In partial fulfillment of

The requirements for the

Degree of

Doctor of Philosophy

Completed July 22, 2002

Commencement June 2003

Doctor of Philosophy thesis of Sangmoon Park presented on July 22, 2002.

APPROVED:

Redacted for privacy

Major Professor, representing Chemistry

Redacted for privacy

Chair of the Department of Chemistry

Redacted for privacy

Dean of the Graduated School

I understand that my thesis will become part of the permanent collection of Oregon State University libraries. My signature below authorizes release of my thesis to any reader upon request.

Redacted for privacy

Sangmoon Park, Author

ACKNOWLEDGMENTS

I am particularly thankful to my major professor, Douglas A. Keszler for supplying endless great ideas, enthusiasm, encouragement, and support during my graduate work.

I would like to extend my appreciation to my Ph.D. committee members and former committee members: Dr. Arthur W. Sleight, Dr. Philip R. Watson, Dr. Janet Tate, Dr. Joseph J. Karchesy, Dr. Michael M. Lerner, and Dr. W. M. Hetherington for their time and commitment to my Ph.D. program.

I especially have to thank Dr. John F. Wager and Dr. Tate Janet for supporting in my research and allowing me to work with their research groups in ECE and Physics. I am grateful to the past and present members of Keszler Group, Wager Group, Sleight Group, and Tate Group for their many useful discussions and help: Dr. Ki-Seog Chang, Dr. Dong Li, Dr. Greg Peterson, Dr. Judith Kissick, Dr. Ben Clark, Dr. Jennifer Stone, Dr. Ning Ye, Candice Pike, Jeremy Anderson, Mike Hruschka, Cheol-hee Park, Mike Shoemaker, Melinda M. Valencia, Randy L. Hoffman, Jeffrey P. Bender, Dr. Beau Baukol, Hai Chang, Dr. Uma Sitharaman, Jun Li, Dr. M. K. Jayaraj, Dr. Hiroshi Yanagi, Matthew F. Price. I also thank Dr. Gregory S. Herman, Dr. David M. Schut, Dr. Alex Yokochi and Chemistry support staff at OSU for help and support. I have also made new friends including George Law, Wei Yang and people in KPCC.

I would like to acknowledge my mother, Kyung Hee Lee, father, Young Sik Park, and all family for their love and encouragement to continue my education. Finally, I want to say thank and love my wife, Eil Ran Roh-Park, my daughter, Rachel Eugene Park, and my baby in my wife (I really want meet you).

CONTRIBUTION OF AUTHORS

This work would not have been possible without the help of Dr. Douglas A. Keszler and several collaborators. These collaborators and their respective contributions are given here. Gregory S. Herman provide Electron Micrograph of ZrO_2 and all substrates from Hewlett-Packard Company, Jeffrey P. Bender and John F. Wager provided the green emission photo of $Mn{:}Zn_2GeO_4$, and Thomas A. Reynolds in Rey Tech Corporation contributed in Chapter 2. Melinda M. Valencia, Randy L. Hoffman, and Dr. John F. Wager contributed in Chapter 4, 5, and 7. Cheol-Hee Park, Hiroshi Yanagi, and Dr. Tate Janet collaborated in Chapter 6. Dr. Alex Yokochi assisted the structural refinements in Chapter 9.

TABLE OF CONTENTS

Page

TABLE OF CONTENTS (continued)

TABLE OF CONTENTS (continued)

TABLE OF CONTENTS (continued)

TABLE OF CONTENTS (continued)

LIST OF FIGURES

LIST OF FIGURES (continued)

LIST OF FIGURES (continued)

LIST OF FIGURES (continued)

LIST OF FIGURES (continued)

LIST OF TABLES

Table Page

SYNTHESIS AND STUDY OF OXIDES AND CHALCOGENIDES: THIN FILMS AND CRYSTALS

CHAPTER 1

INTRODUCTION

Within the field of solid-state inorganic materials, many opportunities exist to synthesize new materials and to examine their physical and chemical properties. The original intent of the work described here was to prepare and study new piezoelectric materials with an emphasis on developing simple models for understanding acoustic-wave properties. As time passed, greater effort was directed to the study of luminescent materials and finally thin films, where a new deposition procedure was developed and numerous materials were characterized. While a breadth of materials has been examined, there extends through the work the common themes of synthesis and the use of structure-property relationships for the development of new materials.

The preparation of thin films has been a major aspect of this work. Thin-film deposition methods of evaporation and sputtering are two of the more important methods of physical vapor deposition (PVD).[1] Chemical vapor deposition (CVD), the process of chemically reacting volatile compounds, is also widely used as a thin-film deposition method.[1] These methods, however, have high capital equipment and maintenance costs, high processing temperatures and vacuum pressures, and limited flexibility in the choice of substrates. The thin-film deposition methods from aqueous solutions[2-6] such as successive ion layer adsorption and reaction (SILAR), chemical bath deposition (CBD), and spin coating, have been developed as simple, inexpensive, low temperature, and atmospheric-pressure deposition processes, producing in some cases films of purity and homogeneity comparable to those achieved with PVD and CVD. For many applications, crystalline films are required, but in most cases as-deposited films are amorphous or rich in defects. Crystallization of such films typically requires a high-temperature anneal. In previous work,[7] the method of precipitation and hydrothermal dehydration[8] was developed to obtain a variety of crystalline oxide powders at low temperatures ($T < 473$ K). As described in Chapter 2, this technique has been extended to the production of oxide thin films by using the SILAR-deposition method in conjunction with hydrothermal dehydration to provide a procedure for achieving both low-temperature deposition and crystallization.

The production of invisible electronic circuits[9] for applications in optoelectronic devices requires materials having high transparency across the visible and infrared regions and high conductivity, both p- and n-type. Sn-doped In_2O_3 and Al-doped ZnO are well known n-type conductors having good optical transparency (~ 90 %), high mobility (~ 20 cm^2/Vs), and high conductivity (~3000 S/cm). p-Type conductors have been widely studied following a report on $CuAlO_2$ thin-film fabrication and characterization in 1997.[10] Up to now, transmission in the visible for p-type transparent conductors has been around 80 %, but reported conductivity (~ 1 S/cm) and mobility (~ 0.5 cm^2/Vs) values are much lower than those of the n-type conductors. The work detailed in Chapters 3, 4, 5, and 6 addresses various aspects of the development of new transparent p-type materials, extending from the development of synthesis methods for delafossite oxides to the identification of new wide band-gap chalcogenide fluoride conductors. This work on semiconductors has been extended in Chapter 7 to the examination of the structural and conducting properties of the various polymorphs of In_2Se_3 and the related structure of Sb_2Te_2Se.

Piezoelectric materials[11-13] such as quartz and lead zirconium titanate are used in acoustic-wave devices. Langasite, $La_3Ga_5SiO_{14}$ (LGS), is a relatively new piezoelectric material that exhibits better thermal stability, piezoelectric moduli, electromechanical coupling coefficients, and lower signal losses than quartz. LGS is a disordered material, and it has been proposed that acoustic losses could be minimized and mechanical properties improved by forming ordered derivatives. In Chapter 8, the structural characterization of an ordered Langasite structure type is described.

For improving colors (green, blue, red) and our understanding of luminescent materials for lighting and display technologies, many different activator host combinations can be synthesized and studied. In Chapter 9 and 10, selected aspects of luminescent properties of a silicate chloride and two oxides are summarized.

The remainder of this chapter provides a summary of some of the important concepts and techniques that have been used in developing the subjects of the ensuing chapters, which comprise the main body of the work.

SUCCESSIVE IONIC LAYER ADSORPTION AND REACTION (SILAR) DEPOSITION[2-6]

The distinguishing characteristics of the SILAR deposition method are a small-capital investment and capabilities for low-temperature processing, batch processing, monolayer manipulation, and room-pressure operation.

Deposition Mechanism

SILAR deposition is simply a controlled process for achieving precipitation at a surface. In its simplest form, only two salt solutions are required for an experiment. Mixing these solutions must produce a precipitate, which is to become the thin film. A process is generally classified as a SILAR deposition, if the film is formed by the sequential addition of individual layers of complexed ions. A water-insoluble thin-film of C_mA_n, for example, is grown on a substrate by reaction of cation $m[CL_p]^{n+}$ and anion $n[AL'_q]^{m-}$, where L_p and L'_q are ligands. The overall reaction follows.

$$m[CL_p]^{n+} + n[AL'_q]^{m-} \rightarrow C_mA_n \downarrow + mpL + nqL'$$

A schematic and explanation of the SILAR deposition process for ZnS, as an example, are summarized in Figure 1.1 and Table 1.1, respectively. This process neglects the hydrolysis of S^{2-}

$$S^{2-}\,(aq) + H_2O\,(l) \Leftrightarrow HS^-\,(aq) + OH^-\,(aq)$$

which actually interferes with the precipitation of ZnS.

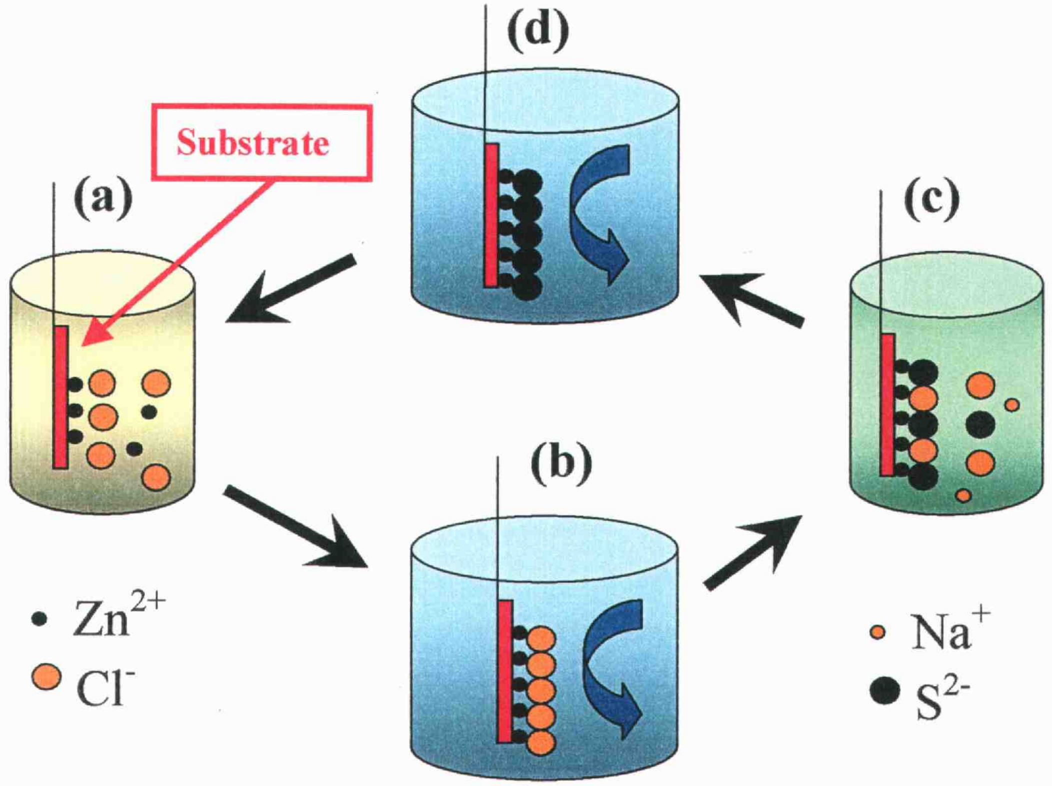

Figure 1.1. Drawing of SILAR deposition mechanism for ZnS.

Table 1.1. Process of SILAR deposition for ZnS.

(a) 1st Step: Cation (Zn^{2+}) Adsorption	The cation constituent of the thin-film material is adsorbed on the surface of the substrate, forming an electrical double layer capped by a diffusion layer. The adsorption of the cations can occur if the solution pH is above the substrate isoelectric point. A positive electrokinetic potential yields a large cation surface coverage. The heterogenous reaction between solid (substrate) and liquid (cation solution, zinc precursor solution) can be obtained by adjusting the solution pH to ~ 5.
(b) 2nd Step: Rinsing	The surface is rinsed with purified water to remove un-adsorbed Zn^{2+} and Cl^- ions in the diffusion layer, so only one tightly adsorbed layer stays on the substrate.
(c) 3rd Step: Anion (S^{2-}) Reaction	The anions of the solution diffuse to the surface, react with the adsorbed cations of the inner layer, and ideally form the water-insoluble precipitate ZnS.
(d) 4th Step: Rinsing	The substrate is again rinsed to remove un-adsorbed Na^+, S^{2-}, and Cl^- ions in the diffusion layer, so only a tightly adsorbed ZnS layer remains on the substrate.
Steps (a)-(d) are sequentially repeated many times to achieve a desired film thickness. **Reaction: $ZnCl_2$ (aq) + Na_2S (aq) → ZnS (s) + 2NaCl (aq)**	

In SILAR deposition, thin-film thickness can be controlled by cycle numbers and by rinsing times. Figure 1.2 is a plot of film thickness vs. rinsing time for deposition of zirconium hydroxide hydrate on glass. 0.2 M $ZrOCl_2{\cdot}8H_2O$ and 0.2 M NaOH were used as the salt solutions. The immersion time in the salt solutions was set at 10 s with rinsing times of 10, 30, 60, 90, and 180 s. The number of cycles for each rinsing time was 150. The thickness of the films decreased from 2000 to 200 nm up to and following a rinse time of 60 s. At this time and beyond, it is assumed that the deposition process is occurring at the ion-layer level.

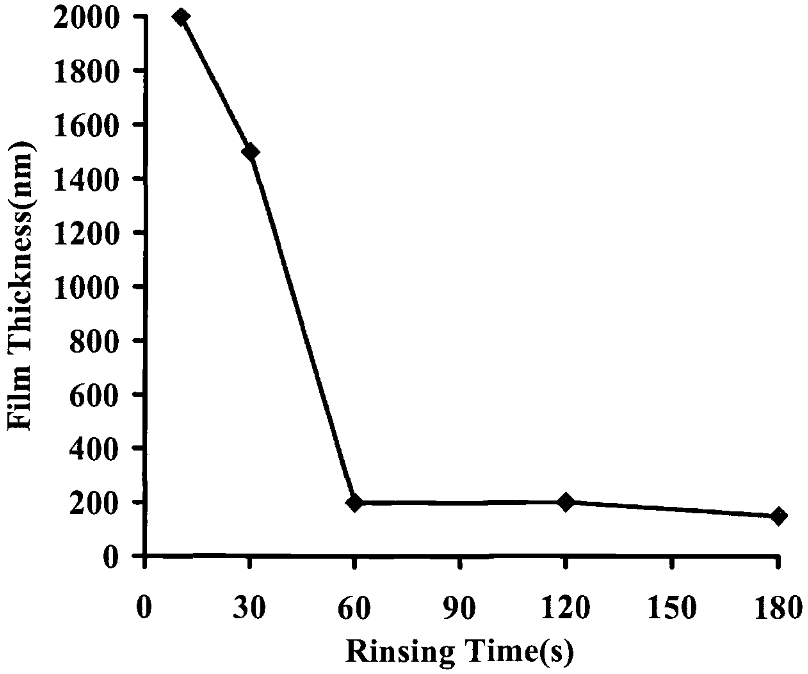

Figure 1.2. Film thickness vs rinsing time for deposition of ZrO_2 on glass.

In this work, ion-layer deposition with rinse times as short as 10 s has been achieved by using a mechanical stirring system. Laminar flow regions providing smooth substrate coverage have been identified in the bath. Salt solution pH and concentration are also important parameters in controlling film thickness and quality.

SILAR Equipment

A photograph of the SILAR deposition system is given in Figure 1.3. The system comprises a Gilson 223 XYZ robot, two or more salt solutions, and a rinse bath with mechanical stirring capabilities. The XYZ robot arm moves the substrate to the appropriate X and Y positions of the solutions or rinsing vessel and then dips it in the Z direction for appropriate immersion and rinsing times. The salt solutions are contained in 40-mL beakers and the rinse vessel is a 2-L plastic container. The pH of the salt solutions is set before each run. Water in the rinse bath is continuously recirculated through a Millipore Academic Milli-Q purification system at a rate of 1.5 L/min, providing a constant resistivity of 18.2 MΩ cm.

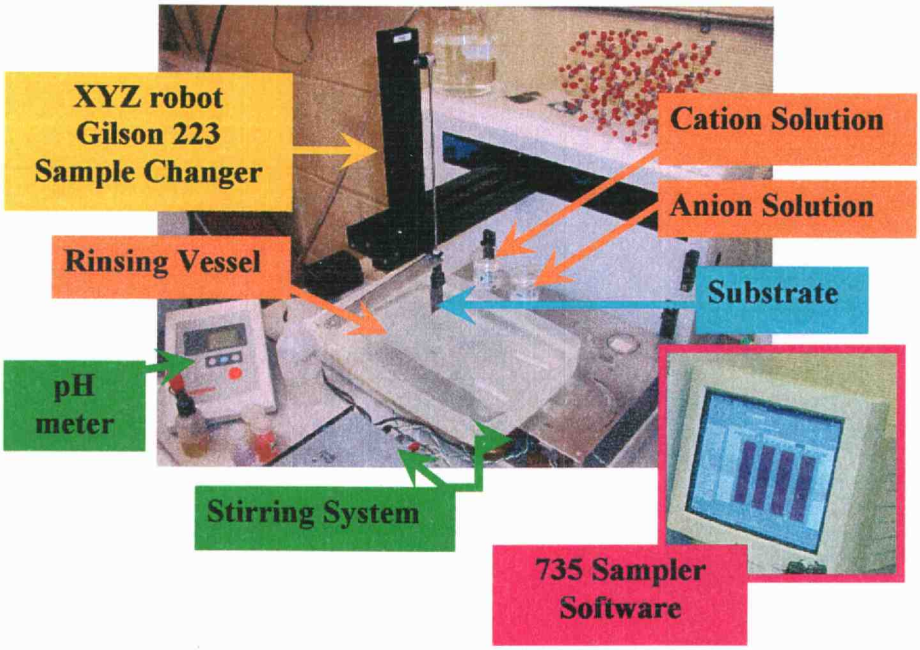

Figure 1.3. Photograph of the SILAR deposition equipment.

THIN-FILM ANNEALING TECHNIQUES

To form highly crystalline films from as-deposited material, some type of annealing method must be used. Hydrothermal dehydration, rapid-thermal annealing (RTA), and furnace annealing methods have been used in this research.

Hydrothermal Dehydration and Hydrothermal Annealing[7-8]

High-purity, homogenous, fine crystalline oxide powders can be conveniently obtained at low temperatures by hydrothermal dehydration of precipitates. The hydrothermal-dehydration process provides nucleation and modest grain growth in transforming an amorphous material into a crystalline solid. From the hydrothermal dehydration, the porous thin films such as ZrO_2 and CeO_2 having nanoscale particles can be produced. In previous work, a fine crystalline Zn_2SiO_4 powder was prepared from the precipitate formed on mixing $ZnSO_4 \cdot H_2O$ and Na_4SiO_4 aqueous solutions followed by hydrothermal dehydration in a Teflon-lined, high-pressure reaction vessel (Parr Instruments) at 473 K. As shown in this work, the hydrothermal-dehydration process leads to production of nanoscale particles for films such as ZrO_2 and CeO_2. A simple and effective method for low-temperature crystallization and grain growth has also been demonstrated by using hydrothermal annealing on amorphous $Mn:Zn_2GeO_4$ thin films. From the application of the hydrothermal-annealing procedure, dense and large grains having microscale particles can be produced. Zn_2GeO_4 exhibits a small solubility in H_2O at elevated temperatures, so the amorphous film crystallizes following hydrothermal treatment. It results in crystalline grain sizes approaching the complete thickness of the film, ~ 1 μm. Figure 1.4 shows an atomic-force-microscopic (AFM) image of such a Mn:Zn_2GeO_4 film on glass. The emission of this film, hydrothermally annealed at 475 K for 2h, is more than four times brighter than a film that has been furnace annealed at 925 K for 2 h. Clearly, one of the continuing challenges in the application of hydrothermal methods to the preparation of useful films will be the development of methods for promoting grain growth and densification of a number of different oxides.

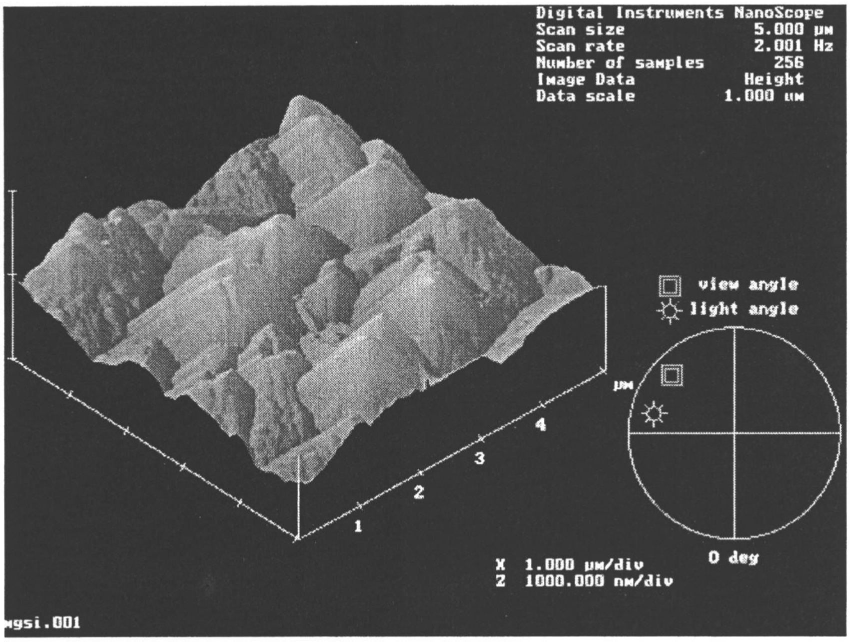
Digital Instruments NanoScope
Scan size 5.000 µm
Scan rate 2.001 Hz
Number of samples 256
Image Data Height
Data scale 1.000 um
X 1.000 µm/div
Z 1000.000 nm/div

Figure 1.4. Atomic force micrograph of Mn:Zn_2GeO_4 on glass.

Rapid Thermal Annealing (RTA)[14]

Rapid thermal annealing is an important technique for promoting grain growth of films that have been deposited on substrates exhibiting limited thermal stability. The technique has been applied to annealing the p-type materials $BaCu_2S_2$ and Sb_2Te_2Se as well as the n-type material In_2Se_3:I. The computer programmable RTA system is able to increase temperature at 300 K/s, hold for 3 ~ 5 minutes and then cool down at a fast rate. Each processing run lasts ~ 20 min and can be done under a variety of gas atmospheres.

Furnace Annealing

Furnace anneals can be done in a standard high-temperature furnace in air or in a tube furnace under a controlled atmosphere. This method is usually used instead of RTA when a longer annealing time is required. In this work, BaCuSF thin films, for example, have been prepared in a tube furnace by heating BaF_2/Cu films under flowing H_2S (g) for 3 h. As noted previously, the oxide thin film of Mn:Zn_2GeO_4 on glass can be annealed and crystallized by heating in air for 2 h at 925 K.

PHYSICAL VAPOR DEPOSITION[1,14,15]

For fabrication of p- or n-type thin films, the physical-vapor-deposition methods of sputtering, thermal evaporation, and electron beam evaporation were used. Laboratory facilities for these deposition processes are located in the Departments of Electrical & Computer Engineering (ECE) and Physics at Oregon State University.

Sputtering Deposition

One of the more common techniques of physical vapor deposition is sputtering. This method has been used for fabrication of transparent p-type conducting $BaCu_2S_2$ thin films. The schematic process of sputtering deposition is shown in Figure 1.5. Bombarding ions, generally of an inert gas, produced by a radio-frequency (RF) glow discharge collide with the atoms on the surface of the target with a high kinetic energy. Atoms are sputtered from the target, move across the chamber, and then deposit on the substrate surface. Following optimization of process variables such as target composition, substrate temperature, and deposition rate, high quality stoichiometric films can be produced.

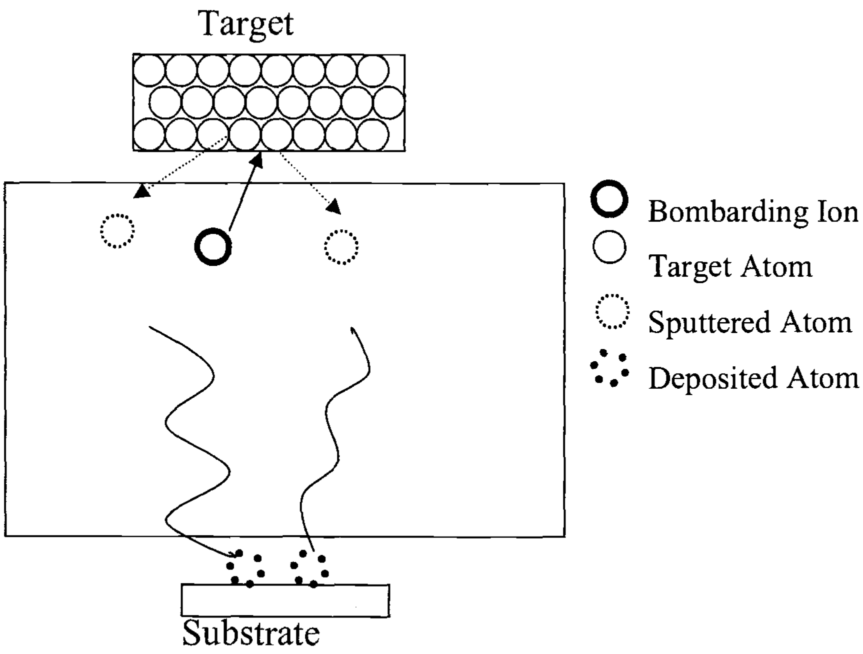

Figure 1.5. The depiction of the sputtering process.

Thermal Evaporation

Thermal evaporation is conceptually the simplest technique of PVD (Figure 1.6). We have used this method for fabrication of p-type BaCuSF, Sb_2Te_2Se, and n-type In_2Se_3:I thin films. Pellets or powders in ceramic boats can be used as a source of materials. The pressure in the vacuum chamber is usually set from 10^{-5} to 10^{-6} torr. The transparent p-type BaCuSF thin film discussed in this work was prepared by thermal evaporation of BaF_2 and Cu powders followed by an anneal under flowing $H_2S(g)$. In principle, by using multiple sources, stoichiometric control can be attained. We have found it to be difficult to achieve highly reproducible results with this method.

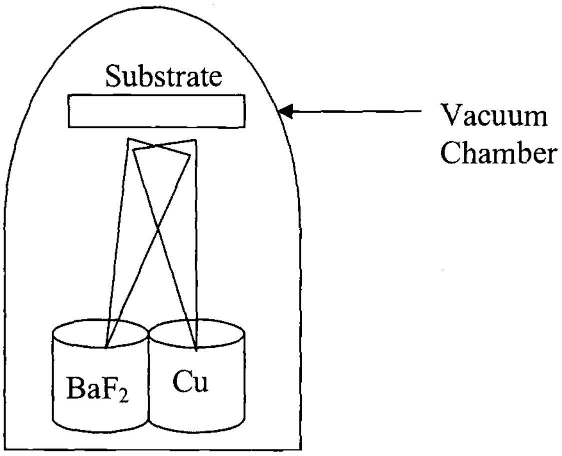

Figure 1.6. The schematic process of thermal evaporation.

Electron Beam Evaporation (EBE)

In electron beam evaporation, high-energy electrons impact a solid surface, forming a vapor. The gas molecules traverse the vacuum chamber and deposit on the substrate surface. The method has been successfully used at Oregon State University to deposit binary sulfide materials such as SrS, ZnS, BaS, and CaS. The advantages of electron-beam evaporation are its fast turnaround time, high deposition rates, and ease in producing pressed-pellet evaporation targets. We have attempted to fabricate $BaCu_2S_2$ films with this method, but we failed to achieve good compositional control with the targets that were used.

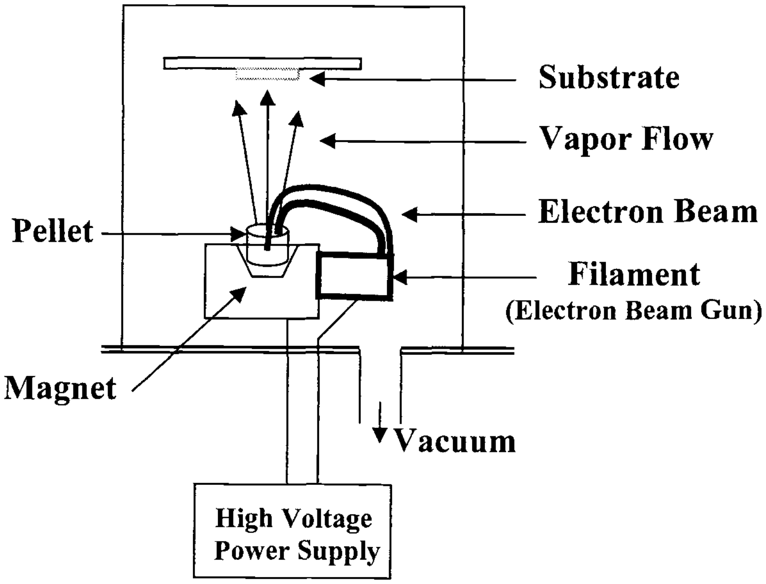

Figure 1.7. The schematic process of electron beam evaporation.

TRANSPARENT P-TYPE CONDUCTING THIN-FILM DEVELOPEMENT

The syntheses and structures of ABO_2 compounds (A=Ag and Cu, B=3+ cation) from reaction between Cu_2O and B_2O_3 were reported in the middle of the 20th century by Hahn and co-workers.[16,17] These materials are isostructural to delafossite, wherein the A and B atoms are coordinated by two O atoms in a linear dumb-bell unit, and the B atoms are coordinated by six O atoms in octahedral geometry. In 1971, Shannon and co-workers[18] expanded the number of examples by reporting the syntheses, properties, crystal structures, and electrical properties of ABO_2 materials with A=Pt, Pd, Cu, Ag and B=Co, Cr, Al, Ga, Fe, etc. A room-temperature metallic resistivity of $3\text{x}\ 10^{-6}$ ohm-cm was obtained for $PtCoO_2$, a value slightly greater than that of copper metal.

During the period 1984 to 1987, Benko and Koffyberg[19] studied the electrical properties of delafossite oxides such as $CuAlO_2$, $CuYO_2$, $CuGaO_2$, $CuCrO_2$, and $CuFeO_2$ in pressed-pellet form. All materials exhibit p-type conductivity and band gaps (3.35 ~ 3.60 eV) longer than those of Cu_2O (2.1 eV) and CuO (1.35 eV).

In 1992, Matthesis[20] proposed the existence of ordered delafossite-type superoxides in the system $CuYO_{2+\delta}$ $(0.5 \leq \delta \leq 0.7)$, before Cava and co-workers reported the intercalation of O in the Cu layers.

NiO thin films were prepared as transparent conductive oxide films by Sato and co-workers in 1993. The thin films were observed to be p-type with a resistivity of $1.4 \times 10^{-1}\ \Omega$ cm and a transmittance in the visible range below 40 %.[21]

In 1997, Cava and co-workers[22] described the synthesis of the delafossite derivatives $CuLaO_2$ and $CuYO_2$ as well as their oxidation products. They found intercalated O atoms in the Cu planes and examined the oxidized phases $CuLaO_{2.64}$ and $CuYO_{2.55}$ on the basis of X-ray diffraction and electron microscopy. The resistivities decreased with increasing oxygen content.

Thomas has described military and consumer applications involving invisible electronic circuits.[9] These devices require both p- and n-type transparent conductors. Several transparent, highly conducting n-type materials are known, but as yet there is no equivalent p-type material. To achieve suitable transparency, the band gap should exceed 3.1 eV.

p-Type transparent $CuAlO_2$ thin films were fabricated by Kawazoe and co-workers[10] in 1997. They reported a 3.1-eV band-gap, 1 S/cm conductivity, and 70 % transmittance in the visible. Following this report, additional transparent p-type oxides $CuAlO_2$[23,24], $CuGaO_2$[24,25], $CuInO_2$[26], $CuScO_{2+x}$[27], SrC_2O_2[28], and LaCuOS[29] were described.

In 2000, the Kawazoe group described new findings on $CuAlO_2$ – a reduced conductivity (~ 3 x 10^{-1} S/cm), a higher band gap (3.5 eV), and greater transmittance (~90 %) in the visible. $CuGaO_2$ and Ca-doped $CuInO_2$ thin films have been reported to have large optical band gaps, 3.4 and 3.9 eV, respectively with good transparencies, but the conductivities, 5.6 x 10^{-3} and 2.8 x 10^{-3} S/cm, respectively, are lower than $CuAlO_2$ thin films. Duan and co-workers prepared transparent p-type conducting $CuScO_{2+x}$ thin films having conductivity as high as

30 S/cm and 40% transparency in the visible portion of the spectrum. $SrCu_2O_2$ and LaCuOS were also reported as transparent p-type conductors. For K-doped $SrCu_2O_2$, reported characteristics are 3.3-eV band gap, ~ 80 % transparency, and 4.8×10^{-2} S/cm conductivity. The structure of LaCuOS is a layered type containing discrete CuS and LaOS layers. Unlike the delafossite oxides, the Cu atom is coordinated by four S atoms in a distorted tetrahedral geometry. $La_{1-x}Sr_xCuOS$ (x=0, 0.05) thin films exhibit a 3.1-eV band gap, ~80 % transparency, and 1.2×10^{-2} to 2.6×10^{-1} S/cm conductivity.

Considerable effort is being directed to the development of p-type transparent conductive thin films exhibiting high conductivities and mobilities, wide band gaps, and transparencies in the visible and IR regions of the spectrum. Some of the characteristics of the p-type materials that have recently been introduced are summarized in Table 1.2. Interatomic distances were derived from structural results in the Inorganic Crystal Structure Database.

Table 1.2. The characteristic summary of the selected p-type materials.

p-type	Chemical Formula (System)[18a]	Cu-Cu [Cu-O or Cu-S] (Å)	B.G. (eV)	σ(S/cm) Thin Film	Ref.
Oxides	$CuAlO_2$ (3R, 2H)	2.86 [2.04]	3.5	0.33 ~ 1	10,23,24
	$CuGaO_2$ (3R)	2.98 [1.88]	3.4	$5.6x10^{-3}$	24,25
	$CuInO_2$ (3R)		3.9	2.8x10-3 (Ca-doped)	26
	$CuCrO_2$ (3R)	2.98 [1.85]		10^{-5} (Pellet)	19
	$CuCa_{0.05}Cr_{0.05}O_2$			33 (Pellet)	19
	$CuFeO_2$ (3R, 2H)	3.04 [1.90]			19
	$CuScO_2$ (3R, 2H)	3.22 [1.80]	3.3		27
	$CuScO_{2+\delta}$			30	27
	$CuYO_2$ (3R, 2H)	3.53 [1.83]	3.6		20,22
	$CuCa_{0.05}Y_{0.95}O_2$			$2.2x10^{-3}$ (Pellet)	19
	$CuLaO_2$ (3R, 2H)	3.83 [1.85]			22
	$SrCu_2O_2$ (Tetra)	2.74 [1.84]	3.3	$4.8x10^{-2}$	28
	Cu_2WO_4 (Triclinic)	2.41 [1.73~]			30
	Cu_2O (Cubic)	3.01 [1.84]	2.1	$\sim10^{-3}$	31

Table 1.2 (Continued)

	CuO	2.90 [1.69]	1.35	$6.25x10^{-2}$	32
Sulfides	$CuGaS_2$ (Tetra)	3.74 [2.31]	2.5	10^{-3}~10^{-6} (Single Crystal)	33
	$CuInS_2$ (Tetra)	3.92 [2.33]	1.5	10^{-2}	34
	Cu_2S (Tetra, Hexa)	2.7 [2.31]	1.3		34
	$BaCu_2S_2$ (Tetra)	2.76 [2.41]			35
	$Ba_{0.8}K_{0.2}Cu_2S_2$ (Tetra)			200 (Single Crystal)	35
	$BaCu_2S_2$ (Ortho)	2.71 [2.36, <]		This Work	
Oxide-sulfides	LaCuOS (Tetra)	2.83 [2.44]	3.1	$1.2x10^{-2}$	29
	$La_{0.95}Sr_{0.05}CuOS$			$2.6x10^{-1}$	29
	Sr_2CuGa_3OS (Tetra)	2.73 [2.43]			36
Selenide-flouride	BaCuSeF (Tetra)	3.00 [Cu-Se: 2.565]			37
Sulfide-flouride	BaCuSF			This Work	

SYNTHESIS OF DELAFOSSITE-TYPE OXIDES (ABO_2)

Conventional high-temperature solid-state reactions have been used to prepare many ABO_2 delafossites. In the case of Cu derivatives, care must be taken to prevent oxidation of Cu (I). To obtain $CuYO_2$, $Cu_2Y_2O_5$, which contains Cu (II), is first synthesized from a mixture of Y_2O_3 and 2CuO at 1000 or 1100 °C in air. The $Cu_2Y_2O_5$ is then heated under flowing N_2(g) or Ar(g) to convert it to $CuYO_2$.[22] Under these conditions the reaction to produce $CuYO_2$ is entropically favored.

$$Cu_2Y_2O_5\ (s) \rightarrow 2CuYO_2 + 1/2O_2\ (g)$$

Hydrothermal methods have also been used for synthesis of delafossites, especially Ag derivates.

$$0.5Ag_2O + GaO(OH) \rightarrow AgGaO_2{}^{18}$$

Another method involves a simple low-temperature substitution reaction. The following reactions can lead to the production of In- and Sc-containing materials.

$$CuCl + LiInO_2 \rightarrow CuInO_2 + LiCl^{38}$$

$$CuCl + LiScO_2 \rightarrow CuScO_2 + LiCl^{39}$$

The reaction is run with excess CuCl. When complete, the products can be washed with NH_3(aq) to remove excess CuCl and LiCl. Previous attempts to use this reaction, however, have always led to products containing In_2O_3 and Sc_2O_3. An improvement of this method that leads to the production of single-phase material is described in Chapter 3. Also, as described in that chapter, a new, relatively low-temperature, flux-assisted method for preparation of $CuGaO_2$ has been developed. This technique should be generally applicable to other delafossite compounds.

CHARACTERIZATION OF TRANSPARENT P-TYPE CONDUCTORS

Conductivity[40-43]

The electrical conductivity (σ) of a material can be expressed by the equation

$$\sigma = n\mu_e e + p\mu_h e$$

where n is the number density (cm^{-3}) of electrons in the conduction band; p is the number of holes in the valence band; μ_e is the mobility (cm^2/Vs) of electrons; μ_h is the mobility of holes; and e is the charge of an electron. The resistance (R, ohm) of a sample is related to the distance between the measurement points (L, cm) and the its cross-sectional area (A, cm^2) by

$$R = \rho \text{ x } (L / A).$$

The resistivity, ρ, is the proportionality constant relating these variables to the measured resistance. It is common to report conductivity (σ, $ohm^{-1}cm^{-1}$ or S cm^{-1}), which is simply the reciprocal of the resistivity, i.e.,

$$\sigma = 1 / \rho.$$

Four-Probe Electrical Conductivity Measurement

The four-probe electrical measurement was performed in the Department of Physics at Oregon State University; a schematic of the set up is given in Figure 1.8. The resistance (R) can be determined from a current (I) – voltage (V) measurement by using Ohm's law: V = I x R. Conductivity can then be calculated by using the dimensions of the sample and the relationships given on the previous page. This four-probe measurement can also provide variable-temperature results, but mobilities and carrier concentrations cannot be derived. To determine these quantities a Hall measurement is required.

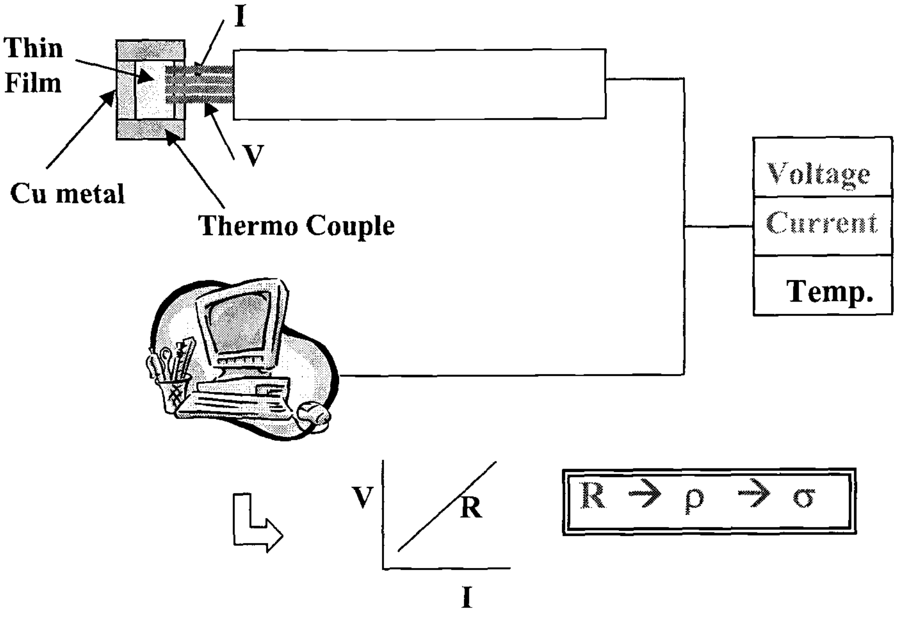

Figure 1.8. Schematic of four probe conductivity measurement

Hall Measurement[42]

Hall measurements have been performed with equipment in the Departments of ECE and Physics at Oregon State University. A schematic for explanation of the effect is given in Figure 1.9. Assume a constant current flow of electrons (n-type material) along the x-axis from the left to right. When a magnetic field (B_z) is applied in the z direction across the sample, electrons experience a Lorentz force. These electrons drift away from the current line toward the positive y axis, producing an excess surface electrical charge on the side of the sample and a Hall voltage V_H. The voltage is equal to IB/end, where I is the current; B is the magnetic field; d is the sample thickness; and e is the elementary charge. By measuring V_H and including the known values of I, B, and e, the charge-carrier density can be determined. From the four-probe electrical measurement, a value of the sheet resistance R_S can be determined, which can be used with the Hall measurement to calculate the mobility

$$\mu = |V_H|/(R_S IB) = 1/(en_S R_S)$$

where $\rho = R_S d$ and $n = n_S/d$.

By using a four-probe geometry, the carrier type, n or p, can also be determined.

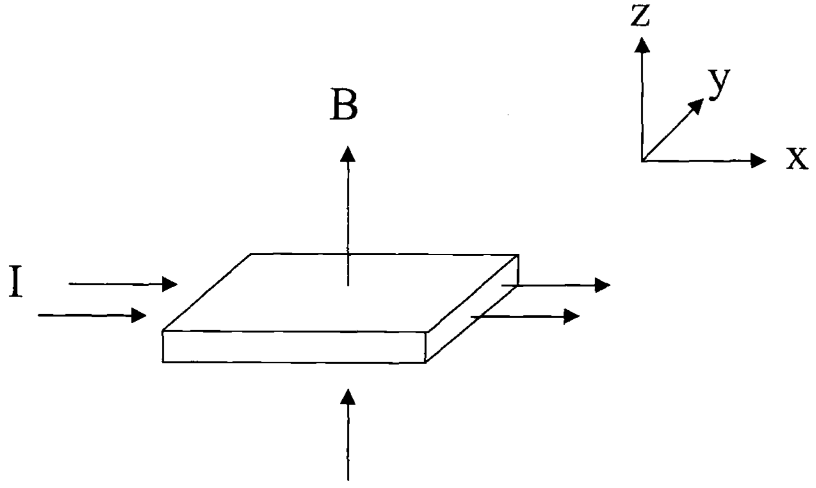

Figure 1.9. Schematic for Hall effect.

Seebeck Effect[42]

The carrier type, p or n, can be confirmed through a Seebeck measurement. This measurement was performed in the Department of Physics at Oregon State University. A schematic of the setup is given in Figure 1.10.

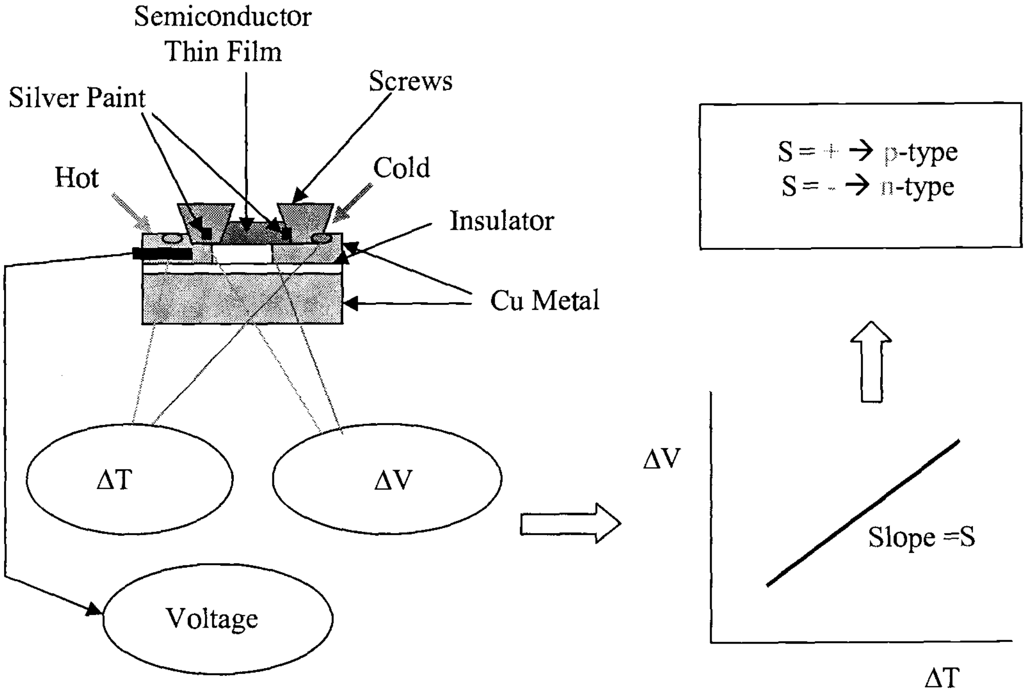

Figure 1.10. Schematic of Seebeck measurement.

The Seebeck effect is associated with the flow of current that occurs in a closed circuit made of two dissimilar materials, if the materials are maintained at two different temperatures,

$$\Delta V = S\,\Delta T.$$

The Seebeck coefficient, S, can be calculated from measurement voltage as a function of temperature. From the slopes of the temperature dependence, a material can be classified as n- or p-type, since an n-type material gives a positive contribution to the Seebeck effect, while a p-type material gives a negative contribution.

Transmittance and Band Gap[19,42]

Transmittance (T) is an important parameter charactering transparent conductors. The equation for transmittance is expressed as

$$\%\,T = I/I_0 \times 100,$$

where I_0 is the incident-light intensity and I is the transmitted-light. The band gap (E_g) in semiconductors is known as the energy gap between the valence band, the bottom-filled band, and the conduction band, the top empty band. The gap can be determined by an absorption (transmittance) measurement. Schematic of the process is given in Figure 1.11. Direct and indirect band gaps can be calculated by plotting $(\alpha h\upsilon)^2$ and $(\alpha h\upsilon)^{1/2}$, respectively, vs. $h\upsilon$, where α (cm^{-1}) is the optical absorption coefficient;

$$I = I_0 e^{-\alpha L}$$

: L is the film thickness (cm).

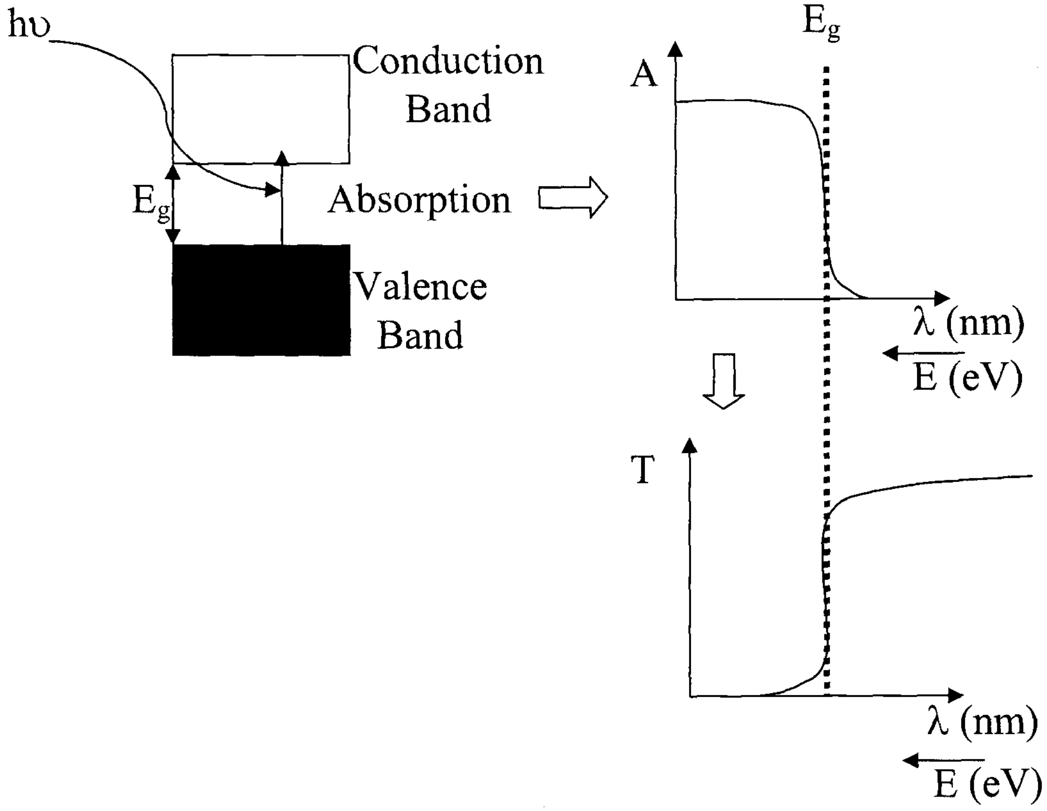

Figure 1.11. Schematic of transition between valence band and conduction band and associated absorption and transmittance curves as a function of wavelength (λ, nm) or photon energy (E, eV).

ATOMIC FORCE MICROSCOPY (AFM) AND SCANNING ELECTRON MICROSCOPY (SEM)[44]

AFM and SEM have been used to image a number of different types of thin films. The AFM and SEM laboratory facilities are located in the Department of Chemistry at Oregon State University and at the Hewlett-Packard Company, respectively. These analytical techniques are used as high-resolution imaging tools with nanometer-scale resolution. In SEM, a topographical image is formed from secondary-electron emission following a scan with a highly focused electron beam. In addition, the SEM can be used to monitor X-ray emission for chemical analysis. In AFM (Figure 1.12), the image is formed as a tip-cantilever moves across the sample surface; the interaction between the tip and sample is monitored by reflecting a laser beam off the back of the cantilever onto a photodiode detector.

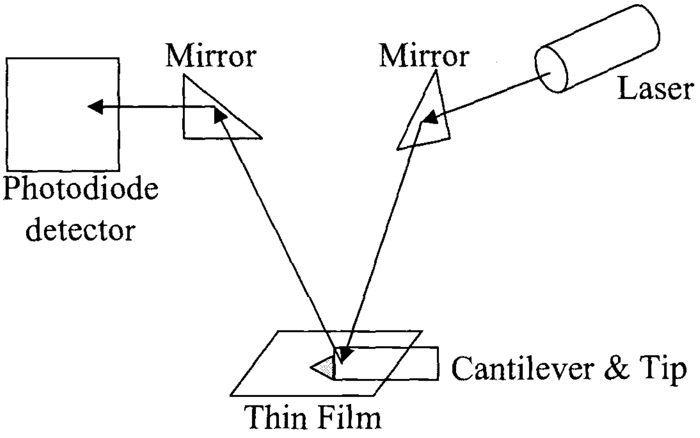

Figure 1.12 . Schematic of atomic force microscope.

PIEZOELECTRIC MATERIALS[11-13]

The piezoelectric effect is associated with the generation of an electric polarization in a crystal by the application of a stress. Conversely, an electric field applied to such a crystal causes it to become elastically strained. Quartz is one example of a piezoelectric material that is widely used in transducer and filter applications. In Chapter 8, the crystal growth and determination of an ordered derivative of the mineral Langasite are presented. Langasite is a commercial piezoelectric crystal that exhibits several improved attributes relative to those of quartz.

LUMINESCENCE[45]

Selected luminescent properties of doped $Y_3(SiO_4)_2Cl$, $Mn:Zn_2SiO_4$, and $Eu:Y_6WO_{12}$ are described in Chapters 9 and 10. In general, luminescent materials absorb some form of high-energy radiation and then emit a portion of this excitation at lower energies. The high-energy excitation can be energetic electrons in cathodoluminescence (CL) and electroluminescence (EL) or photons in photoluminescence. The excitation and emission processes for an ion doped into a solid are commonly modeled on the basis of the configuration-coordinate diagram (Figure 1.13), where the energy (E) is plotted versus the interatomic ion-ligand distance (R). The lower and upper parabolas represent the ground and excited states having different values of the equilibrium distances, R_0 and R_0', respectively. When the luminescent center absorbs energy, an electron is excited from the ground state to a high vibrational level in the excited state. Relaxation from this vibrational level to the lowest vibration level in the excited state occurs rapidly followed by a transition to a vibrational level in the ground state with emission of a photon. ΔR is determined by the amount of relaxation in the excited state, which is associated with atomic displacements and changes in the configuration coordinate. The magnitude of ΔR largely determines the energy difference between absorbed and emitted light, the so-called Stokes shift. In characterizing luminescent materials, we are interested in the energies of the excitation and emission transitions and the associated Stokes shift as these properties are of prime importance in the initial understanding of the luminescence process and for predicting its efficiency and potential utility.

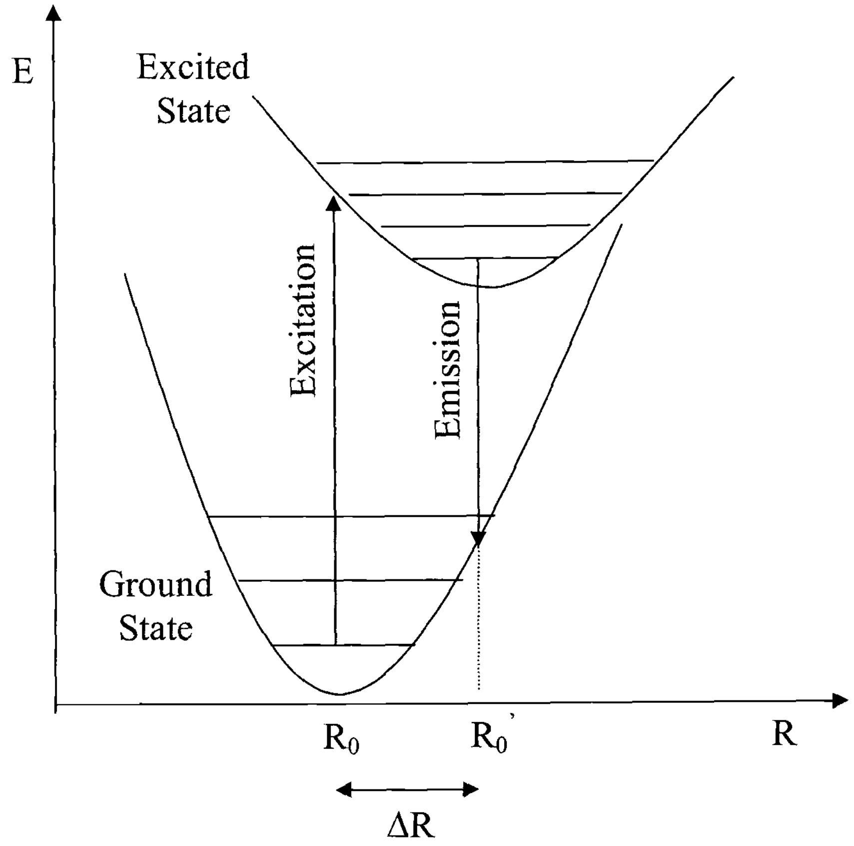

Figure 1.13. Configurational coordinate diagram.

References.

1. Ohring M., The Materials Science of Thin films, Academic Press, 1992.

2. Nicolau Y. F. *Appl. Surf. Sci.*, **22/23**, 1061-1074 (1985).

3. Nicolau Y. F., and Menard J. C., *J. Cryst. Growth*, **92**, 128-142 (1988).

4. Kanniainen T., Lindroos S., Prohaska T., Friedbacher G., Leskela M., Grasserbauer M., Niinisto L., *J. Mater. Chem*, **5(7)**, 985-989 (1995).

5. Kanniainen T., University of Helsinki, Faculty of Science, Department of Chemistry, Laboratory of Inorganic Chemistry, Helsinki, 2001.

6. Thomas P. Niesen and Mark R. De Guire, *J. Electroceramics*, **6**, 169-207 (2001).

7. Benjamin L.Clark and Douglas A Keszler, *Inorg.Chem.*,40,1724 (2001).

8. Lencka, M.M., Oledzka, M., Riman R., *Chem. Mater.*, 12, 1323 (2000).

9. Thomas Gordon, *Nature*, **389**, 907-908 (1997).

10. Kawazoe H., Yasukawa M., Hyodo H., Kurita M., Yanagi H., and Hosono H., *Nature*, **389**, 939-942 (1997).

11. K. Shimamura, H. Takeda, T. Kohno, and T. Fukuda, *J. Cryst. Growth*, **163**, 388-392 (1996).

12. Chai B.H.T., Bustamante A.N.P., Chou M.C., *Proc. 2000 IEEE/EIA Int. Freq. Control Symp. Exhib.*, 163-168 (2000).

13. G-T. Park, J-J Choi, J Ryu, H. Fan, and H-E Kim, *Appl. Phy. Lett.*, **80(24)**, 4606 (2002).

14. Keir P. D., Fabrication and Characterization of ACTFEL Devices, Ph. D. Dissertation, Oregon State University, 2000.

15. Koretsky M., Electronic Material Processing, Class Notes, Fall, 1999.

16. Hahn H., and Lorant C., *Z. Anorg. Allg. Chem.*, **279** 281-288 (1955).

17. Hahn H., and Kordes E., *Zeitschrift fur Kristallographie*, **129** 259-279 (1969).

18. Shannon R. D., Rogers D. B., and Prewitt C. T., *Inorg. Chem.*, **10(4)**, 713-718 (1971); Prewitt C. T., Shannon R. D., and Rogers D. B., *Inorg. Chem.*, **10(4)**, 719-723 (1971); Rogers D. B., Shannon R. D., Prewitt C. T., and Gillson J. L., *Inorg. Chem.*, **10(4)**, 723-727 (1971).

19. Benko F. A., and Koffyberg F. P., *J. Phys. Chem. Solids*, **45(1)**, 57-59 (1984); Benko F. A., and Koffyberg F. P., *Can. J. Phys.*, **63**, 1306-1308 (1985); Benko F. A., and Koffyberg F. P., *Phys. Stat. Sol.*, **94**, 231-234 (1986); Benko F. A., and Koffyberg F. P., *Mat. Res. Bull.*, **21**, 753-757 (1986); Benko F. A., and Koffyberg F. P., *J. Phys. Chem. Solids*, **48(5)**, 431-434 (1987).

20. Mattheiss L. F., *Phys Rev. B*, **48(24)**, 18300-18303 (1993).

21. Sato H., Minami T., Takata S., and Yamada T., *Thin Solid Films*, **236**, 27-31 (1993).

22. Cava R. J., Zandbergen H. W., Ramirez A. P., Takagi H., Chen C. T., Krajewski J. J., Peck W. F., Waszczak J. V., Meigs G., Roth R. S., and Schneemeyer L. F., *J. Solid, State Chem.*, **104**, 437-452 (1993).

23. Yanagi H., Inoue S., Ueda K., Kawazoe H., and Hosono H., *J. Appl. Phys.*, **88(7)**, 4159-4162 (2000).

24. Yanagi H., Kawazoe H., Kudo A., Yasukawa M., and Hosono H., *J. Electroceramics*, **4(2/3)**, 407-414 (2000).

25. Ueda K., Hase T., Yanagi H., Kawazoe H., Hosono H., Ohta H., Orita M., and Hirano M., *J. Appl. Phys.*, **89(3)**, 1790-1793 (2001).

26. Yanagi H., Hase T., Ibuki S., Ueda K., and Hosono H., *Appl. Phys. Lett.*, **78(11)**, 1583-1585 (2001).

27. Duan N., Sleight A. W., Jayaraj M. K., and Tate J., *Appl. Phys. Lett.*, **77((9)**, 1325-1326 (2000).

28. Kudo A., Yanagi H., Hosono H., and Kawazoe H., *Appl. Phys. Lett.*, **73(2)**, 220-222 (1998).

29. Ueda K., Inoue S., Hosono Hirose S., Kawazoe H., and Hosono., *Appl. Phys., Lett.*, **77(17)**, 2701-2703 (2000).

30. Marinder D.-O., Wang P.-L., Werner P.-E., Westdahl M., Andresen A. F., and Louer D., *Acta Chemica Scandinavica A*, **41**, 152-157 (1987).

31. Parretta A., Jayaraj M. K., Nocera A. D., Loreti S., Quercia L., and Agati A., *Phys. Stat. Sol. (a)*, **155**, 399-404 (1996).

32. Koffyberg F. P. and Benko F. A., J. Appl. Phys., 53(2), 1173-1177 (1982).

33. Oishi K., Kobayashi S., Ohta S.-I., Tsuboi N., and Kaneko F., *J. Cryst. Growth*, **177**, 88-94 (1997); Oishi K., Kobayashi S., and Kaneko F., J *Cryst. Growth*, **153**, 158-163 (1995); Susaki M., Horinaka H., and Yamamoto N., *J. Appl. Phys.*, **30**, 2797-2801 (1991); Susaki M., Horinaka H., and Yamomoto N., *Jpn. J. Appl. Phys.*, **31(Pt. 1, No. 2A)**, 301-304 (1992).

34. Alt M., Lewerenz H. J., and Scheer R., *J Appl. Phys.*, **81(2)**, 956-959 (1997).

35. Zhang X., Hogan T., Kannewurf C. R., and Kanatzidis M. G., *J Alloys Compd.*, **236**, 1-5 (1996).

36. Zhu W. Z., and Hor P. H., *Inorg. Chem,*, **36**, 3576-3577 (1997).

37. Zhu W. J., Huang Y. Z., Wu F., Dong C., Chen H., and Zhao Z. X., *Mat. Res. Bull.*, **29(5)**, 505-508 (1994).

38. Shimode M., Sasaki M., and Mukida K., J. *Solid. State. Chem.*, **151**, 16-20, (2000).

39. Doumerc J.-P., Ammar A., Wichainchai M. P., and Hagenuller P., *J. Phys. Chem. Solids*, **48(1)**, 37-43 (1987).

40. West A. R., *Solid State Chemistry and its Applications*, John Wiley & Sons Ltd, Chapter 14, 1995.

41. Sleight A. W., Solid-State Chemistry, Class Notes, Spring, 1999.

42. Cox P. A., The Electronic Structure and Chemistry of Solids, Oxford University Press.

43. Shriver D. F., Atkins P., and Langford C. H., Inorganic Chemistry, Second Edition, Freeman.

44. Russell P., Batchelor D., Thornton J., SEM and AFM: Complementary Techniques for High Resolution Surface Investigations, Digital Instruments.

45. Blasse G., Grabmaier B. C., Luminescent Materials, Springer-Verlag, 1994.

CHAPTER 2

LOW-TEMPERATURE THIN-FILM DEPOSITION AND CRYSTALLIZATION

Sangmoon Park, Benjamin L. Clark, Douglas A. Keszler,
Jeffrey P. Bender, John F. Wager,
Thomas A. Reynolds, Gregory S. Herman

Science, **297**, 65 (2002)

ABSTRACT

A new, general procedure is described for the low-temperature deposition and crystallization of refractory oxide films. The methods of successive ionic layer adsorption and reaction (SILAR) and hydrothermal dehydration are combined to produce a range of crystalline oxide films at temperatures near 400 K.

INTRODUCTION

Crystalline oxide films are significant components in a wide array of electronic and optical devices, and their study and manufacture comprise major aspects of current science and technology. A plethora of methods, such as sputtering, chemical vapor deposition, pulsed laser deposition, and sol-gel, are commonly utilized to deposit these films, and many new techniques are being developed (1). In each of these methods, however, the deposited film is amorphous. For those applications requiring a crystalline film, an additional high-temperature processing step is required. This high-temperature step can lead to considerable constraints in combining the desirable characteristics of a crystalline oxide film with those of thermally unstable substrates and other device components. High-temperature processing also adds considerable costs to manufacturing. We describe a simple method that provides a general means for both low-temperature deposition and crystallization of oxide films. To demonstrate the generality of the method, we describe here the production of Zn_2SiO_4, ZrO_2, and MnO_2 films, which are of interest for applications in displays, electronics, and energy storage, respectively.

The present method derives from our report on the preparation of oxide powders by a method of precipitation and hydrothermal dehydration (2). In this process, a hydroxo precipitate is dehydrated under hydrothermal conditions to yield an anhydrous, crystalline oxide at temperatures as low as 400 K. We have now combined this dehydration and crystallization process with the successive-ionic-layer-adsorption-and-reaction (SILAR) deposition method (3) to produce fully crystalline oxide films at low temperatures.

EXPERIMENTAL

In the SILAR process, the cation constituent is first adsorbed onto the substrate surface followed by a rinsing step in water to produce an approximate monolayer of coverage. The substrate is then transferred to a solution containing the anionic constituent wherein a precipitation reaction occurs at the surface of the substrate; the process is completed with an additional water rinse. This cycle of coating and rinsing is repeated many times under robotic control to achieve a desired film thickness. For the examples given here, substrates were immersed in ~0.1 M solutions and rinse baths for 10 s each, and 700 cycles were utilized to develop a film thickness near 250 nm. Dehydration was performed overnight (~12 h), although crystallinity in some systems has been observed after a 30-min treatment.

RESULTS

Films of Zn_2SiO_4 were produced on glass and nitrided silicon (Si_3N_4/Si) substrates by using the SILAR process with Zn^{2+}(aq) and SiO_4^{4-}(aq) as the cationic and anionic constituents, respectively. The SiO_4^{4-}(aq) species undergoes extensive hydrolysis, so the as-deposited film is an amorphous hydrated hydroxide salt. The film was crystallized by heating at 378 K in a sealed 23-mL Teflon-lined Parr reactor containing 0.03 mL of water. From consideration of the X-ray diffraction patterns in Figs. 2.1A and 2.1B, the resulting film is a highly crystalline form of Zn_2SiO_4. For comparison, annealing the amorphous, as-deposited film near the softening point of the glass substrate ($T = 923$ K) does not produce a crystalline product.

Crystalline films of ZrO_2 have been deposited on Si_3N_4/Si substrates. Again, SILAR deposition with the aqueous solutions Zr^{4+}(aq) and OH^-(aq) results in an amorphous, hydroxylated film. Following hydrothermal dehydration at 473 K, the resulting diffraction pattern reveals the formation of the expected monoclinic form of ZrO_2; an electron micrograph of the resulting film is given in Fig. 2.1C. Curiously, direct annealing of the amorphous film in air at 923 K results in the production of an oxygen-deficient tetragonal form of $ZrO_{2-\delta}$, while under normal conditions this phase exists only at temperatures above 1273 K (4). Annealing the monoclinic film at 923 K results in no structural change.

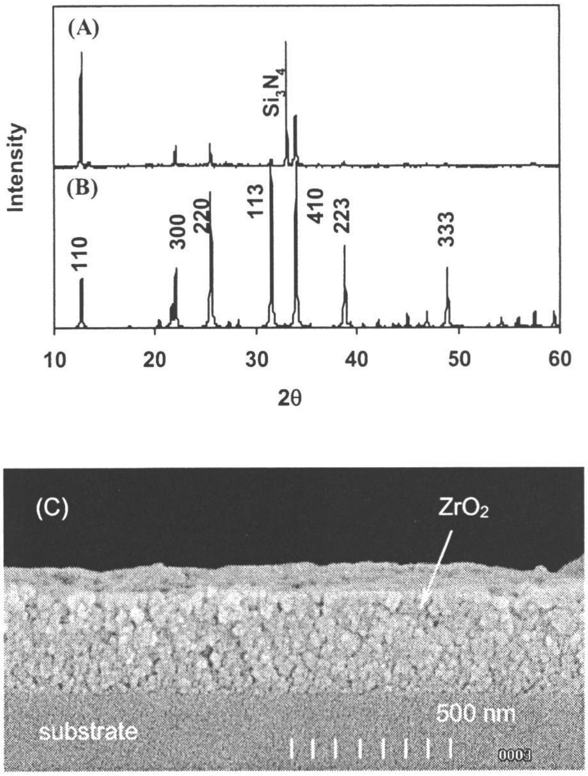

Figure 2.1. (A) X-ray diffraction pattern of Zn_2SiO_4 film on Si_3N_4/Si
(B) Simulated powder X-ray diffraction pattern of Zn_2SiO_4
(C) Electron micrograph of ZrO_2 film on Si_3N_4/Si substrate

MnO_2 and Mn_2O_3 have been deposited on SiO_2/Si substrates by using the solutions $Mn^{2+}(aq)$ and $OH^-/H_2O_2(aq)$. The as-deposited material is amorphous. Following a hydrothermal anneal at 473 K, the film is crystalline, forming the tetragonal, rutile form of MnO_2 (5). Annealing the as-deposited film at 773 K results in loss of oxygen and production of the cubic, bixbyite structure of Mn_2O_3 (6). These processing methods thus provide facile control of product formation and oxidation states of the Mn cation.

A simple and general method has been demonstrated for both low-temperature thin-film deposition and crystallization of refractory oxides. It provides unique opportunities for development of new manufacturing methods, generation of unusal composite materials, and application of high-temperature materials to low-cost substrates, as shown by the deposition of a green-emitting phosphor on a flexible, plastic substrate (Fig. S2.2) (7).

Low-Temperature Thin-Film Deposition and Crystallization

Sangmoon Park, Benjamin L. Clark, Douglas A. Keszler, Jeffrey P. Bender,
John F. Wager, Thomas A. Reynolds, Gregory S. Herman

Supplementary Information

A demonstration of the capabilities of hydrothermal annealing for realization of crystalline oxide films on plastic is given by the deposition of the green-emitting phosphor Mn:Zn_2GeO_4 on a flexible substrate (see Figure S2.1.) The substrate is DuPont Kapton HPP-ST polyimide, a material that is commonly employed in the fabrication of organic light emitting devices and rated for continuous use at temperatures not exceeding 493 – 513 K. A thin, 20-nm film of Ti metal is deposited onto the polyimide to promote adhesion while retaining flexibility of the ceramic oxide film. The amorphous, as-deposited oxide was hydrothermally annealed in a closed Teflon container at 423 K. The bright green photoluminescence is a direct measure of the crystallinity of the phosphor, as the amorphous, as-deposited film exhibits no luminescence. Insofar as we know, this represents the first example of the direct deposition of a refractory, crystalline highly luminescent oxide onto a low-temperature, flexible substrate.

Supplemental Figure 2.2. Photoluminescent, green-emitting Mn:Zn_2GeO_4 phosphor film deposited onto flexible, polyimide substrate.

ACKNOWLEDGMENTS. This work was supported by grants from the Hewlett-Packard Company and the National Science Foundation (DMR-0071899, DMR-0071727, and DMI-0128677).

REFERENCES

1. M. Ritala, K. Kukli, A Rahtu, P. I. Räisänen, M. Leskelä, T. Sajavoara, J. einonen, *Science* **288**, 319 (2001).
2. B. L. Clark, D. A. Keszler, *Inorg. Chem.* **40**, 1724 (2001).
3. Y. F. Nicolau, *Appl. Surf. Sci.* **22**, 1061 (1985).
4. U. Martin, H. Boysen, F. Frey, *Acta Crystallogr., Sect. B* **49**, 403 (1993).
5. W. H. Baur, *Acta Crystallogr., Sect. B* **32**, 2200 (1976).
6. S. Geller, *Acta Crystallogr., Sect. B* **27**, 821 (1971).

See supplementary information available on *Science* Online at

www.sciencemag.org/cgi/content/full/297/5578/65/DC1

CHAPTER 3

SYNTHESIS OF 3R-$CuMO_{2+\delta}$ (M = Ga, Sc, In)

Sangmoon Park and Douglas A. Keszler

Modified version submitted to Journal of Solid State Chemistry

ABSTRACT

Improvements have been made in the single-phase synthesis of 3R $CuScO_2$ and $CuInO_2$ by the metathesis method. A new flux-assisted procedure has also been devised for the preparation of $CuGaO_2$. Oxygen insertion into $CuScO_2$ and $CuInO_2$ has been examined by heating samples in air to a temperature of 723 K.

INTRODUCTION

Chemical and physical properties of numerous compounds, $CuMO_2$ (M = +2, +3, +4 cation,) crystallizing in the structure of delafossite, $CuFeO_2$ (1), have been examined (2, 3). In particular, the compounds $CuScO_2$ and $CuInO_2$ have recently been studied as transparent p-type conductors (4,5). Their bulk synthesis, however, has been a challenge. The Sc derivative exists in two polytypes - 2H and 3R. The 2H form can be stabilized by incorporation of small amounts of Mg, but up to now, no method has been reported for the synthesis of single-phase 3R material. The preparation of $CuInO_2$ has likewise been difficult because of its relatively low decomposition temperature - 873 K.

A low-temperature substitution reaction

$$CuCl + AMO_2 = CuMO_2 + ACl \quad (A = Li, Na; M = In, Sc)$$

has been described for synthesis of these compounds, but its use has resulted in the generation of multiphase products, i.e., following the procedures of Doumerc, Ammar, Wichainchai, *et. al.* (6) we observe residual Sc_2O_3 and Cu_2O in the preparation of $CuScO_2$, and residual In_2O_3 and Cu_2O are observed in the preparation of $CuInO_2$ (7). In principle, the substitution reaction should provide a simple means for the realization of single-phase products; for $CuScO_2$, the reaction affords only the 3R polytype as part of the product mixture, and the reaction occurs below the decomposition temperature of $CuInO_2$. The synthetic challenge is then to simply improve the yield of the substitution process, and, as we describe below, this can be done in a straightforward manner. In addition to improving the low-temperature metathesis reaction, a new, flux-assisted method is described for the synthesis of the Ga derivative, $CuGaO_2$, providing a procedure that should be applicable to the preparation of a variety of other delafossites and related oxides. Given the availability of single-phase 3R Sc and In delafossites, we have also examined their oxidation on heating in air to form $CuMO_{2+\delta}$, $\delta > 0$ (M = In, Sc).

EXPERIMENTAL

For the preparation of $CuScO_2$ and $CuInO_2$, the reagents Sc_2O_3 (Stanford Materials 99.9%), In_2O_3 (Cerac 99.99%), Li_2CO_3 (Cerac 99.999%), Na_2CO_3 (Cerac 99.995%), and CuCl (Alfa 99%) were used. $NaInO_2$ and $LiScO_2$ were prepared by heating the appropriate stoichiometric quantities of Na_2CO_3, Li_2CO_3, In_2O_3, and Sc_2O_3 in alumina crucibles at 1273 K for 12 h. $LiScO_2$ and $NaInO_2$ were loaded with 30 mol% excess CuCl in separate alumina tubes, which were subsequently sealed inside evacuated silica tubes. The Sc mixture was then heated for 12 h at 973 K, and the In mixture was heated for 3 h at 873 K. The cooled products were vigorously stirred in 2 M NH_3(aq) for several hours to remove LiCl, NaCl, and excess CuCl.

For the preparation of $CuGaO_2$, the reagents Ga_2O_3 (Cerac 99.995%), Cu_2O (Cerac 99%), CuCl (Alfa 99%), and KCl (MCB Reagent) were used. Products were characterized from reactions of 80 wt% (Ga_2O_3 + Cu_2O)/ 20 wt% (0.7 CuCl + 0.3 KCl) and 80 wt% (Ga_2O_3 + Cu_2O)/ 20 wt% (0.3 CuCl + 0.7 KCl.) The mixtures were heated in sealed, evacuated silica tubes from 573-1073 K for 15 h. The products were stirred in 2 M NH_3(aq) overnight to remove the flux components. All samples were characterized by X-ray diffraction on a Siemens D-5000 powder system, both before and after washing in NH_3(aq.)

Oxygen uptake in production of $CuMO_{2+\delta}$ ($M = Sc$, In; $\delta > 0$) was determined by heating samples at 523, 573, 623, 673, and 723 K for three days at each temperature. The same sample was used for each successive heating step so that each was heated for a total of fifteen days. The powders were weighed and ground after each heat treatment.

RESULTS

As shown by the diffraction patterns in Figures 3.1 and 3.2, application of the metathesis reactions

$$LiScO_2 + CuCl = CuScO_2 + LiCl$$

$$NaInO_2 + CuCl = CuInO_2 + NaCl$$

can lead to the production of single-phase 3R-delafossites $CuScO_2$ and $CuInO_2$. In each X-ray pattern, there is no evidence of other phases such as In_2O_3, Sc_2O_3, and Cu_2O or the the 2H polytype of $CuScO_2$ in Figure 3.3 and 3.4. The presence of In_2O_3, Sc_2O_3, or Cu_2O in the products, as noted by others (7), likely arises from reaction between the alkali-metal reagents and the container, SiO_2. Indeed, when heating the reagents directly in silica tubes, severe attack of the tube is readily noted. To circumvent these side reactions, the reagents are first placed in an alumina tube, which is subsequently sealed inside the silica tube, providing a physical barrier between the reagents and the silica. The net result is a straightforward application of the substitution reaction.

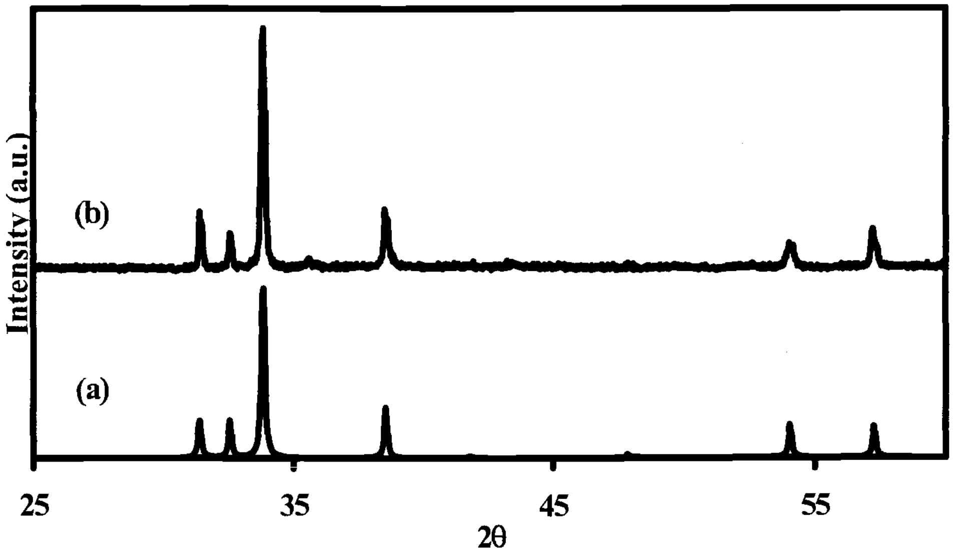

Figure 3.1. (a) Experimental X-ray diffraction pattern for 3R $CuScO_2$ (b) Simulated X-ray diffraction pattern for 3R $CuScO_2$ (for structural data, see reference 6).

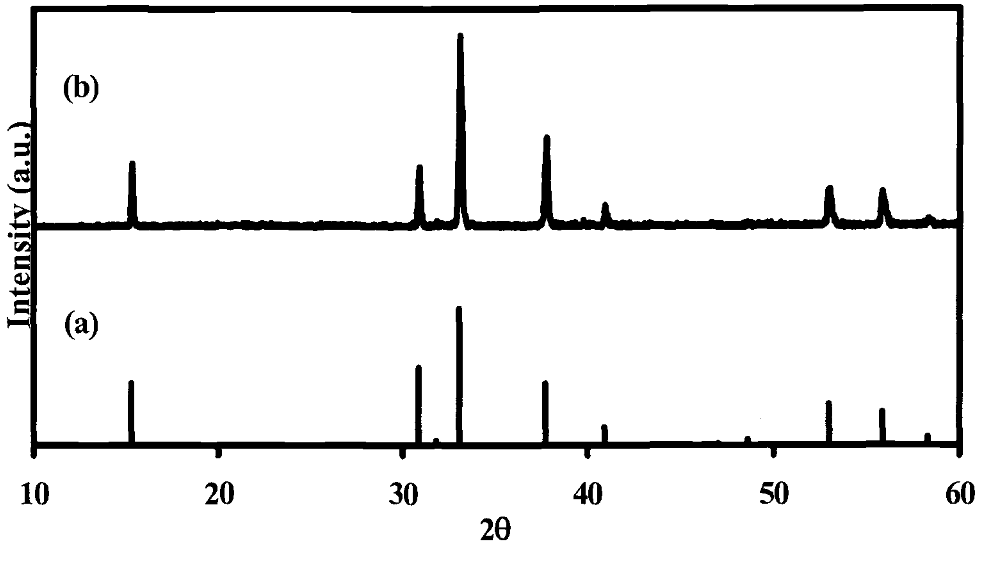

Figure 3.2. (a) Experimental X-ray diffraction pattern for 3R $CuInO_2$ (b) Simulated X-ray diffraction pattern from structural data in reference 7.

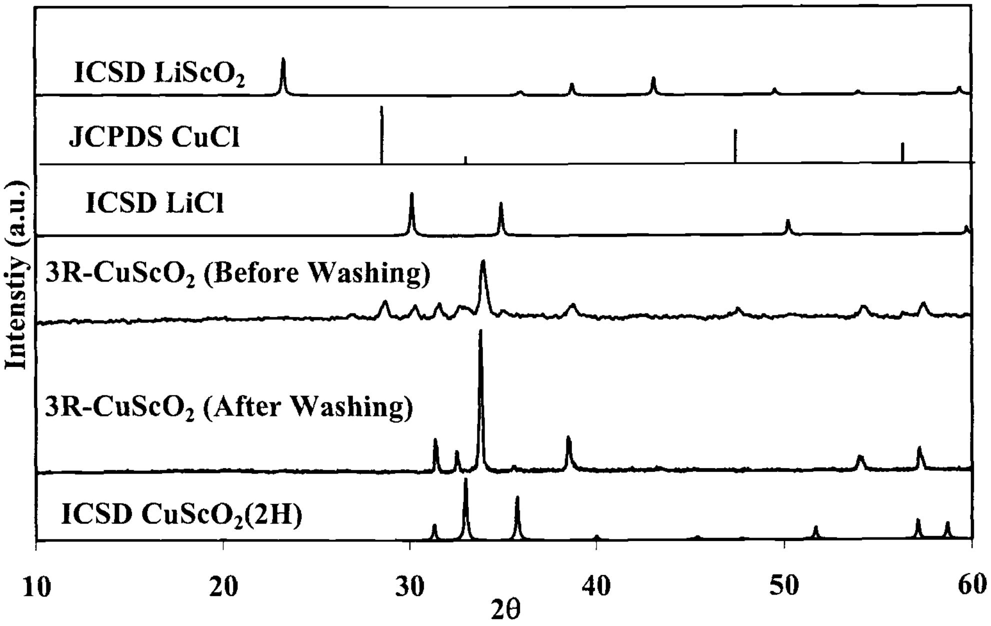

Figure 3.3. Calculated $LiScO_2$, CuCl, LiCl, and 2H-$CuScO_2$ and observed 3R-$CuScO_2$ (before and after washing with NH_4OH) X-ray diffraction patterns.

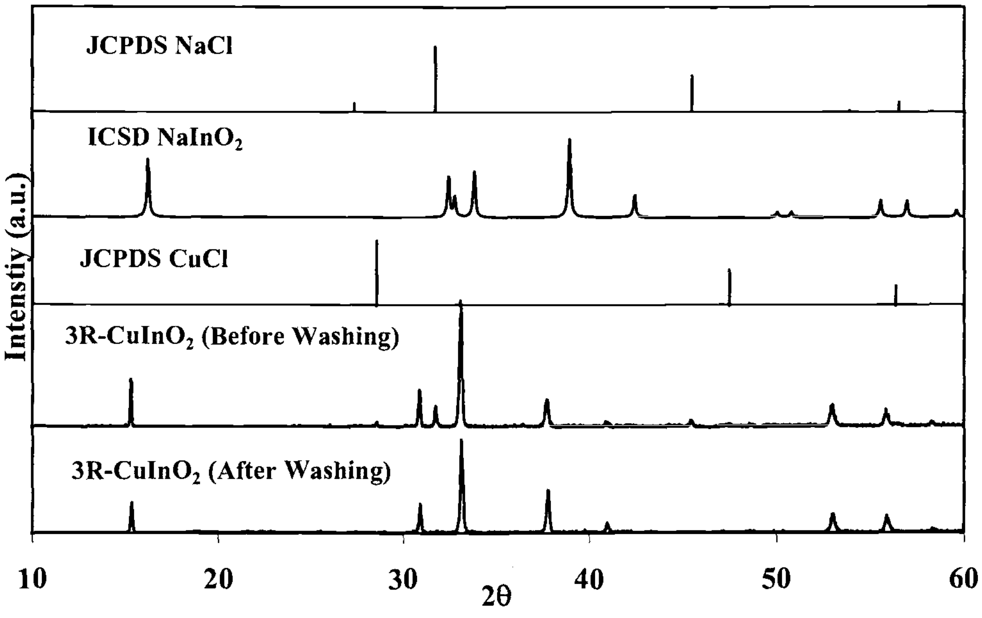

Figure 3.4. Calculated NaCl, NaInO$_2$, and CuCl and observed 3R-CuInO$_2$ (before and after washing with NH$_4$OH) X-ray diffraction patterns.

We note that the resulting $CuScO_2$ powder exhibits a light gray-blue color. This color likely results from the presence of a small amount of unreacted or excess Cu compound in the sample, as heating the powder in a sealed, evacuated tube across a temperature gradient of 50 K at 1273 K leads to a color that is more aptly described as off white, a result that is consistent with the band gap, > 3 eV (8). The $CuInO_2$ product exhibits a rather deep off-yellow body color, a result that is consistent with the reported absorption spectrum of thin films (5).

The success of these metathesis processes derives from the topochemical nature of the reactions. The Sc-O and In-O structural connectivities in $LiScO_2$ (9) and $NaInO_2$ (10), respectively, match those in the corresponding materials $CuScO_2$ and $CuInO_2$; in the metathesis process only the coordination environments of the Li(Na) and Cu atoms change. For the preparation of $CuGaO_2$, a corresponding topochemical substitution is not possible, since the compounds $MGaO_2$ (M = Li, Na, K) crystallize with tetrahedral coordination of the Ga atoms (11), and application of the low-temperature replacement process does not lead to a delafossite product. To promote the reaction between Ga_2O_3 and Cu_2O at low temperatures, we have utilized a flux-assisted approach with the KCl-CuCl system (12) in Figure 3.5, which exhibits a deep eutectic (T_m = 398 K) near 30 mol% KCl/70 mol% CuCl. By using a equimolar mixture of the eutectic and the oxide formulation 0.5 Cu_2O:0.5 Ga_2O_3, we observe production of $CuGaO_2$ at temperatures near 673 K; the product is retained on heating the mixture to 1073 K. Refined cell parameters for the phase are $a = 2.9767(7)$ and $c = 17.174(3)$ Å. In the

KCl-rich portion of the diagram, however, the results at much different. At the composition 70 mol% KCl/30 mol% CuCl, the liquidus occurs at approximately 813 K. In an equimolar mixture of this KCl/CuCl composition and 0.5 Cu_2O:0.5 Ga_2O_3, no reaction between Cu_2O and Ga_2O_3 is observed at 673 K. Just below the liquidus at 773 K, Cu_2O and Ga_2O_3 react to form $CuGaO_2$, while at temperatures above the liquidus, the major peaks in the X-ray diffraction patterns of the products correspond to Ga_2O_3. So, above the liquidus, Cu_2O is preferentially dissolving in the flux, leaving Ga_2O_3 as the precipitated product. To promote the smooth formation of $CuGaO_2$ from Cu_2O and Ga_2O_3, the flux should be more concentrated in Cu, i.e., near the eutectic point. Considering the characteristics of the method, it should be generally applicable to the preparation of other delafossite compounds and related oxides.

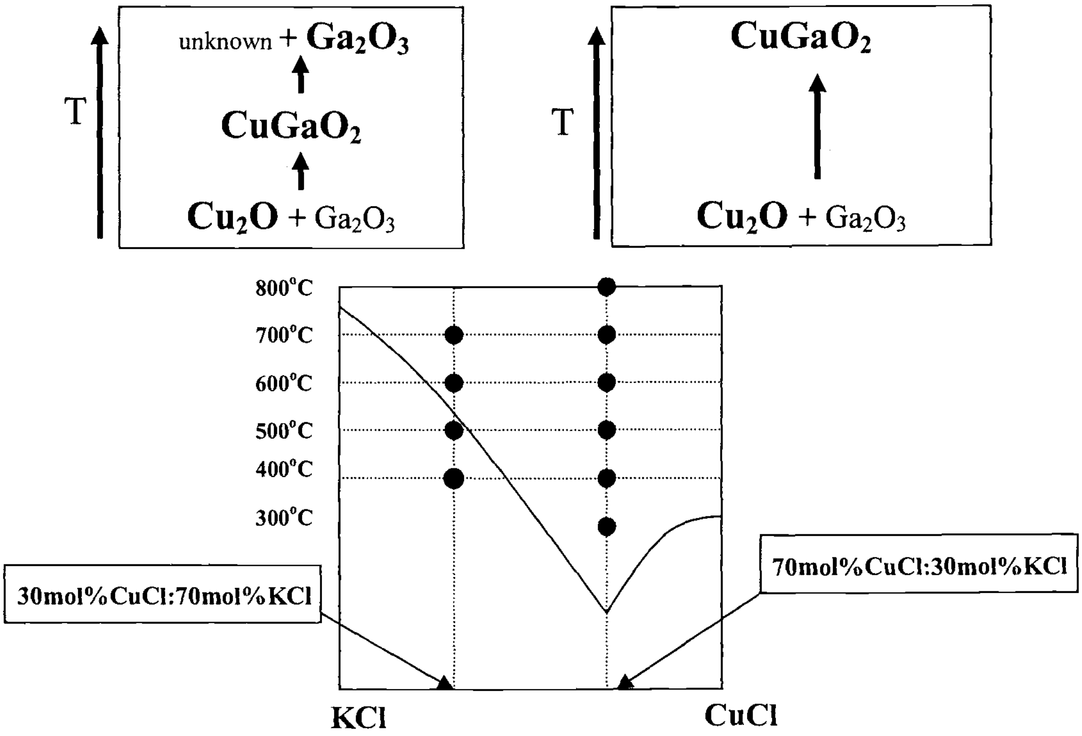

Figure 3.5. The reaction between Ga_2O_3 and Cu_2O with KCl – CuCl system.

Since single-phase 3R $CuInO_2$ and $CuScO_2$ powders are now available, we have done a cursory examination of the oxidation products that occur on heating in air. The results are plotted in Figure 6 and summarized in Table 3.1. As noted in the experimental section, all samples were heated at each of the indicated temperatures for three days. For $CuScO_2$, heat treatment at 523 K affords a discoloration of the sample from white to gray and a very small increase in mass. At 623 K, the sample has turned black, and the mass increase corresponds to a stoichiometry of $CuScO_{2.06}$. The increasing trend in the cell parameters following these heat treatments is consistent with a small solubility of O atoms in the 3R structure. At 673 K, the stoichiometry is $CuScO_{2.26}$, but the X-ray pattern can be accounted for on the basis of a two-phase mixture comprised of lightly and heavily O-doped phases. At 723 K, decomposition begins with appearance of CuO and Sc_2O_3 in the diffraction pattern; the heavily doped O phase, however, is still discernable, and no change in unit-cell volume is observed between 673 and 723 K. We note that the poor fit of the data to the larger hexagonal cell at 673 K and 723 K provides some evidence that the symmetry of this phase could be lower than indicated by the hexagonal cell.

The results for air oxidation of $CuInO_2$ are similar to those of $CuScO_2$ in Figure 3.7 and 3.8. Up to 623 K, a volume increase is observed, but the O concentation is higher than that of $CuScO_{2+\delta}$ (*cf.*, Table 3.1.) At 673 K, the material separates into a two-phase product of lightly and heavily doped O components. In contrast to $CuScO_2$, the O-rich form of $CuInO_{2+\delta}$, $\delta = 0.67$ exhibits a higher thermal stability, providing a single-phase product at 723 K that is nicely indexed with a hexagonal cell. The differences between $CuInO_2$ and $CuInO_{2.67}$ are readily apparent from comparison of their X-ray patterns in Figure 8. Reflections of the type (00*l*) exhibit only minor shifts on O insertion, whereas reflections of the type $k,l \neq 0$ exhibit significant shifts. The shifts indicate that the cell is preferentially expanding in the *ab* plane upon O insertion. In the two-phase regions of the phase diagrams for the Sc and In analogues, the diffraction patterns are essentially composites of the two patterns of Figure 3.7 and 3.8.

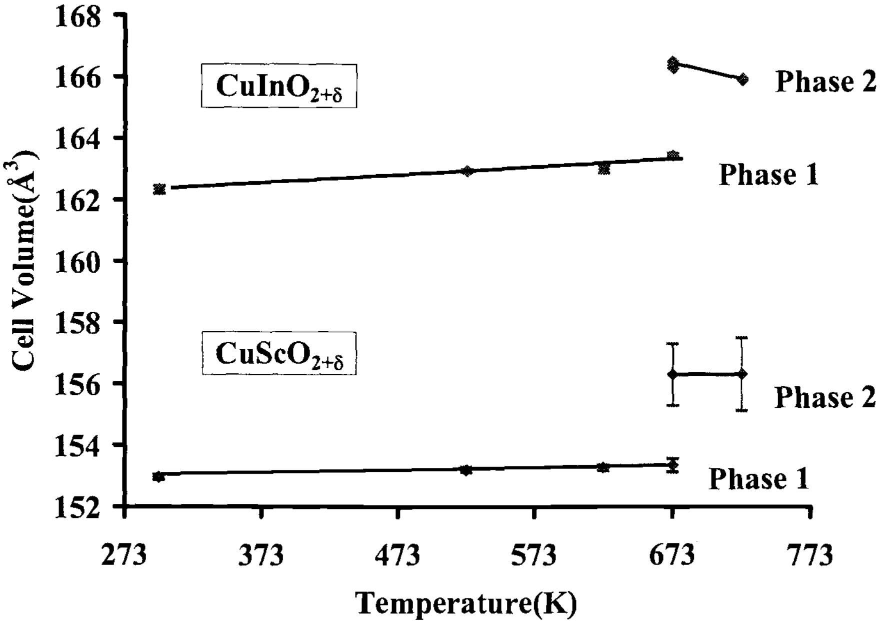

Figure 3.6. The plot of cell volume vs. temperature for $CuMO_{2+\delta}$ (M = Sc, In).

TABLE 3.1. Cell parameters and δ values for $CuMO_{2+\delta}$ (M = Sc, In)

$CuMO_2$	a (Å)	c (Å)	V (Å^3)	δ
M = Sc	3.2160(6)	17.077(3)	152.96(5)	0
523 K	3.2180(6)	17.081(3)	153.18(5)	<0.01
623 K	3.2183(6)	17.086(3)	153.26(5)	0.06
673 K	3.219(2)	17.089(9)	153.3(1)	0.26
	3.253(7)	17.06(4)	156.3(6)	
723 K	3.253(8)	17.05(4)	156.3(7)	decomposition
M = In	3.2869(9)	17.349(4)	162.32(7)	0
523 K	3.2904(4)	17.376(2)	162.92(3)	<0.01
623 K	3.2916(9)	17.370(3)	162.98(7)	0.09
673 K	3.2950(5)	17.382(2)	163.44(4)	0.32
	3.3240(8)	17.387(3)	166.37(6)	
723 K	3.3222(2)	17.355(1)	165.89(2)	0.67

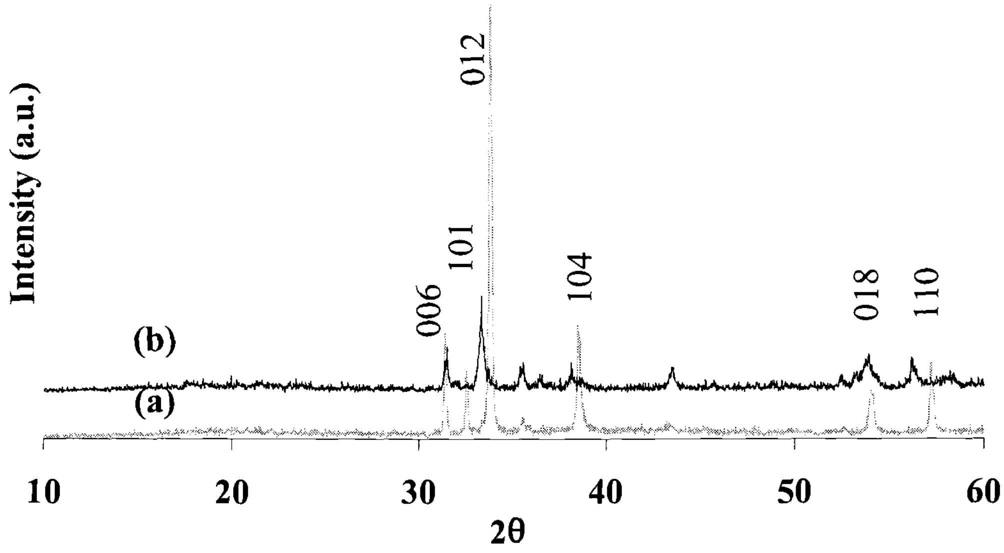

Figure 3.7. X-ray diffraction patterns for $CuScO_{2+\delta}$. Black line represent $\delta = 0$, and gray line represent $\delta = 0.26$.

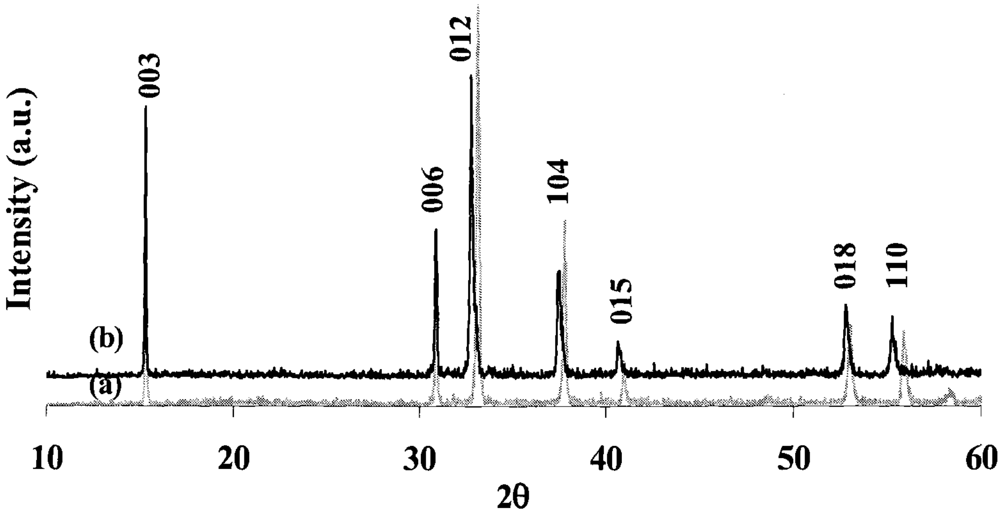

Figure 3.8. X-ray diffraction patterns for $CuInO_{2+\delta}$. Black line represents $\delta = 0$, and gray line represents $\delta = 0.67$.

The results on oxidation of $CuScO_2$ are qualitatively similar to those previously reported (13) for samples heated in flowing $O_2(g)$ at 673 K, where a large volume increase was observed, corresponding to an expansion of the *a* axis and a slight contraction of the *c* axis (*cf.*, Table 3.1.) The maximum O incorporation in the previously reported study corresponds to $\delta = 0.37$, a value that exceeds our observation of $\delta = 0.26$. This result is expected, as we heated samples in air rather than O_2 (g), and O insertion in the Sc compound is kinetically slow. The observation of a two-phase region in this system is also consistent with a previous report on the compounds $LaCuO_{2+\delta}$ and $CuYO_{2+\delta}$ (14). The results on $CuInO_{2+\delta}$ follow those of the Sc analog, but higher O concentrations are more readily realized in the In derivative. This higher concentration can be associated with the larger crystal radius of In (r = 0.93 Å) *vs*. Sc (r = 0.87 Å) (15) and the larger cell volume of $CuInO_2$ (*cf.* Table 3.1). The delafossite structure (Figure 3.9) contains hexagonal arrays of Cu(I) atoms that can be oxidized. O incorporation occurs through placement of atoms in triangular hollows formed by nearest-neighbor Cu atoms. In the Sc derivative, these nearest-neighbor Cu···Cu distances are shorter than those in the In compound, as seen by comparing the lengths of the *a* axes (Table 3.1), likely contributing to the slower kinetics of O insertion. Similarly, for $CuGaO_2$ with its even shorter *a* axis, heating in air under the same conditions does not produce a measurable increase in mass; O insertion does not occur under these conditions. At 1073 K, the compound is oxidized to CuO and $CuGa_2O_4$.

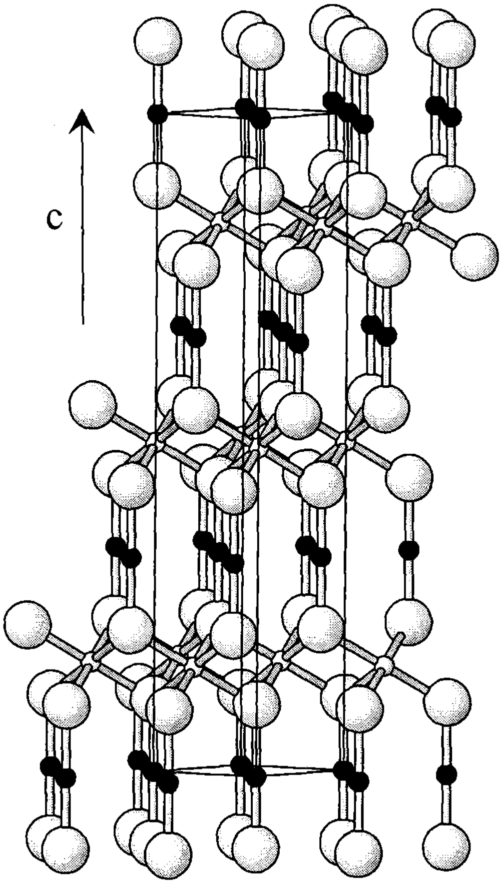

Figure 3.9. Drawing of the structure of delafossite. Large open circles represent O atoms, small filled circles represent Cu atoms, and small open circles represent M atoms such as Sc or In.

CONCLUSIONS

Single phase 3R forms of $CuScO_2$ and $CuInO_2$ can readily be prepared by a relatively low-temperature metathesis reaction; care must be taken to prevent reaction of the reagents with the container. A flux-assisted method can be used to prepare $CuGaO_2$ at temperatures as low as 773 K. O insertion proceeds more readily in the In derivative relative to that of the Sc derivative because of the larger size of the In atom. This larger size also leads to a higher thermal stability of the oxidized In delafossite.

ACKNOWLEDGMENTS

This work was supported by the US National Science Foundation (DMR-0071727). We thank Professors A. W. Sleight and J. Tate for many technical discussions at OSU on delafossite compounds.

REFERENCES

1. A. Pabst, Amer. Mineralogist 23 (1938) 175-176.

2. R. D. Shannon, D. B. Rogers, C. T. Prewitt, Inorg. Chem. 10 (1971) 713-718.

3. R. Nagarajan, N. Duan, M. K. Jayaraj, J. Li, K. A. Vanaja, A. Yokochi, A. Draeseke, J. Tate, A. W. Sleight, Internat. J. Inorg. Mater. 3 (2001) 265-270.

4. N. Duan, A. W. Sleight, M. K. Jayaraj, J. Tate, Appl. Phys. Lett. 77 (2000) 1325-1326.

5. H. Yanagi, T. Hase, S. Ibuki, K. Ueda, H. Hosono, Appl. Phys. Lett. 78 (2001) 1583-1585.

6. J. P. Doumerc, A. Ammar, A. Wichainchai, M. Pouchard, P. Hagenmuller J. Phys. Chem. Solids 48 (1987) 37-43.

7. M. Shimode, M. Sasaki, K. Mukaida, J. Solid State Chem. 151 (2000) 16-20.

8. A. Draeseke, H. Yanagi, D. Tucker, D. Easley, D. H. McIntyre, J. Tate, J. Li, A. W. Sleight, Bull. Amer. Phys. Soc. 47 (2002) B23/13.

9. R. Hoppe, B. Schepers, H. J. Roehrborn, E. Vielhaber, Z. Anorg. Allg. Chem. 339 (1965) 130-143.

10. E. Hubbert-Paletta, R. Hoppe, G. Kruezburg, Z. Anorg. Allg. Chem. 379 (1970) 255-261.

11. M. Marezio, Acta Crystallogr. 18 (1965) 481-484; H. Mueller, R. Hoppe, Z. Anorg. Allg. Chem. 611 (1992) 73-80.

12. C. Sandonnini, Gazz. Chem. Ital. 44I (1914) 307.

13. M. Elazhari, A. Ammar, M. Elaatmani, M. Trari, J. P. Doumerc, Eur. J. Solid State Inorg. Chem. 34 (1997) 503-509.

14. R. J. Cava, H. W. Zandbergen, A. P. Ramirez, H. Takagi, C. T. Chen, J. J. Krajewski, W. F. Peck, Jr., J. V. Waszczak, G. Meigs, R. S. Roth, L. F. Schneemeyer, J. Solid State Chem. 104 (1993) 437-452.

15. R. D. Shannon, C. T. Prewitt, Acta Crystallogr. Sect. B 25 (1969) 925-929.

CHAPTER 4

TRANSPARENT P-TYPE CONDUCTING $BaCu_2S_2$ FILMS

Sangmoon Park, Douglas A. Keszler, Melinda M. Vaencia, Randy L. Hoffman,
Jeffrey P. Bender, and John F. Wager

Modified version: *Applied Physics Letters*, **80(23)**, 4393 (2002)

ABSTRACT

p-type conducting films of α-$BuCu_2S_2$ have been deposited onto glass and KBr substrates, yielding a conductivity of 17 S/cm and a Hall mobility of 3.5 $cm^2/V{\cdot}s$. For a 430-nm thick film, the optical transparency approaches 90% in the visible portion of the spectrum at 650 nm, and a transparency of 40% extends throughout the infrared to the long-wavelength cutoff of the KBr substrate at 23 μm.

INTRODUCTION

Wide band-gap oxides such as tin-doped indium oxide (ITO) and aluminum-doped zinc oxide (AZO) are well-known and widely used *n*-type transparent conductors. On the other hand, *p*-type materials with equivalent optical transparency and electrical conductivity are unknown, although efforts have recently been directed to the development of such materials on the basis of Cu compounds such as $CuAlO_2$,[1-4] $CuScO_{2+x}$,[5] $SrCu_2O_2$,[4] and LaCuOS.[6] In comparison with ITO and AZO, however, these Cu-based materials exhibit much lower figures of merit with respect to their transparency and conductivity. Conductivity in these systems is limited, in part, by low hole mobilities, which have been reported to be ≤ 0.4 $cm^2/V{\cdot}s$. The rather low conductivity, 0.01 S/cm, reported for LaCuOS thin films is somewhat surprising in view of the higher covalency of the Cu-S interactions in this compound relative to the Cu-O interactions in the oxides; higher covalency is expected to lead to broader bands, smaller effective masses, hence, higher mobilities and smaller dopant ionization energies, both of which should result in improved conductivity.[7] To examine this covalency issue in more detail and to determine whether improved mobilities can be observed in thin films of complex Cu sulfides, we have studied the preparation and electrical properties of the compound $BaCu_2S_2$.

$BaCu_2S_2$ crystallizes in a low-temperature orthorhombic form (α)[8] and a high-temperature tetragonal form (β);[9] in this work, we focus on the low-temperature compound. The structure is characterized by a three-dimensional linkage of CuS_4 tetrahedra that encapsulates the Ba atom in a seven-coordinate site. The CuS_4 tetrahedra are connected by sharing both vertices and edges. Interestingly, edge sharing results in a one-dimensional chain of tetrahedra and a short Cu···Cu distance of 2.71 Å shown (Fig. 4.1). For comparison, the shortest Cu···Cu interaction in the delafossite $CuAlO_2$ is 2.86 Å.[10] Short interatomic distances are desirable for obtaining materials with improved conductivity, since shorter distances result in broader bands and their associated transport advantages.[7]

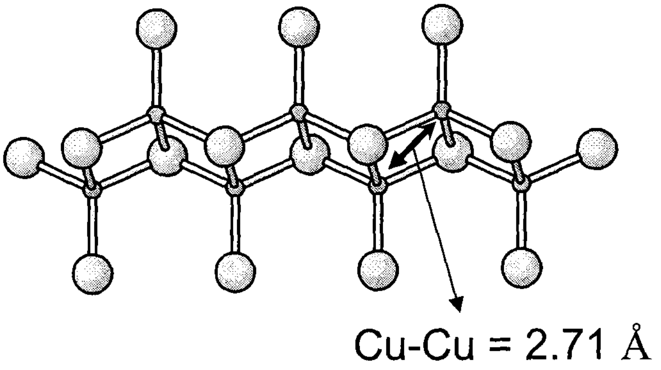

Figure 4.1. Structure of one-dimensional copper-sulfide chains in α-$BaCu_2S_2$. Small circles represent Cu atoms, and large circles represent S atoms.

EXPERIMENTAL

Thin films were deposited onto glass and KBr substrates by RF sputtering with a sintered-target disk and a gas mixture of Ar/He (60%/40%) at 35 mTorr and 80 sccm. The substrate was maintained at 573 K, and following deposition, the film was annealed in Ar at the same temperature for an additional five min. The 50-cm diameter target of $BaCu_2S_2$ was fabricated by pressing a powder at 4 tons and then annealing at 1048 K for 5 h in an Ar atmosphere. The powder was prepared by heating a mixture of the reagents $BaCO_3$ (Cerac, 99.9%) and Cu_2S (Cerac, 99.5%) at 923 K for 1 h under a flowing stream of $H_2S(g)$ and then cooling to room temperature under flowing Ar(g).

Phase identification was accomplished by using a Siemens D-5000 X-ray diffractometer; film thickness was established with an Alpha-Step 500 surface profiler; surface topography was examined with a NanoScope III atomic-force microscope (AFM); carrier type was established by using a hot probe in conjuction with an HP 3457A multimeter; and electrical measurements were performed on films deposited with a cross-shaped mask to improve the quality of the Hall data. A Filmetrics F20-VIS diode array was employed to determine the transmission of the films in the visible portion of the spectrum, and a Nicolet 510P FT-IR spectrometer was used to determine transmission properties in the infrared.

RESULTS

As seen from the X-ray data in Figure 4.2, the film adopts the low-temperature, α form of $BaCu_2S_2$; no diffraction lines attributable to the high-temperature form are evident in the pattern. From AFM measurements, the surface of the film is found to be relatively smooth with a roughness of ±20 nm. Electrical measurements reveal a *p*-type conductivity of 17 S/cm, a mobility of 3.5 $cm^2/V \cdot s$, and a carrier concentration of $10^{19}/ cm^3$. The *p*-type conductivity is consistent with recent observations[11] of similar behavior in the α form of the powder, and the magnitude of the conductivity exceeds that of LaCuOS by a factor of 10^3. The mobility may be compared to values near 20 $cm^2/V \cdot s$ for a typical *n*-type transparent conductor such as ITO.[12]

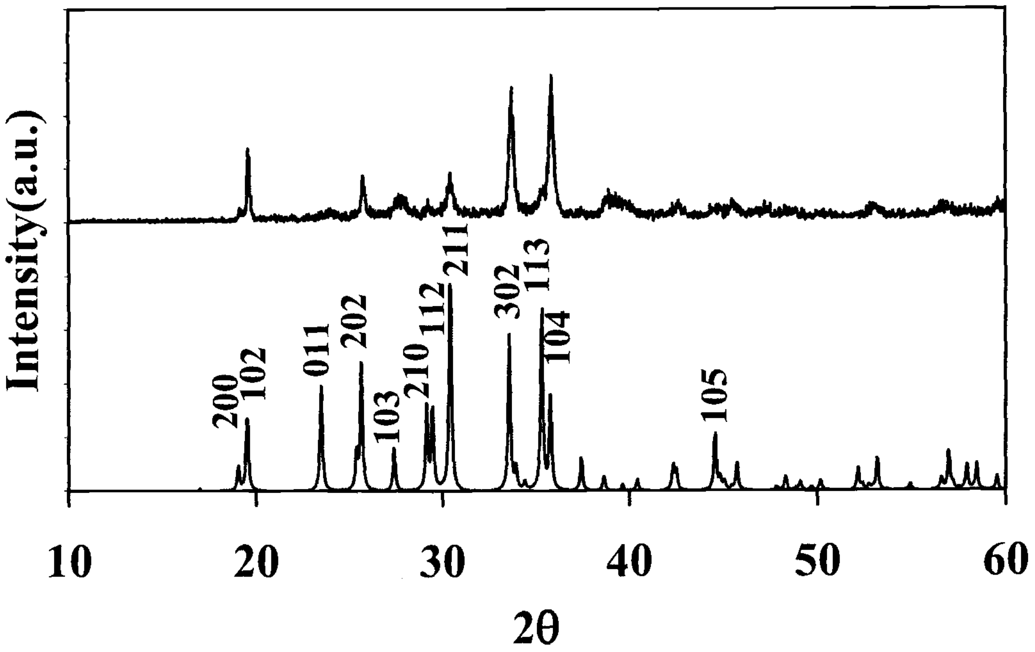

FIG. 4.2. (a) Calculated and (b) observed X-ray diffraction patterns of thin-film α-$BaCu_2S_2$.

As shown in Figure 4.3, prior to the band edge near 540 nm, the film exhibits a transparency near 70% with a maximum of 90% at 650 nm. By using extrapolation methods[13] for direct and indirect character (Figure 4.3,) the band gap is estimated to be 2.3 eV. Because the material can be processed at low temperatures, it can be directly deposited onto KBr substrates. For a 430-nm thick film, a transmission near 40% extends to the long-wavelength cutoff of the substrate at 23 μm. Figure 4.4 shows $BaCu_2S_2$ films deposited on glass and KBr. Figure 4.5 shows the photograph of $BaCu_2S_2$ films on glass and KBr with ITO.

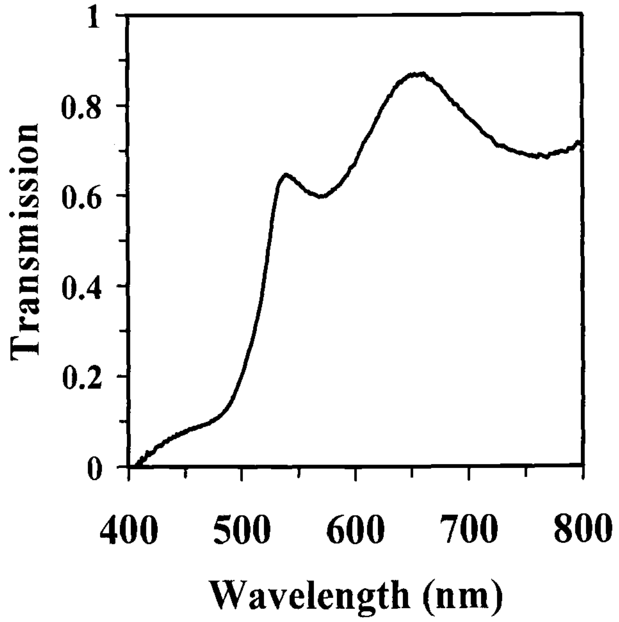

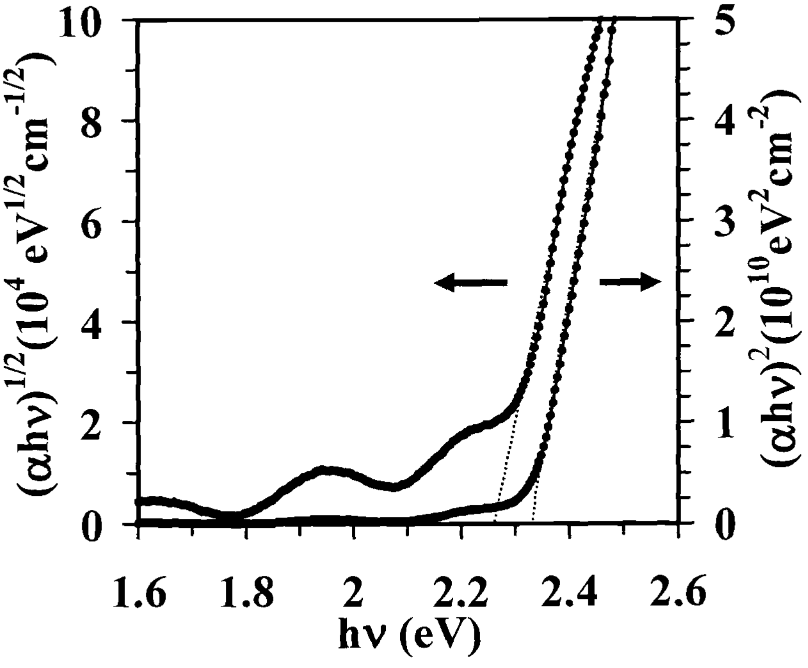

FIG. 4.3. (Top) Optical transmission spectrum of α-$BaCu_2S_2$ film in visible region. (Bottom) Estimate of band gap for indirect and direct character.

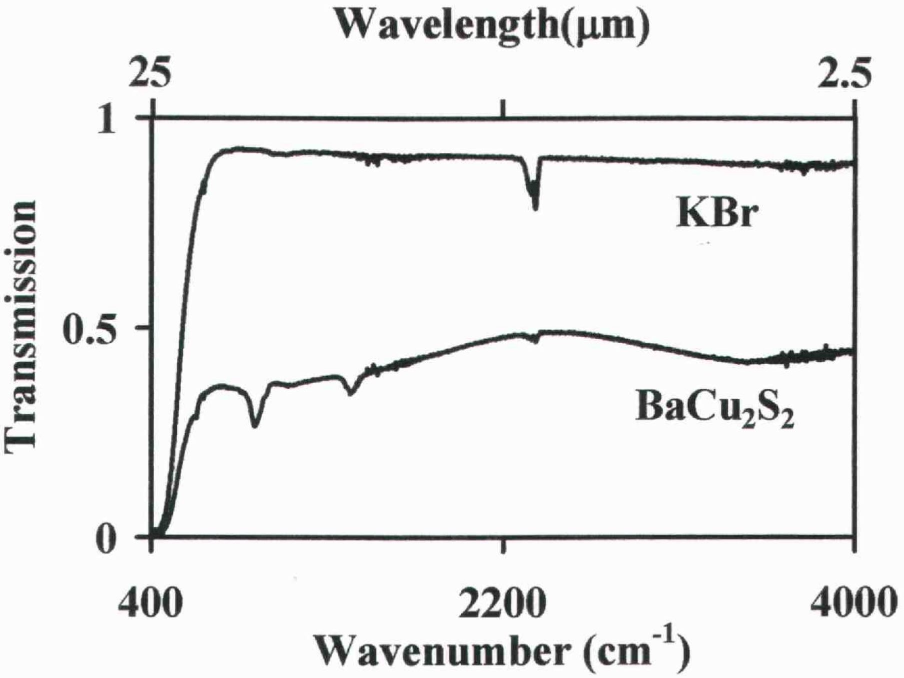

FIG 4.4. Optical transmission spectrum of α-$BaCu_2S_2$ film in infrared region.

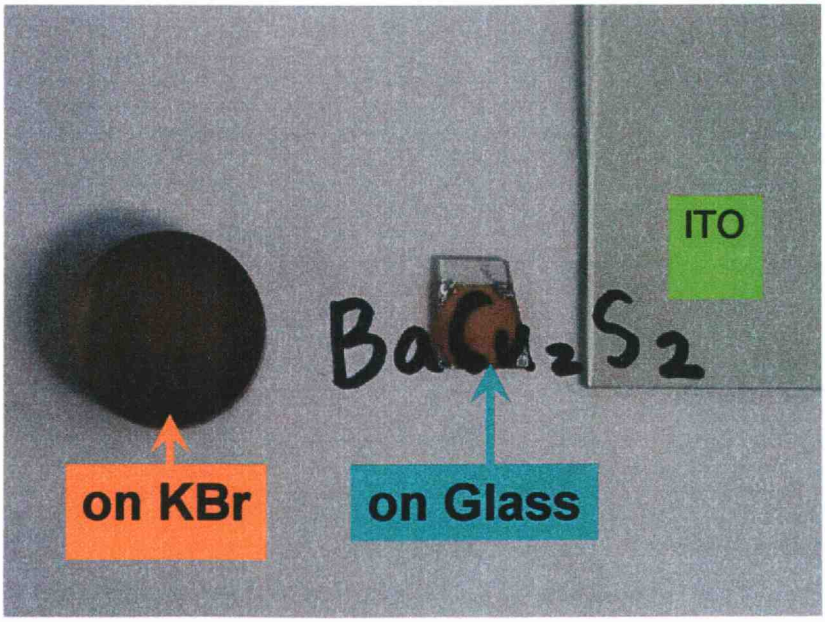

FIG. 4.5. The photograph of $BaCu_2S_2$ films on glass and KBr with ITO.

CONCLUSIONS

In summary, we have found that the low-temperature form of $BaCu_2S_2$ can readily be deposited in polycrystalline, thin-film form. A hole mobility of 3.5 $cm^2/V{\cdot}s$ and a conductivity of 17 S/cm have been measured for undoped material; higher conductivities should be attainable in appropriately doped samples. On the basis of other work performed in our lab, we believe that the limited conductivity of LaCuOS relative to $BaCu_2S_2$ may be related to defect formation associated with the high-temperature ($T = 1073$ K) processing of LaCuOS that is required for its formation and crystallization. Of course, $BaCu_2S_2$ exhibits a smaller band gap than LaCuOS (3.1 eV,) but we have recently identified other complex *p*-type conducting Cu sulfides with band gaps near 3 eV, which, like $BaCu_2S_2$, can be processed at relatively low temperatures ($T \sim 673$ K).

ACKNOWLEDGMENT

This work was funded by the US National Science Foundation under grant no. DMR-0071727 and by the Army Research Office under contract no. MURI E-18-667-G3.

REFERENCES

1. H. Kawazoe, M. Yasukawa, H. Hyodo, M. Kurita, H. Yanagi, and H. Hosono, Nature (London) **389**, 939 (1997).
2. H. Yanagi, S. Inoue, K. Ueda, H. Kawazoe, H. Hosono, N. Hamada, J. Appl. Phys. **88**, 4159 (2000).
3. R. E. Stauber, P. A. Parilla, J. D. Perkins, D. S. Grinley, Mater. Res. Soc. Symp. Proc. **623**, 265 (2000).
4. B. J. Ingram, T. O. Mason, R. Asahi, K. J. Park, and A. J. Freeman, Phys. Rev. B: Condens. Matter Mater. Phys. **64**, 155114/1 (2001).
5. N. Duan, A. W. Sleight, M. K. Jayaraj, and J. Tate, Appl. Phys. Lett. **77**, 1325 (2000).
6. A. Kudo, H. Yanagi, H. Hosono, and H. Kawazoe, Appl. Phys. Lett. **73**, 220 (1998).
7. P. A. Cox, *The Electronic Structure and Chemistry of Solids* (Oxford University Press, Oxford, 1987).
8. J. E. Iglesias, K. E. Pachali, and H. Steinfink, J. Solid State Chem. **9**, 6 (1974).
9. M. Saeki, M. Onada, and H. Nozaki, Mater. Res. Bull. **23**, 603 (1988).
10. T. Ishiguro, A. Kitazawa, N. Mizatani, M. Kato, J. Solid State Chem. **40**, 170 (1981).
11. T. Ohtani, H. Takeuchi, K. Koh, T. Kaneko, J. Alloys Compd. **317/318**, 201 (2001).
12. R. G. Gordon, MRS Bull. **25**, 52 (2000).
13. *Semiconductors and semimetals*, edited by R. K. Willardson and A. C. Beer (Academic, New York, 1967),Vol. 3, Chap. 6.

CHAPTER 5

α-, AND β-$BaCu_2S_2$ FILMS AND POWDERS

Sangmoon Park, Douglas A. Keszler, Melinda M. Valencia, and John F. Wager

ABSTRACT

X-ray diffraction patterns and atomic-force-microscope images of α- and β-$BaCu_2S_2$ thin films have been obtained for sample prepared at a variety of substrate and annealing temperatures. For β-$BaCu_2S_2$, a conductivity of 8 S/cm and optical transparency varying from 20 to 60 % in the visible were obtained for a 230-nm thick film. The low-temperature α form has been stabilized at all temperatures by substitution of Sr atoms for Ba atoms.

INTRODUCTION

$BaCu_2S_2$ crystallizes in a low-temperature orthorhombic form (α)[1] and a high-temperature tetragonal form (β);[2] the transition temperature is reported to be approximately 813 K. The structures of the two phases are depicted in Figure 5.1. Ba atoms are coordinated by seven and eight S atoms in the low- and high-temperature forms, respectively. Cu atoms are coordinated by four S atoms in both forms. The CuS_4 tetrahedra are connected by sharing both vertices and edges in the α form but only edges in the β form. In previous work,[3] we reported results on transparent p-type conducting α-$BaCu_2S_2$ films. In this study, α- and β-$BaCu_2S_2$ thin films have been fabricated at different substrate and annealing temperatures, and property measurements have been made. In addition stabilization of the α phase at all temperatures has been observed through substitution of Sr atoms for Ba atoms.

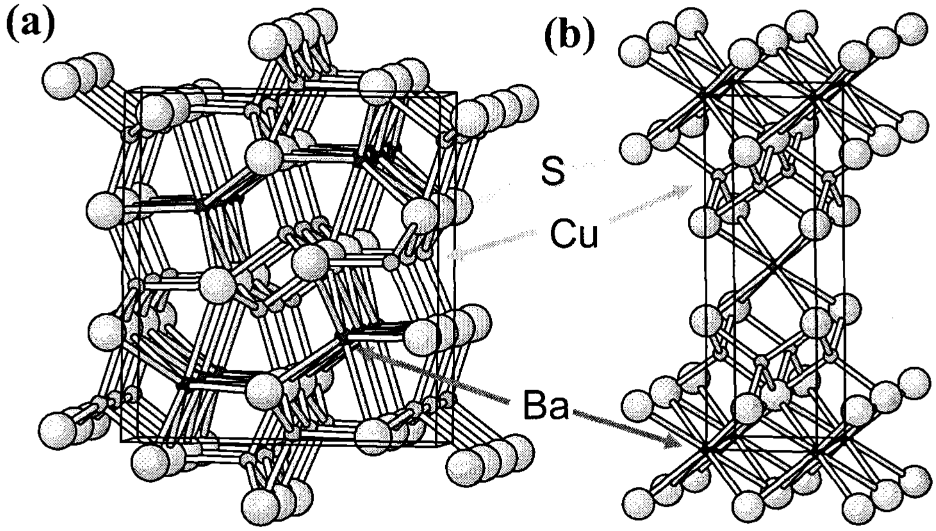

Figure 5.1. Structures of (a) α-$BaCu_2S_2$ and (b) β-$BaCu_2S_2$.

EXPERIMENTAL

Thin films were deposited onto glass substrates by RF sputtering with a sintered-target disk and a gas mixture of Ar/He (60%/40%) at 35 mTorr and 80 sccm. Products were examined from combinations of substrate and annealing temperatures of 573, 773, and 923 K. The 50-cm diameter target of β-$BaCu_2S_2$ was fabricated by pressing a powder at 4 tons and then annealing at 1048 K for 5 h in an Ar atmosphere. The powder was prepared by heating a mixture of the reagents $BaCO_3$ (Cerac, 99.9%) and Cu_2S (Cerac, 99.5%) at 923 K for 1 h under a flowing stream of $H_2S(g)$ and then cooling to room temperature under flowing Ar(g). By using the same method and the reagent $SrCO_3$ (Aldrich, 99.995%), samples in the series $Ba_{1-x}Sr_xCu_{1.8}S_2$ ($0 < x \leq 0.4$) were prepared.

Phase identification was accomplished by using a Siemens D-5000 and a Rigaku/Inel thin-film X-ray diffraction system. Film thickness was established with an Alpha-Step 500 surface profiler; surface topography was examined with a NanoScope III atomic-force microscope (AFM); and carrier type was established by using a hot probe in conjuction with an HP 3457A multimeter. A Filmetrics F20-VIS diode array was used to determine the transmission of the films in the visible portion of the spectrum.

RESULTS

In previous work,[3] low-temperature α-form films of $BaCu_2S_2$ were made by depositing and annealing material at 573 K, i.e., the film was processed below the α → β phase transition.[4] In this study, films were prepared at different substrate (T_S) and annealing (T_A) temperatures. Results are presented for the following processing conditions:

I - $T_S = 573$ K, $T_A = 573$ K

II - $T_S = 773$ K, $T_A = 573$ K

III - $T_S = 773$ K, $T_A = 923$ K

IV - $T_S = 573$ K, $T_A = 923$ K

Films I and II, both annealed at 573 K, but deposited at 573 and 773 K, respectively, were approximately 430-nm thick. Peaks in the X-ray diffraction patterns (Figure 5.2) are consistent with formation of the α phase, although the deposition temperature clearly affects the preferred orientation of the films, since the relative intensities of the two patterns differ. The substrate temperature also affects the surface texture, as the roughness for film I is approximately ± 20 nm, while that for film II is approximately ± 100 nm (Figure 5.3). Conductivities of 20 and 15 S/cm were obtained for films I and II, respectively. While deposition temperature has an observable effect on crystallite morphology and orientation, the conductivity appears to be largely unaffected.

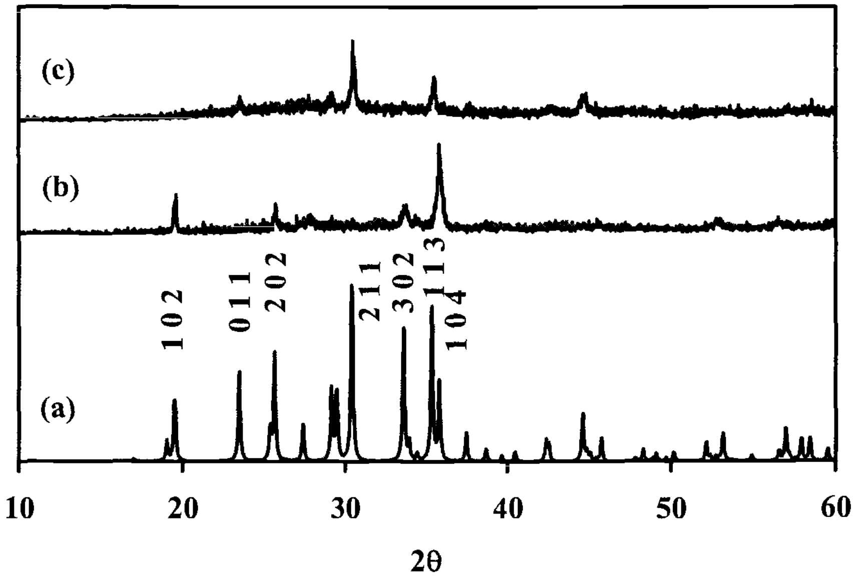

Figure 5.2. (a) Calculated powder X-ray pattern for a-$BaCu_2S_2$, (b) observed X-ray pattern for film I, and (c) observed X-ray pattern for film II.

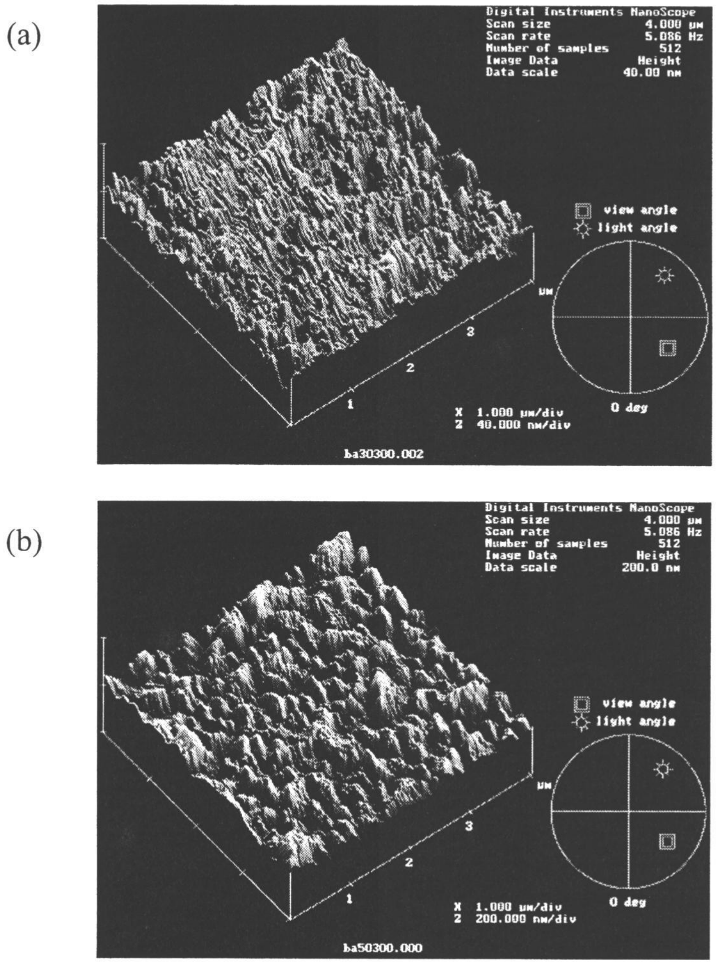

Figure 5.3. Atomic-force-microscope images for (a) film I and (b) film II.

Film III, deposited at the highest substrate and annealing temperatures, was approximately 230-nm thick; the film had a dark-brown color. As seen from the X-ray diffraction pattern in Figure 5.4, it is predominantly characterized as the β form of $BaCu_2S_2$, although a very significant quantity of BaS (asterisk) and an additional unidentified phase are present in the film. The extra diffraction lines do not coincide with those of the low-temperature α phase. Interestingly, the AFM image (Figure 5.5) reveals a substantial surface roughness and the presence of large grains, which could be associated with the phase separation. Electrical measurements reveal p-type behavior and a conductivity of 8 S/cm. Hole conductivity is consistent with observations of Zhang and co-workers.[5]

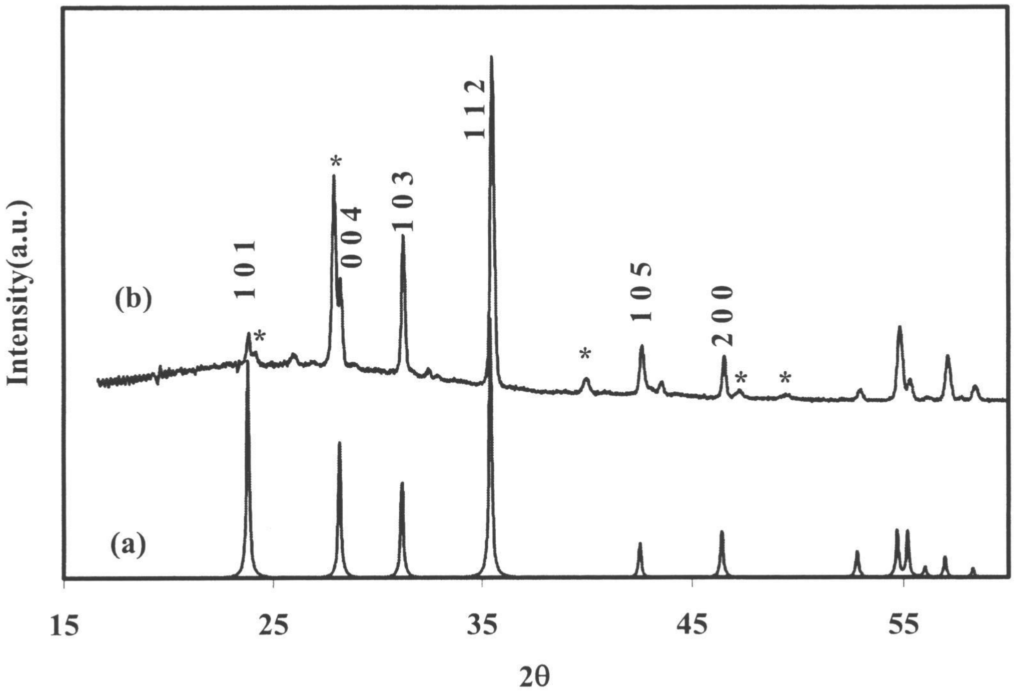

Figure 5.4. (a) Calculated powder X-ray pattern for β-$BaCu_2S_2$ and (b) observed X-ray pattern of film III.

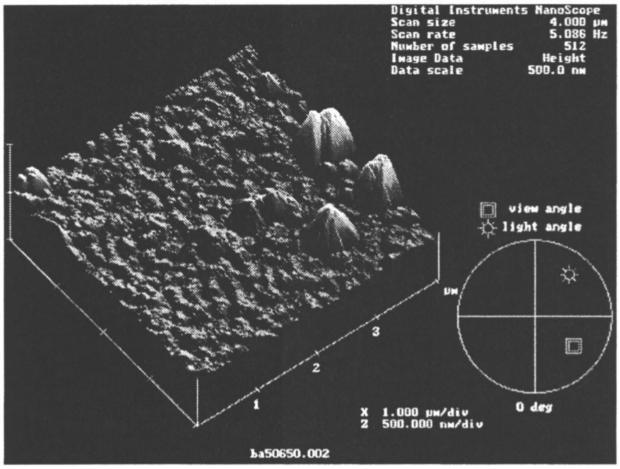
Digital Instruments NanoScope
Scan size 4.000 μm
Scan rate 5.086 Hz
Number of samples 512
Image Data Height
Data scale 500.0 nm

Figure 5.5. Atomic-force-microscope image of film III.

As seen in Figure 5.6, prior to the cutoff near 450 nm, the film exhibits a transparency near 20 % throughout much of the visible with a maximum of 60 % at 800 nm. By using extrapolation methods[6] for direct and indirect character (Figure 5.6) the band gap is estimated to be 1.8 eV. In view of the mixed-phase nature of the film and the unusual appearance of the transmission spectrum, I view these results with considerable skepticism as regards their direct application to the intrinsic properties of β-$BaCu_2S_2$. Additional powder and thin-film studies are required to clarify these findings.

No data could be collected on film IV. Following these processing conditions, the film always peeled off the substrate. Presumably, the low-temperature deposition leads to a film structure that is closely related to the α phase. On heating, this film undergoes the phase transformation and loses its grip on the substrate.

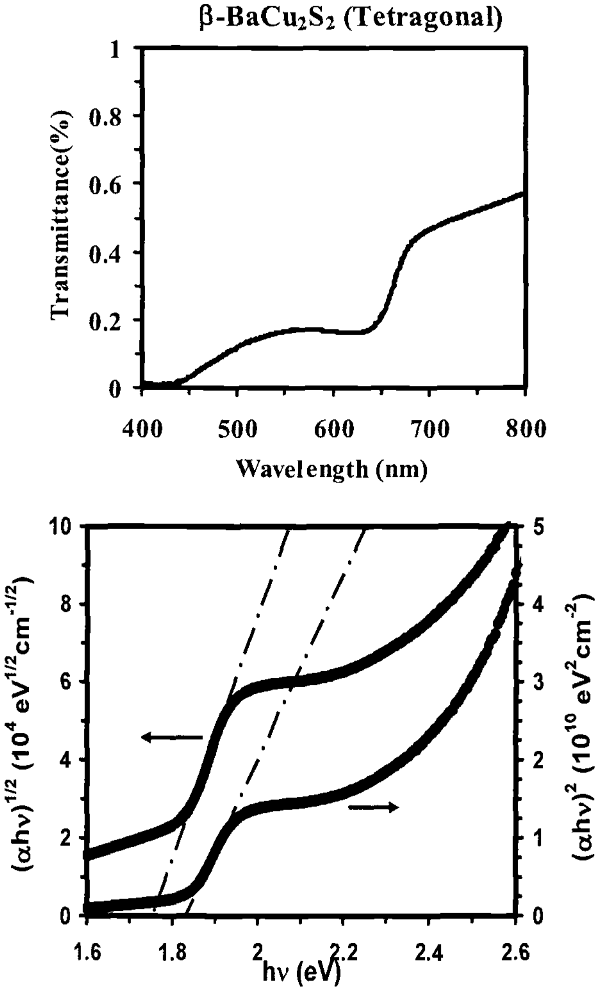

Figure 5.6. (Top) Optical transmission spectrum of film III in the visible region. (Bottom) Estimate of band gap for indirect and direct character.

As noted previously, Huster and co-workers have established a phase-transition temperature of 813 K for $BaCu_2S_2$.[4] The Ba atom is coordinated by seven and eight S atoms in low- and high-temperature forms, respectively, so stabilization of the α form is expected following substitution of Ba with a smaller alkaline-earth atom. The β- form is readily synthesized at 923 K with no evidence of the α- form in the X-ray diffraction pattern. Substitution of Ba with Sr at the same synthesis temperature, however, leads to stabilization of the α form. From determination of unit-cell volumes in the series $Ba_{1-x}Sr_xCu_{1.8}S_2$ $(0 < x \leq 0.4)$, the maximum substitution of Sr for Ba occurs at $x \approx 0.3$; beyond this value, the unit-cell volume does not change (Figure 5.7).

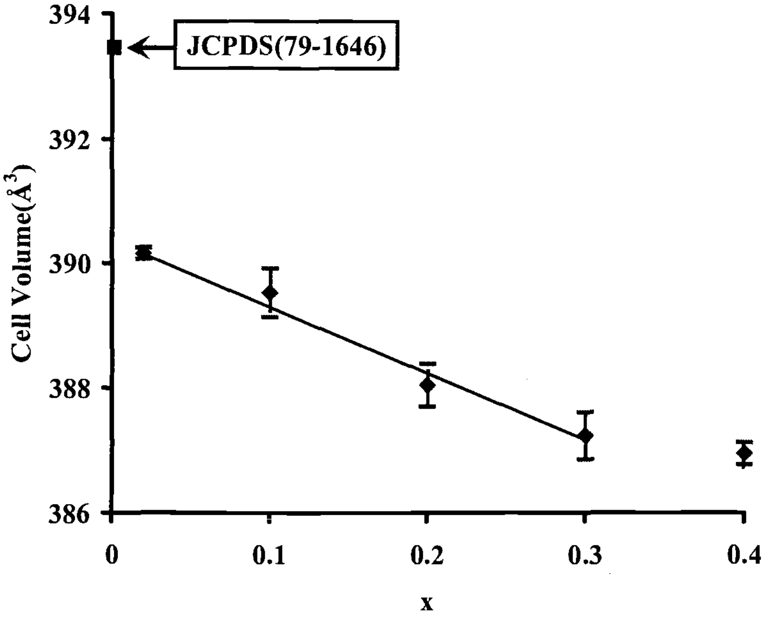

Figure 5.7. Unit-cell volumes for solid solution of $Ba_{1-x}Sr_xCu_{1.8}S_2$.

CONCLUSION

Low- and high-temperature forms of $BaCu_2S_2$ can be deposited on glass substrates by controlling deposition and annealing conditions. A conductivity of 8 S/cm and a band gap of 1.8 eV have been observed for a mixed phase β-$BaCu_2S_2$ thin film. More work, however, needs to be done to determine the intrinsic conducting properties of high-quality films and to firmly establish the band gap. The low temperature form of $BaCu_2S_2$ can be stabilized by substituting Sr atoms for Ba atoms.

REFERENCES

1. J. E. Iglesias, K. E. Pachali, and H. Steinfink, J. Solid State Chem. **9**, 6 (1974).
2. M. Saeki, M. Onada, and H. Nozaki, Mater. Res. Bull. **23**, 603 (1988).
3. S. Park, D. A. Keszler, M. M. Valencia, R. L. Hoffman, J. P. Bender, and J. F. Wager, Appl. Phys. Lett., **80(23)**, 4393 (2002).
4. J. Huster and W. Bronger, Z. Anorg. Allg. Chem., **625**, 2033-2040 (1999).
5. X. Zhang, T. Hogan, C. R. Kannewurf, and M. G. Kanatzidis, J. Alloys Compd., **236**, 1 (1996).
6. *Semiconductors and semimetals*, edited by R. K. Willardson and A. C. Beer (Academic, New York, 1967),Vol. 3, Chap. 6.

CHAPTER 6

THE POWDER AND THIN FILM STUDIES FOR BaCuSF

Sangmoon Park, Cheol-Hee Park, Douglas A. Keszler,
Hiroshi Yanagi, and Janet Tate

ABSTRACT

The conductivities, Seebeck coefficients, and intensities of pellets of the series $Ba_{1-x}K_xCuSF$ ($0 \leq x \leq 0.1$) were measured. The band gap for BaCuSF is estimated to be 3.4 eV. The p-type conducting films of BaCuSF nominally doped with K have been deposited on glass substrates, yielding a conductivity of 0.12 S/cm. For a 370-nm-thick film, the optical transparency approaches 90 % in the visible region of the spectrum at 750 ~ 900 nm. BaCuSF emits orange-red color under both photo- and cathodoexcitation.

INTRODUCTION

In previous work,[1] we observed p-type conductivity in α-$BaCu_2S_2$ with E_g = 2.3 eV. To extend these results to higher band-gap materials requires limiting band dispersion, which appears to be possible by reducing dimensionality. α-$BaCu_2S_2$, for instance, exhibits a three dimensional linkage of distorted CuS_4 tetrahedra. In the oxide sulfide LaCuOS,[2] the distorted CuS_4 tetrahedra are confined to a plane, and consequently the band gap is raised to 3.1 eV.

EXPERIMENTAL

Powder Synthesis and Characterization

Powdered samples of BaCuSF were prepared by heating stiochiometric mixtures of the reagents BaF_2 (Cerac 99.9%), Cu_2S (Cerac 99.5%), and BaS at 723 K for 15 h in sealed silica tubes or the reagents of $BaCO_3$ (Cerac 99.9%), Cu_2S, and BaF_2 at 823 K for 1 h under flowing stream of H_2S (g) and cooling to room temperature under flowing Ar (g). For K-doped BaCuSF powder, the reagents BaF_2, Cu_2S, BaS, KF (Alfa 99%), Cu (AESAR 99.9%), and S (Cerac 99.999%) were used. The half-inch pellets of un-doped and K-doped BaCuSF were fabricated by pressing a powder at 4.5 tons and then annealing at 923 K for 30 min in evacuated silica tube. BaS powder was prepared by heating $BaCO_3$ at 1023 K for 1 h as same as the synthesis method of BaCuSF powder for gas flowing.

Phase identification was accomplished by using a Siemens D-5000 and Philips X-ray diffractometers. Cathodoluminescence and photoluminescence for BaCuSF were performed in Hewlett-Packard Company and our laboratory, respectively. Excitation provided by an Oriel 300 W Xe lamp was passed through a 50-cm water filter, focused onto the entrance slits of a Cary model-15 prism monochromator, and then onto the sample. Luminescence was collected at a near right angle to excitation light, dispersed through an Oriel 22500 1/8 – m monochromator with interchangeable gratings. Hamamatsu R636 photomultiplier tube was used for detecting emission. The signal was collected and amplified with a Keithley model 602 picoammeter and then converted to a digital signal for computer acquisition. The emission was corrected with a tungsten lamp.

Thin Film Deposition and Characterization

Thin films were deposited on glass substrates by thermal evaporation of BaF_2 and Cu at a pressure near 1×10^{-5} Torr. For K-doped films, KF was used as a source of K. The substrate was maintained at 473 K during deposition, and the films were then sulfurized under a flowing stream of H_2S (g) at 623 K for 3 h. Film thickness was established with an Alpha-Step 500 surface profiler; carrier type was established by using a Seebeck coefficient measurement; and electrical measurements were made with a four-probe technique. A Xe lamp and double monochrometer (ORIEL) was employed to determine the transmission of the films in the visible portion of the spectrum. A Siemens D-5000 X-ray diffractometer was used for phase identification of films.

RESULTS

As seen from the fully indexed X-ray pattern of Figure 6.1, single-phase BaCuSF powders can be produced at a relatively low temperature (T = 723 K). K-doped samples are produced in like manner.

Results of electrical measurements of K-doped pellets are summaried in Figure 6.2. These phases exhibit an increasing conductivity with dopant concentration, extending from 0.1 S/cm for BaCuSF to approximately 80 S/cm for $Ba_{0.9}K_{0.1}CuSF$. Seebeck coefficients for all samples are positive (Figure 6.2), indicating p-type behavior. The unusul trend in these coefficients noted for the range x = 0 ~ 0.5 requires additional investigation. The coefficient for x = 0 could too small, considering the low conductivity of this sample. Additional pellets will be prepared to determine if this trend is reproducible.

Thin films were prepared by evaporation of BaF_2 and Cu metal followed by heat treatment under flowing H_2S (g). The X-ray pattern (Figure 6.3) contains only diffraction peaks that overlap those of the BaCuSF powder. Because of a small shift of the (101) and (203) reflections relative to those observed in the powder, it is difficult to specifically assign the peak near 29° to the (102) or (003) reflection.

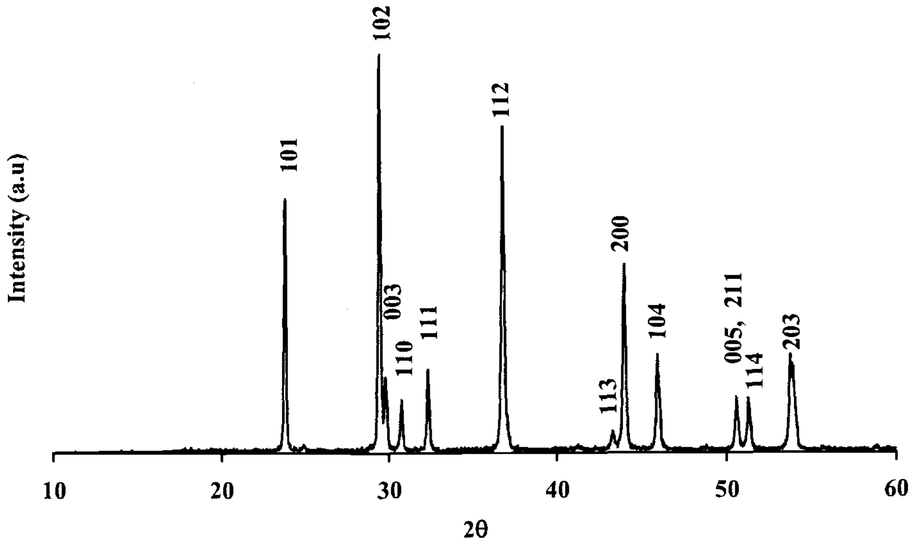

Figure 6.1. X-ray powder patterns of BaCuSF (tetragonal cell, a = 4.123(1) Å and c = 9.021(1) Å).

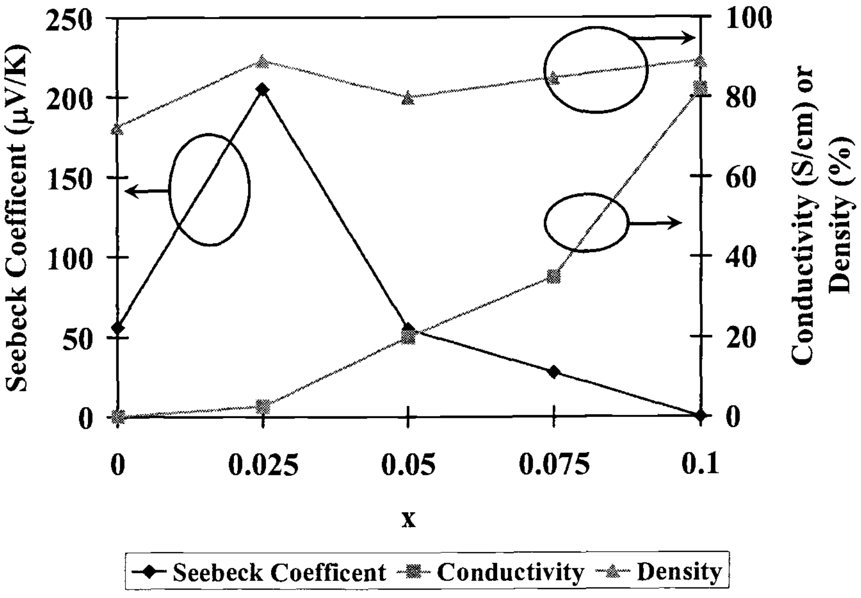

Figure 6.2. The plot of conductivities, Seebeck coefficients, and theoretical densities vs. x for $Ba_{1-x}K_xCuSF$.

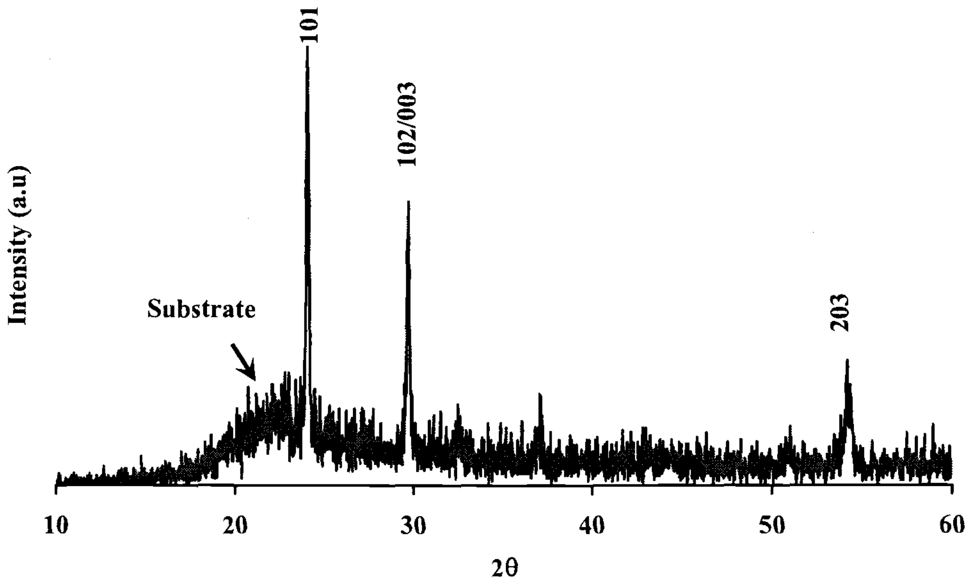

Figure 6.3. Thin-film X-ray diffraction pattern of BaCuSF.

The optical transmission spectrum is shown in Figure 6.4; transmittance varies from approximately 70 to 90 % across the visible. From extrapolation methods, the band gap is estimated to be 3.4 eV. The transmission spectrum for a film nominally doped with K is given in Figure 6.5. The spectrum is quite similar to that of the undoped sample; the room-temperature conductivity of this film is 0.12 S/cm.

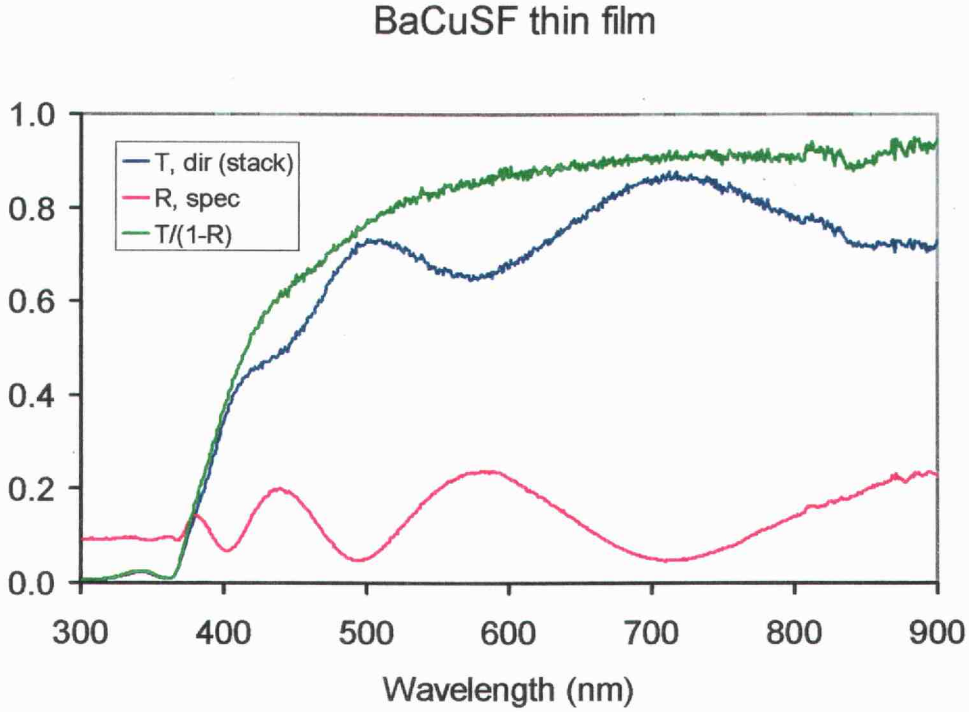

Figure 6.4. Optical transmission spectrum for BaCuSF: T is transmission of film and substrate and R is reflection of film and substrate stack.

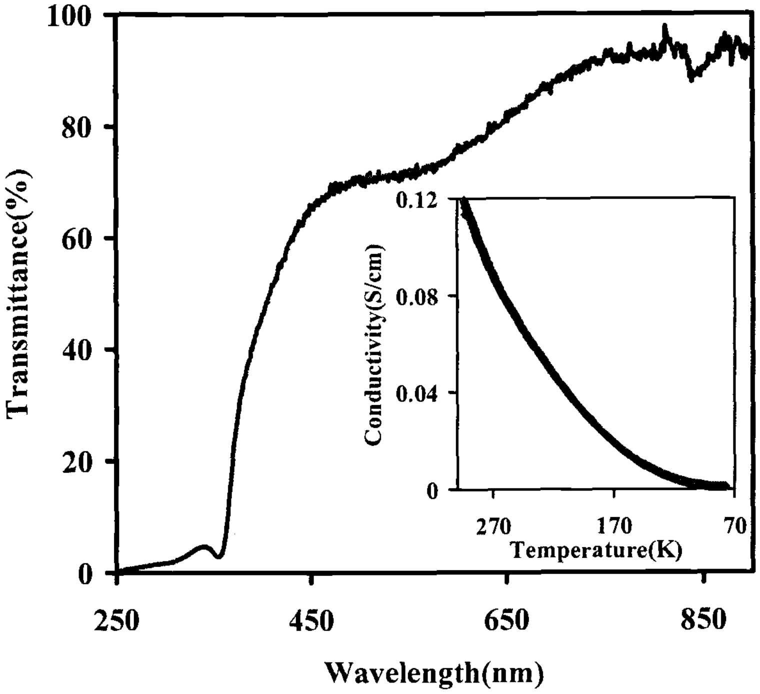

Figure 6.5. The optical transmission spectrum of BaCuSF film nominally doped with K. (Inside) Temperature dependence of electrical conductivity of K:BaCuSF thin film.

Powders of BaCuSF have also been found to emit orange-red light following photoexcitation at energies above the band gap. A similar spectrum is observed from cathodoexcitation (Figure 6.6). A pressed pellet of the material (Figure 6.7) was used for this cathodoluminescence experiment; the pellet exhibited a range of grain sizes with an average size near 2 μm. The cathodoluminescence is easily observed at the lowest voltage setting (900 V) on the SEM. The chromaticity coordinates are x = 0.58 and y = 0.41, which may be compared to the values x = 0.654 and y = 0.346 for the saturated red phosphor Eu:Y_2O_3.

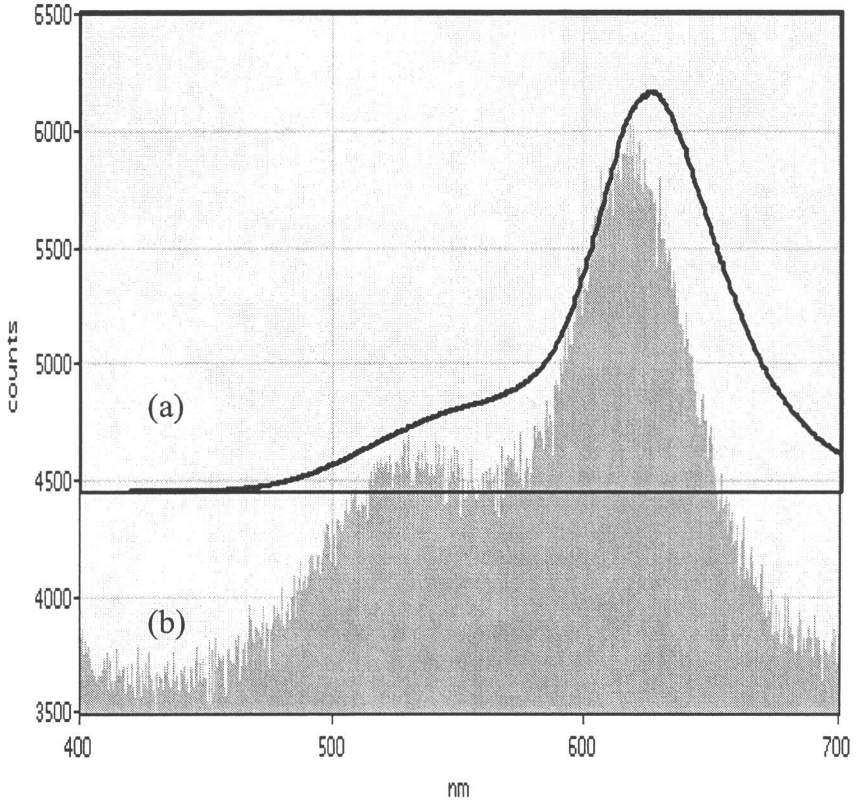

Figure 6.6. The emission spectra from BaCuSF under (a) photoexcitation and (b) cathodoexcitation.

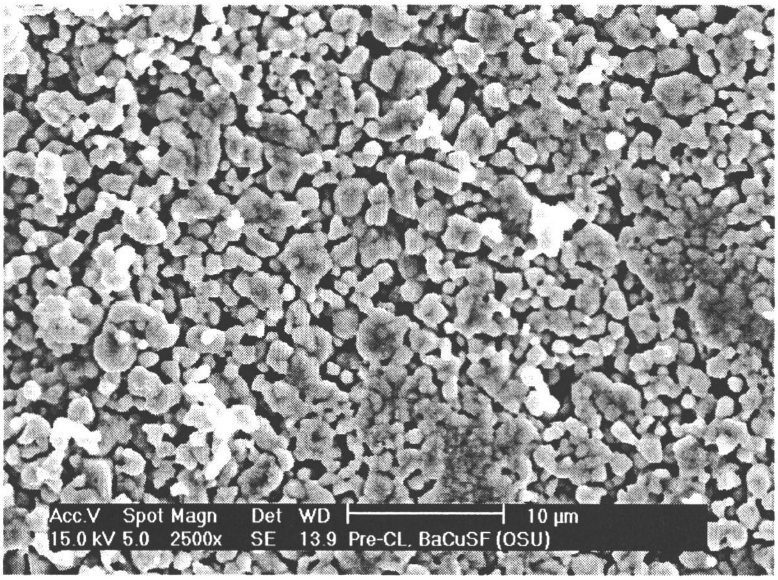

Figure 6.7 SEM image of the region where CL images were taken.

DISCUSSION

From reported structural refinements and comparison of X-ray diffraction patterns, BaCuSF is isostructural to the tetragonal materials LaCuOS and BaCuSeF[3] (Figure 6.8). The structure may be characterized as a two-dimensional condensation of edge-sharing distorted CuS_4 tetrahedra that are separated by two Ba layers interleaved by a layer of F atoms. The Ba atom is coordinated by four S atoms and four F atoms in a distorted cubic antiprism.

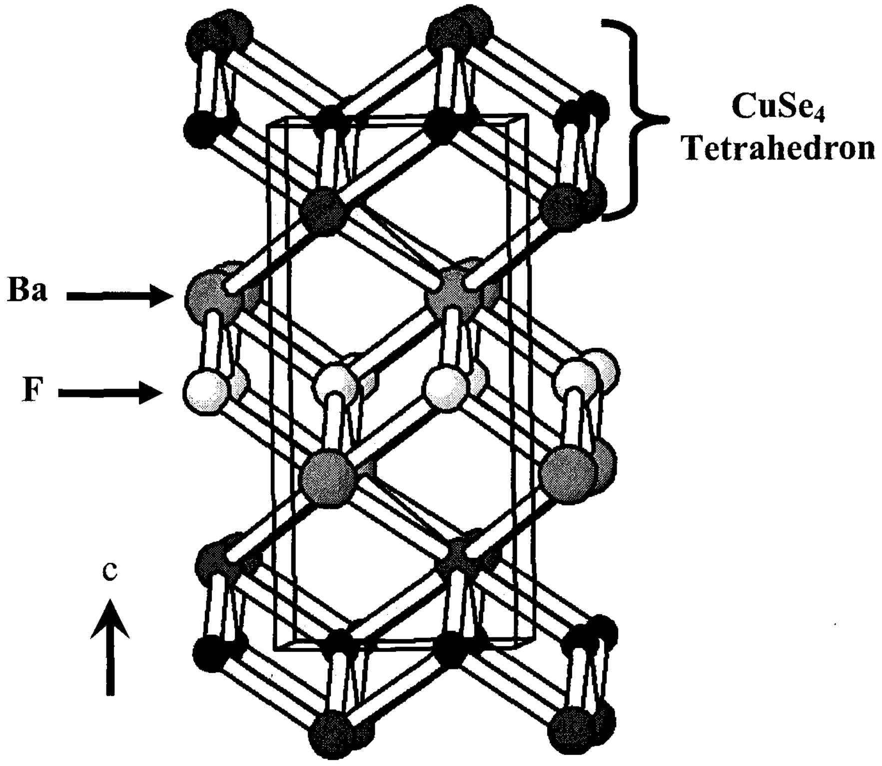

Figure 6.8. The structure of BaCuSeF. Small dark circles represent Cu atoms, medium dark circles represent Se atoms, medium blank circles represent F atoms, and large circles represent Ba atoms.

Conductivity is expected to be associated with the CuS sheets in the material. Substitution of K for 10 % of the Ba atoms leads to oxidation of the sheets, p - type conductivity, and an increase in conductivity by a factor of nearly 10^3 in pressed pellets.

The available thin-film data are very useful for establishing the band gap, 3.4 eV, of the undoped material. While the X-ray data are consistent with the film formation of BaCuSF, it is difficult to believe that the film is single phase. Since the films were made by evaporation of BaF_2 and Cu metal, the F:Ba ratio in the films should be too high. We know from bulk studies that there is no reaction between BaF_2 and H_2S (g) at elevated temperatures. In some films, residual BaF_2 has been observed. In any event, this excess BaF_2 ($E_g = 9$ eV) will have no effect on assessing the gap of BaCuSF. The band-gap measurement is also consistent with recent excitation measurements associated with the luminescence. The presence of excess BaF_2 in the grain boundaries of the films, however, could have significant effects on conductivity measurements.

Since the structure exhibits two dimensionality, film conductivity could be affected by preferred orientation, i.e., a [001] orientation of the film orthogonal to the substrate might be expected to produce the highest conductivity. Diffraction provides limited evidence for preferred orientation in the powder, and electron-microscope images do not reveal a plate-like morphology for the grains. It is difficult to fully interpret the current thin-film X-ray data in this regard, because of difficulty in assigning the (003) reflection in the pattern.

The visible luminescence of BaCuSF is a unique aspect of the material. The emission is well removed energetically from the excitation (band gap) levels. Two features are clearly evident in the emission spectrum - one band near 550 nm in the green and the other, major band at 620 nm in the red. The combination of these bands leads to an orange emission. The origins of the emission features are still under examination, but we do know that selective doping can quench the 550-nm band, leading to a saturated red emission equivalent to that of $Eu:Y_2O_3$.

SUMMARY

Measurements on pressed pellets of $Ba_{1-x}K_xCuSF$ ($0 \leq x \leq 1$) have been used to establish the material as a p-type conductor with conductivies ranging from 0.1 S/cm (x = 0) to 80 S/cm (x = 0.1). A band gap of 3.4 eV has been derived from optical transmission studies of undoped BuCuSF. The compound also exhibits an orange-red luminescence under photo- and cathodoexcitation. Considering these results, the system BaCuQF (Q=S, Se, Te) is an interesting family of materials for the continued development of p-type transparent conductors.

REFERENCES

1. S. Park, D. A. Keszler, M. M. Valencia, R. L. Hoffman, J. P. Bender, and J. F. Wager, Appl. Phys. Lett., **80(23)**, 4393 (2002).

2. A. Kudo, H. Yanagi, H. Hosono, and H. Kawazoe, Appl. Phys. Lett. **73**, 220 (1998).

3. W. J. Zhu, Y. Z. Huang, F. Wu, C. Dong, H. Chen, and Z. X. Zhao, Mat. Res. Bull., **29(5)**, 505 (1994).

4. K. Ueda, S. Inoue, H. Hosono, N. Sarukura, and M. Hirano, Appl. Phy. Lett., **78(16)**, 2333 (2001).

5. H. Krakauer, M. Posternak, and A. J. Freeman, Phys. Rev. B, **19(4)**, 1706 (1979).

6. E. Wimmer, H. Krakauer, M. Weinert, and A. J. Freeman, Phys. Rev. B, **24(2)**, 864 (1981).

CHAPTER 7

(I) PHASE STABILIZATION OF In_2Se_3 POLYMORPHS (II) ELECTRICAL CONDUCTING OF DOPED In_2Se_3 AND Sb_2Te_2Se FILMS

Sangmoon Park, Douglas A. Keszler,
Randy L. Hoffman, Melinda M. Valencia, and John F. Wager

ABSTRACT

α- In_2Se_3, β-, γ- In_2Se_3, and γ- In_2Se_3 phases were observed at 673, 973, and 1223 K, respectively. α- and β- phases were synthesized and stabilized at all temperatures by Ga and Bi, Sb, or I cation alloying, respectively. *n*-, *p*-Type conducting films of I:In_2Se_3 and Sb_2Te_2Se have been deposited onto glass and Si substrates, yielding conductivities of 55, 1000 S/cm and Hall mobilities of 50, 190 $cm^2/V{\cdot}s$, respectively.

INTRODUCTION

Indium selenide, In_2Se_3, is a wide band-gap semiconductor, $E_g = 1.7$ eV, of considerable technological interest for use in electronic devices. Its use, however, is complicated by the polymorphic nature of the material. Indeed, there are many confusing and contradictory reports in the literature regarding its structure chemistry.[1-15] For example, Ye, Soeda, Nakamura, and Nittono recently proposed a simple vacancy-ordered wurtzite structure for the low-temperature form and a highly unusual layered-type structure having a Se atom with a coordination number = 1.[16]

Perhaps the most comprehensive study of In_2Se_3 phase has been presented by Lutz, Fisher, Baldus, and Blachnik.[17] The α phase, stable at room temperature, contains In atoms in 4- and 5-fold coordination, and it is isostructural to $InGaSe_3$.[18] Above 960 K α undergoes a phase transition to β and above 1080 K, an additional transformation occurs to the γ phase. On cooling the γ phase, several different metastable phases have been observed, not likely representing different stacking sequences of the β and γ structure types. Up to now, only the α and γ forms have been stabilized at room temperature.

In this work, we perform bulk doping studies on In_2Se_3. The purpose is twofold: (a) monitor the resulting electrical properties and (b) stabilize a selected polymorph. Along the way, we hoped to develop a better understanding of the structure chemistry of In_2Se_3. As the work progressed, we were led to consider the structure and properties of Sb_2Te_2Se and results on this material are present as well.

EXPERIMENTAL

Powdered samples of In_2Se_3:M (M=Bi, Sb, I), In_2Se_3:Ga, and Sb_2Te_2Se were prepared by heating stoichiometric mixtures of the reagents In (Alfa, 99.99%,) Se (Alfa, 99.999%,) Ga (Cerac, 99.99%,) Bi (Alfa, 99.999%,) Sb (Alfa, 99.999,) I_2 (Fisher Scientific), and Te (Alfa, 99.99%) at 1223, 1023, and 973 K, respectively, for 1d in evacuated and sealed silica tubes. Phase identification was accomplished by using Siemens D-5000 and Phillips X-ray diffractometers equipped with Cu Kα radiation. Thin films of Sb_2Te_2Se were deposited onto glass substrates by thermal evaporation of single-source Sb_2Te_2Se powders at a deposition pressure of 2×10^{-5} Torr. The substrate was maintained at 473 K, and following deposition, the films were annealed in Ar at 573, 673 and 773 K. Film thickness was established with an Alpha-Step 500 surface profiler; carrier type was established by using a hot probe in conjunction with a HP 3457 A multimeter; and electrical measurements were performed on films with Hall measurement.

RESULTS

X-ray diffraction patterns for In_2Se_3 prepared at selected temperature over a period of one week are given in Figure 7.1. Calculated and reported X-ray diffraction patterns for α-, β-, γ-, and $InGaSe_3$ are also provided. At 673 K, as expected, the pattern corresponds to the low-temperature α phase. At 973 and 1223 K, the patterns correspond to mixtures of β and γ phases of JCPDS entries.

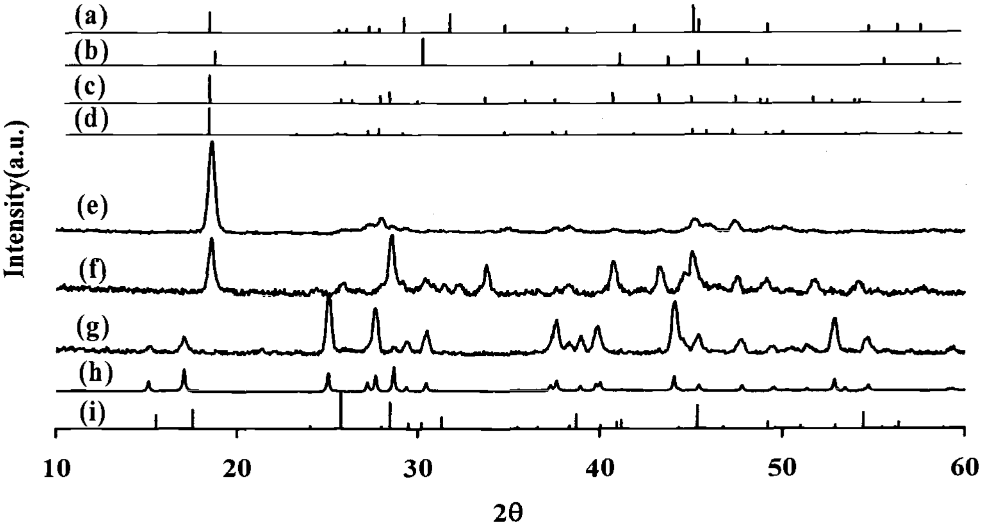

Figure 7.1. (a) β-In_2Se_3 JCPDS 40-1408 (Hex), (b) β-In_2Se_3 JCPDS 45-1041 Rhomb), (c) γ-In_2Se_3 JCPDS 34-0455 (Rhomb), (d) γ-In_2Se_3 JCPDS 34-1279 (Hex), (e) the powder pattern of In_2Se_3 at 1223 K, (f) the powder pattern of In_2Se_3 at 973 K, (g) the powder pattern of In_2Se_3 at 673 K, (h) α-In_2Se_3 ICSD 1376, (i) $InGaSe_3$ JCPDS 78-1745.

Initial experiments were directed to stabilization and study of the α phase. As noted in the Introduction, this material has been reported to contain a mixture of 4- and 5- coordinate In atoms. It is isostructural to $InGaSe_3$ wherein there is an ordering of In atoms on the 5-coordinate site and Ga on the 4-coordinate site (Figure 7.2). The α phase should be stabilized relative to transformation to the β an γ phases following the substitution of a small amount of Ga for In, since small Ga atom prefers a 4-coodinate site. Indeed, substitution of only 5 at% Ga into In_2Se_3 results in retention of the α phase at least to the synthesis temperature of 1023 K. As noted in the X-ray pattern (Figure 7.3), a small amount of the high-temperature phase retained in the product. Prolonged annealing of the sample may lead to complete conversion to the α phase. For 25 at% Ga and higher, only the α phase is observed. Quantitative data on the unit-cell parameters are summarized in Figure 7.4. The unit-cell volume undergoes a smooth contraction with increasing Ga doping with relative contract ions along the *a* and *c* axes being only slightly different. Cell lengths *a* and *c* for a given value of x (Ga doping concentration) with relationships $a = -0.1659x + 7.1296$ and $c = -0.4164x + 19.377$.

Since the stoichiometry $In_{1.75}Ga_{0.25}Se_3$ was consistently observed to for α-phase product only, it was selectively doped with numerous n- and p- type dopants. In all cases, the resistance of pressed pellets of the doped samples was equivalent of usually higher than the undoped pellets, indicating the dopants are compensated through defect formation rather than producing charge carries.

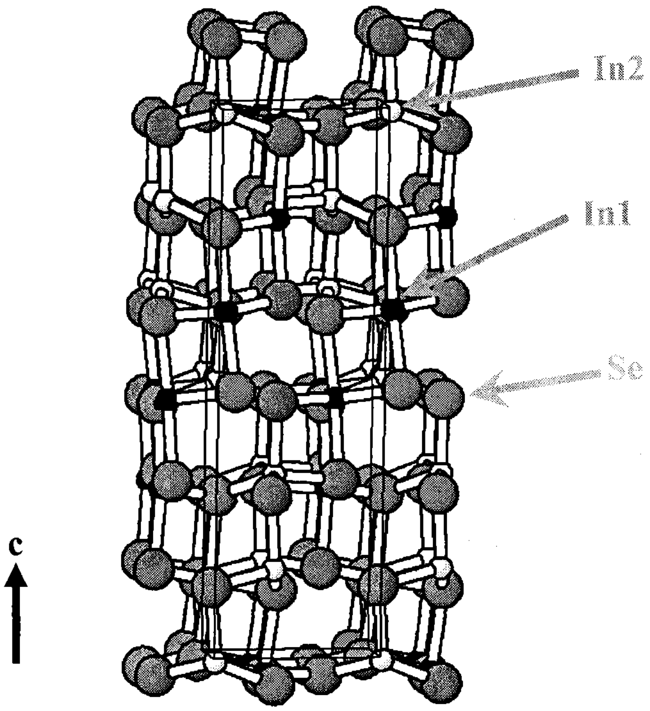

Figure 7.2. The structure of α-In_2Se_3 and $InGaSe_3$. Small dark and open circles represent In atoms, and large circles represent Se atoms. The In2 site corresponds to Ga in $InGaSe_3$.

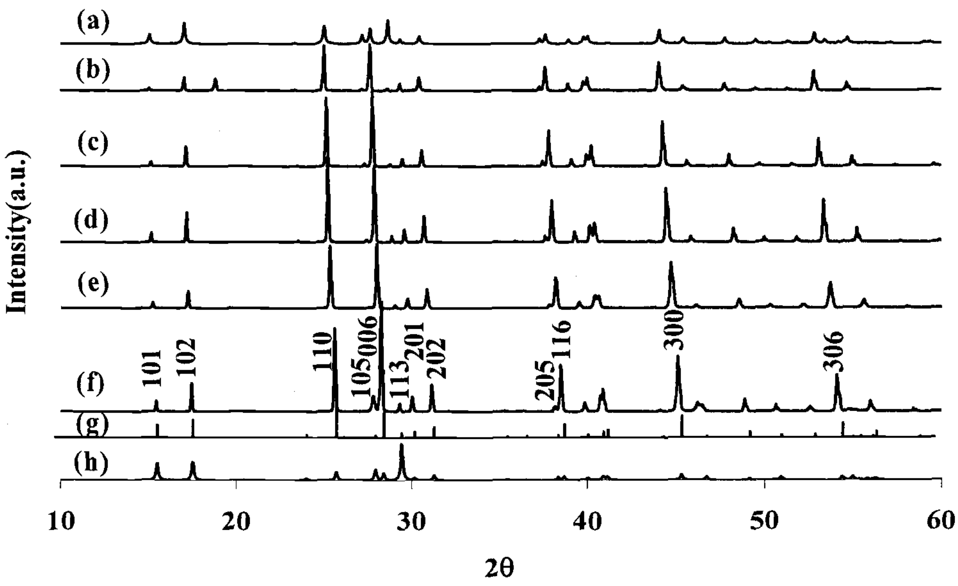

Figure 7.3. The X-ray patterns of $In_{1-x}Ga_xSe_3$ (x = 0.05 ~ 1) (a) γ-In_2Se_3 ICSD 1376, (b) x = 0.05, (c) x = 0.25, (d) x = 0.5, (e) x = 0.75, (f) x = 1, (g) $InGaSe_3$ JCPDS 78-1745, (h) $InGaSe_3$ ICSD 62930.

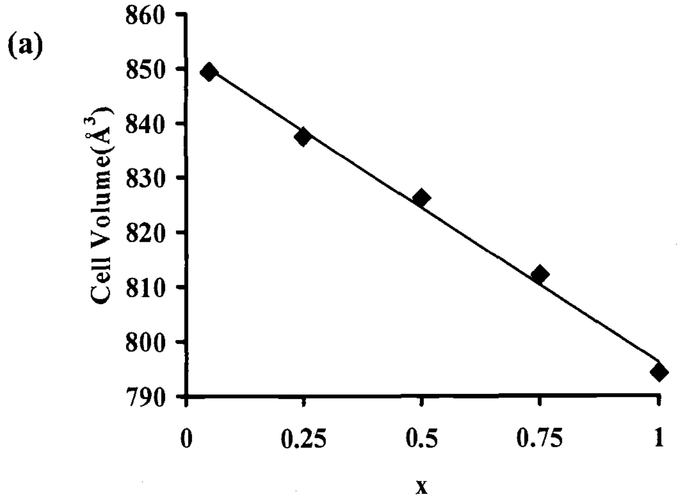

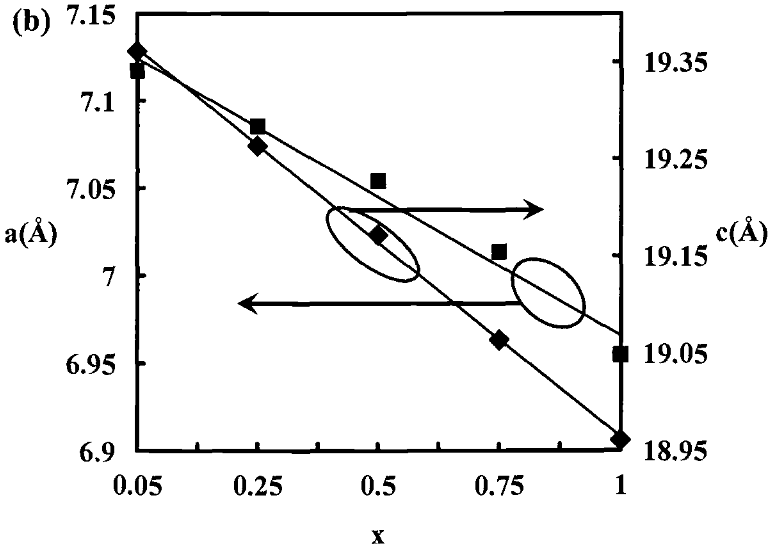

Figure 7.4. (a) Cell volume of $In_{2-x}Ga_xSe_3$ for x = 0.05 to1 (b) plot of cell lengths *a* and *c*.

Some additional observations have been made with regard to In_2Se_3 phases. By heating stoichiometric samples for only one day, the hexagonal form of the high-temperature structure is formed (Figure 7.5 e). Heating a mixture that is Se deficient ($In_2Se_{2.9}$) leads to formation of the hexagonal, γ phase (Figure 7.5 f). β-phase preference is observed with the nominally n-type dopants, I, Sb, and Bi (Figure 7.5). Presumably these dopants lead to Se vacancies and stabilization of the β phase.

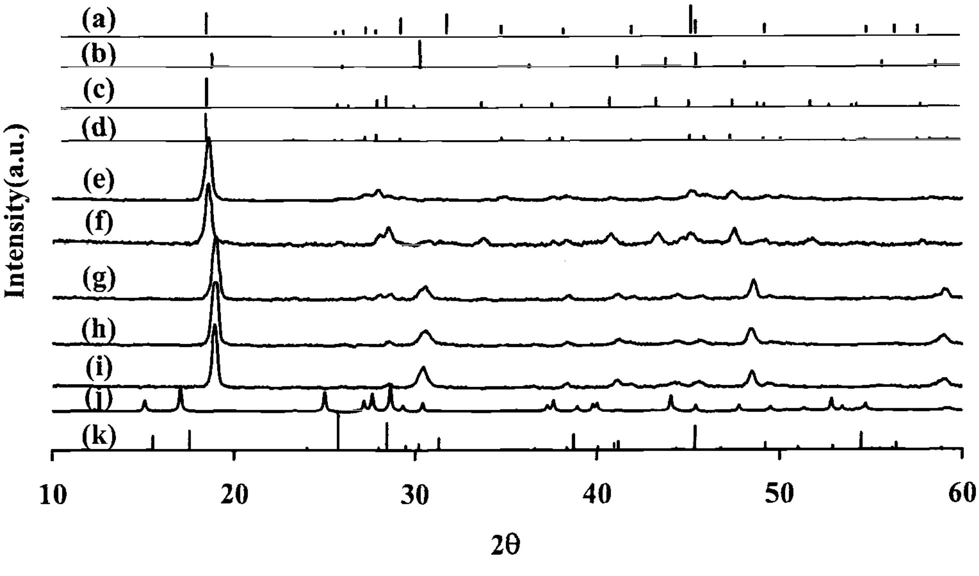

Figure 7.5. (a) β-In_2Se_3 JCPDS 40-1408 (Hex), (b) β-In_2Se_3 JCPDS 45-1041 (Rhomb), (c) γ-In_2Se_3 JCPDS 34-0455 (Rhomb), (d) γ-In_2Se_3 JCPDS 34-1279 (Hex), (e) experimental pattern of γ-In_2Se_3, (f) experimental pattern of $In_2Se_{2.9}$, (g) the powder pattern of In_2Se_3:0.25I, (h) the powder pattern of In_2Se_3:0.04Sb, (i) the powder pattern of In_2Se_3:0.04Bi, (j) α-In_2Se_3 ICSD 1376, (k) $InGaSe_3$ JCPDS 78-1745.

The n-type carriers have been observed in pressed pellets of Ga, Sb, Bi, or I-doped In_2Se_3. The resistance of Ga, Sb, and Bi-doped samples was approximately two orders of magnitude greater than that of the undoped material, while the I-doped pellet had a resistance equivalent to that of the undoped pellet. Because of the unique characteristics of I-doped sample, thin films were deposited onto glass substrates by using thermal evaporation. Following an anneal at 875 K, the film was found to crystallized predominately in the rhombohedral, β form (figure 7.6). The film exhibits a conductivity of 55 S/cm, a Hall mobility of 50 $cm^2/V{\cdot}s$, and a carrier concentration of 1.5×10^{19} cm^{-3}.

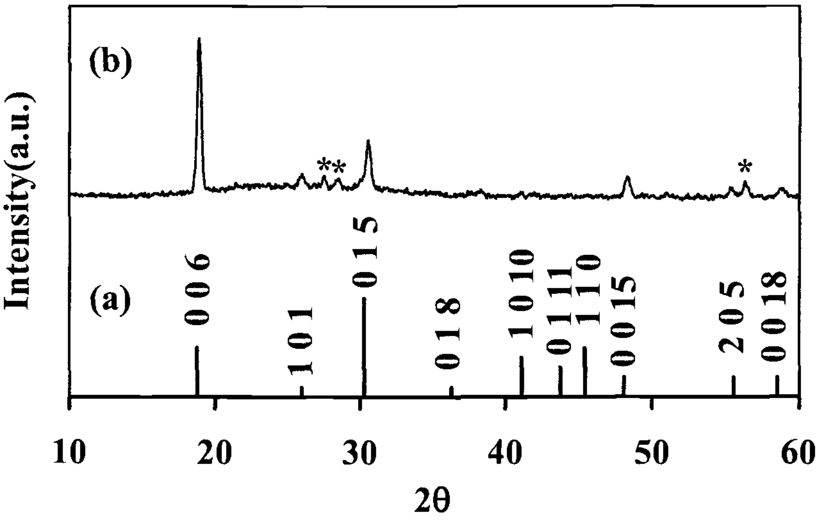

Figure 7.6. (a) Calculated (b) observed thin-film X-ray diffraction patterns of β-In_2Se_3 (R). * β-In_2Se_3 (H)

Our results on phase stabilization of In_2Se_3 are summarized in Scheme I. By adjusting temperature, stoichiometries, dopants, and heating times, different forms of In_2Se_3 can be stabilized. Unfortunately, except for the α phase, no good structural data are available for these phases. We attempted to refine structural parameters of these phases from single-crystal and powder data, but poor samples and data have prevented success. Osamura, Murakami, and Tomiie have published partial refinements ($R = 0.20$) of In_2Se_3 structure from powder data.[19] Unfortunately, these structures make no chemical sense in terms of bonded atoms, until one realizes that some of the In and Se atoms should be interchanged. As seen in Figure 7.7, the structures of the high-temperature phases likely share the common motif of "In_2Se_3" layers connected only by van der Waals interactions. Such layers are a common theme among the heavier main-group selenides and tellurides. It is likely that all of the high-temperature In_2Se_3 structure can be described as different poly types, i.e., stackings of the "In_2Se_3" planes; the specific stacking is controlled by temperature, stoichiometry, and doping.

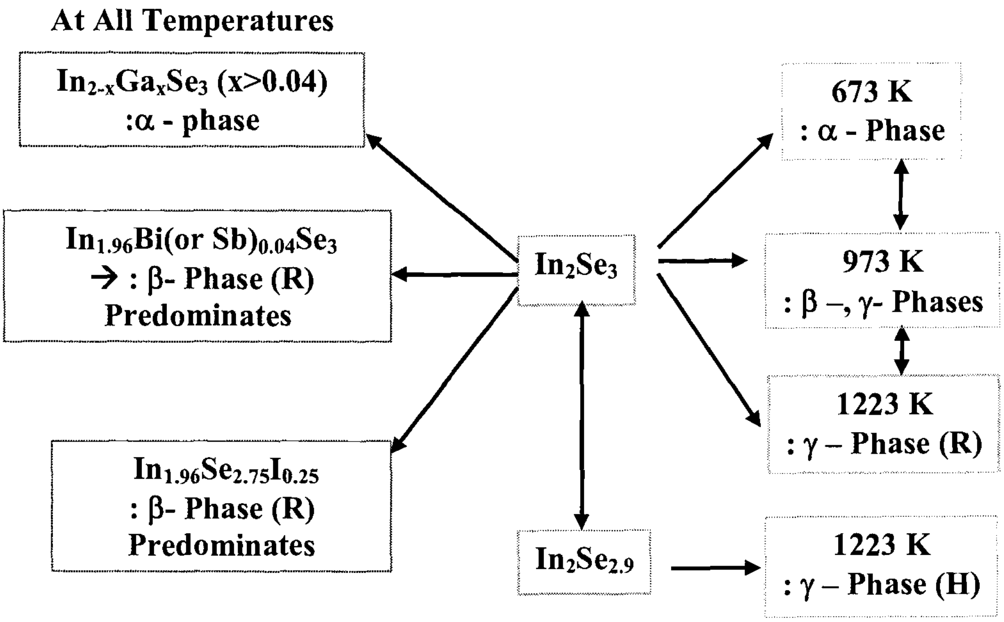

Scheme I. Summary of phase stabilization of In_2Se_3.

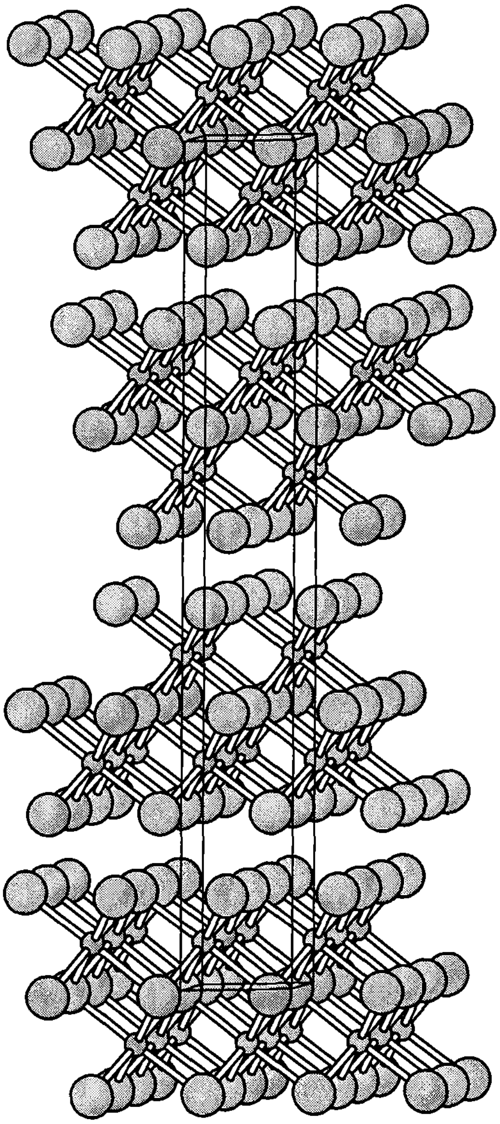

Figure 7.7. The structure of the high-temperature phase. Small and large circles represent In and Se atoms, respectively.

Considering the structure features of high-temperature In_2Se_3 phases, we were immediately drawn to the compound Sb_2Te_2Se. This material shares the same layered-type features (Figure 7.8), but it should easily be made p-type, because of the reservoir of electrons on the ion Sb^{3+}. Film were deposited by evaporation methods and annealed; resulting X-ray patterns are summarized in Figure 7.9. In contrast to the powder, the strong (0 0 *l*) peaks in the annealed film indicate a strong preferred orientation in the film.

All Sb_2Te_2Se films reveal *p*-type coductivity. Mobilities, carrier concentrations, and conductivities are summarized in Table 7.1. The highest values of mobility, carrier concentration, and conductivity of 190 $cm^2/V{\cdot}s$, 3.4 x $10^{19}/cm^3$, and 1000 S/cm, respectively, were obtained for a film annealed at 773 K. A photograph of an Sb_2Te_2Se film (~ 1μm-thick) on Si is shown in Figure 7.10.

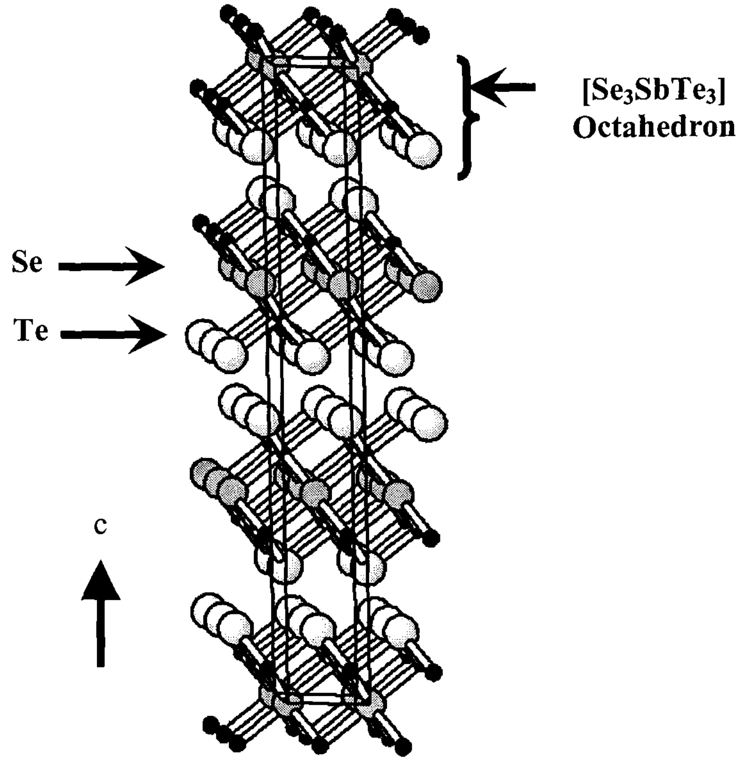

Figure 7.8. The structure of Sb_2Te_2Se. The small dark circles represent Sb atoms, the large dark circles represent Se atoms, and the large open circles represent Te atoms, and [Se_3SbTe_3] octahedrons were stacked along c axis.

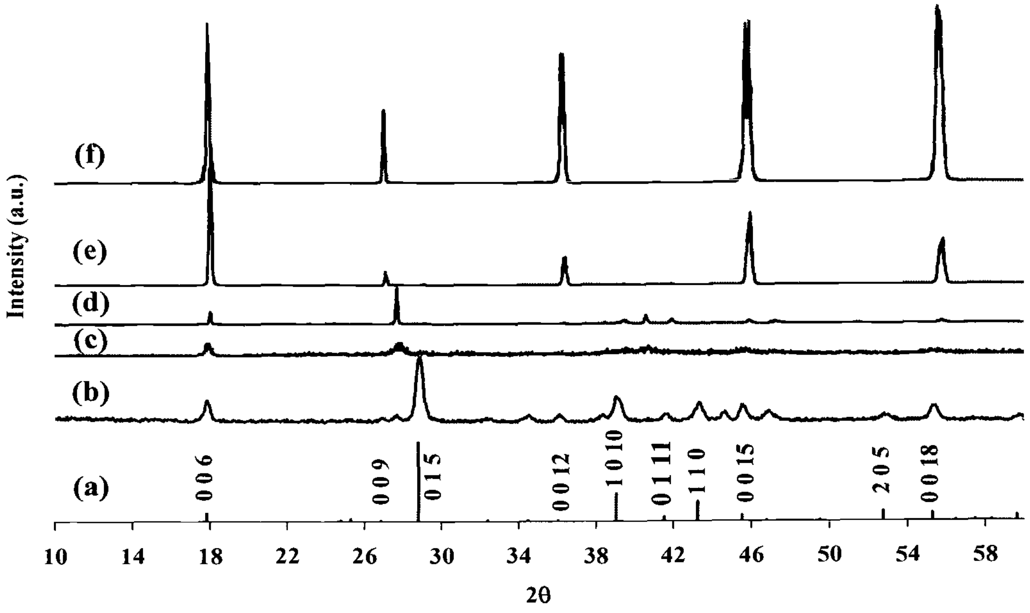

Figure 7.9. (a) Sb_2Te_2Se JCPDS 26-0659, (b) observed X-ray diffraction pattern of powder Sb_2Te_2Se, (c) as-deposited film, and film annealed at (d) 573 K, (e) 673 K, and (f) 773 K.

Table 7.1. Mobility, carrier concentration, conductivity values for Sb_2Te_2Se thin films.

XRD In Fig. 7.9	**Anneal Temp.(K)**	***p*/*n* -type**	**Mobility (cm^2/V·s)**	**Carrier Concentration (cm^{-3})**	**Conductivity (S/cm)**
(c)	**No**	***p***	**22**	**1.6×10^{19}**	**56**
(d)	**573**	***p***	**90**	**1.4×10^{19}**	**200**
(e)	**673**	***p***	**250**	**2.2×10^{19}**	**870**
(f)	**773**	***p***	**190**	**3.4×10^{19}**	**1000**

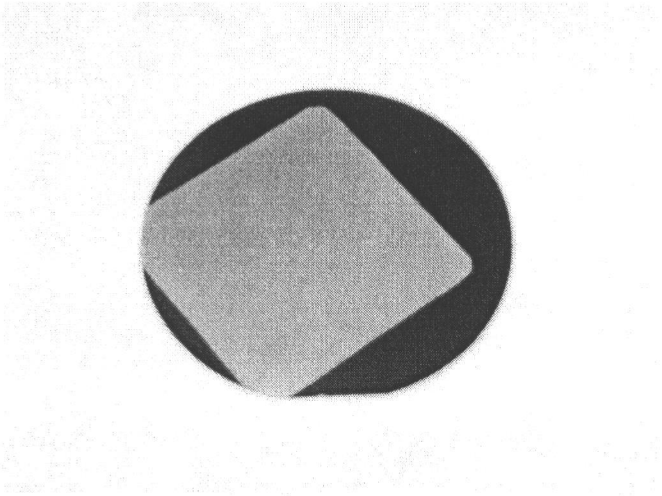

Figure 7.10.Photograph of Sb_2Te_2Se film on Si substrate.

REFERENCES

1. H. Hahn and W. Klingler, Z. Anorg. Allegm, Chem., **260**, 97 (1949).
2. H. Hahn, Angew. Chem., **65**, 538 (1953).
3. H. Hahn and G. Frank, Naturwissenschaften, **44**, 533 (1957).
4. H. Miyazawa and S. Sugaike, J. Phys.. Soc. Jpn., **12**, 312 (1957).
5. P. C. Newman and W. Redhill, Z. Anorg. Chem., **299**, 158 (1959).
6. S. A. Semiletov, Sov. Phys. Crystallogr., **5**, 673 (1961).
7. S. A. Semiletov, Sov. Phys. Crystallogr., **6**, 158 (1961).
8. K. Osamura, Y. Murakami, and Y. Tomiie, J. Phys. Soc. Jpn., **21**, 1848 (1966).
9. S. Popovic, B. Celustka, and D. Bidjin, Phys. Status Solidi A, **6**, 301 (1971).
10. S. Popovic, A. Tonejc, B. Grzeta-Plenkovic, B. Celustka, and B. Trojko, J. Appl. Cryst., **12**, 416 (1979).
11. A. Likforman, D. Messain, M. Guittard, and J. Flahaut, C. R. Acad. Sci., 274, 378 (1972).
12. A. Likforman, D. Carre, and R. Hillel, Acta. Cryst. B, **34**, 1 (1978).
13. A. Likforman, P. Fourcroy, M. Guittard, J. Flahaut, R. Poirier, and N. Szydio, J. Solid State Chem., **33**, 91 (1980).
14. J. van Landuty, G. van Tendeloo, and S. Amelinckx, Phys. Status Solidi A, **26**, K99 (1975).
15. C. Monolikas, J. Solid State Chem., 33, 91 (1980).
16. J. Ye, S. Soeda, Y. Nakamura, and O. Nittono, Jpn. J. Appl. Phy., **37**, 4264 (1998).

17. H. D. Lutz, M. Fischer, H.-P. Baldus, and R. Blachnik, J. Less-Common Met., **143**, 83 (1988).

18. Guseinov, G. G, Amiraslanov I. R., Kuliev A. S., Mamedov K. S., Izv. Akad. Nauk SSSR, Neorg. Mater., **23**, 854 (1987).

19. K. Osamura, Y. Murakami, Y. Tomiie, J. Phys, Soc. Japan, **21**, 1848(1966).

CHAPTER 8

CATION ORDERING IN LANGASITE STRUCTURE TYPES

Sangmoon Park and Douglas A. Keszler

Modified version: *Solid State Sciences*, **4**, 799 (2002)

ABSTRACT

Cation ordering has been examined for Langasite derivatives in the solid-solution series $La_3Sn_{1-x}Ga_5Si_{1-x}O_{14}$ ($0 < x \leq 1$) and $La_3SnGa_{5-x}Al_xO_{14}$ ($0 < x \leq 2$.) Complete solid solutions exist over the indicated compositional ranges. From single crystal X-ray measurements, Sn has been found to occupy only the distorted octahedral site, producing the ordered phase $La_3SnGa_5O_{14}$, while Al exhibits a preference for one of the two available distorted tetrahedral sites.

INTRODUCTION

Langasite ($La_3Ga_5SiO_{14}$) is a relatively new commercial material for use in wireless-communication applications. It exhibits piezoelectric moduli three times greater than quartz with large electromechanical coupling coefficients and low signal losses in acoustic-wave devices (1,2). It has the generic formula $A_3BC_3\underline{D_2}O_{14}$ ($La_3GaGa_3\underline{GaSi}O_{14}$,) where the A site is coordinated by eight O atoms; the B site is coordinated by six O atoms in a distorted octahedral geometry; and the C and D sites are coordinated by four O atoms in distorted tetrahedral geometries; these details may be discerned in Figure 8.1. The La atom occupies the A site; the Ga atoms are distributed over the B, C, and D sites; and the Si atoms partially occupy only the D sites. As such, Langasite is a disordered material. It has been proposed that this disorder leads to higher acoustic looses and poorer mechanical properties than could be achieved in ordered phases (3). For this reason, Langasite derivatives presumably with ordered structures, e.g., A = alkaline earth and B = Nb, Ta, have been prepared and studied (3-5). In this work, we describe the crystallization and structural characterization of the ordered Langasite derivative $La_3SnGa_5O_{14}$. In addition, the preference of the Al atom for occupation of the small D site is examined for the series $La_3SnGa_{5-x}Al_xO_{14}$ ($0 \leq x \leq 2$).

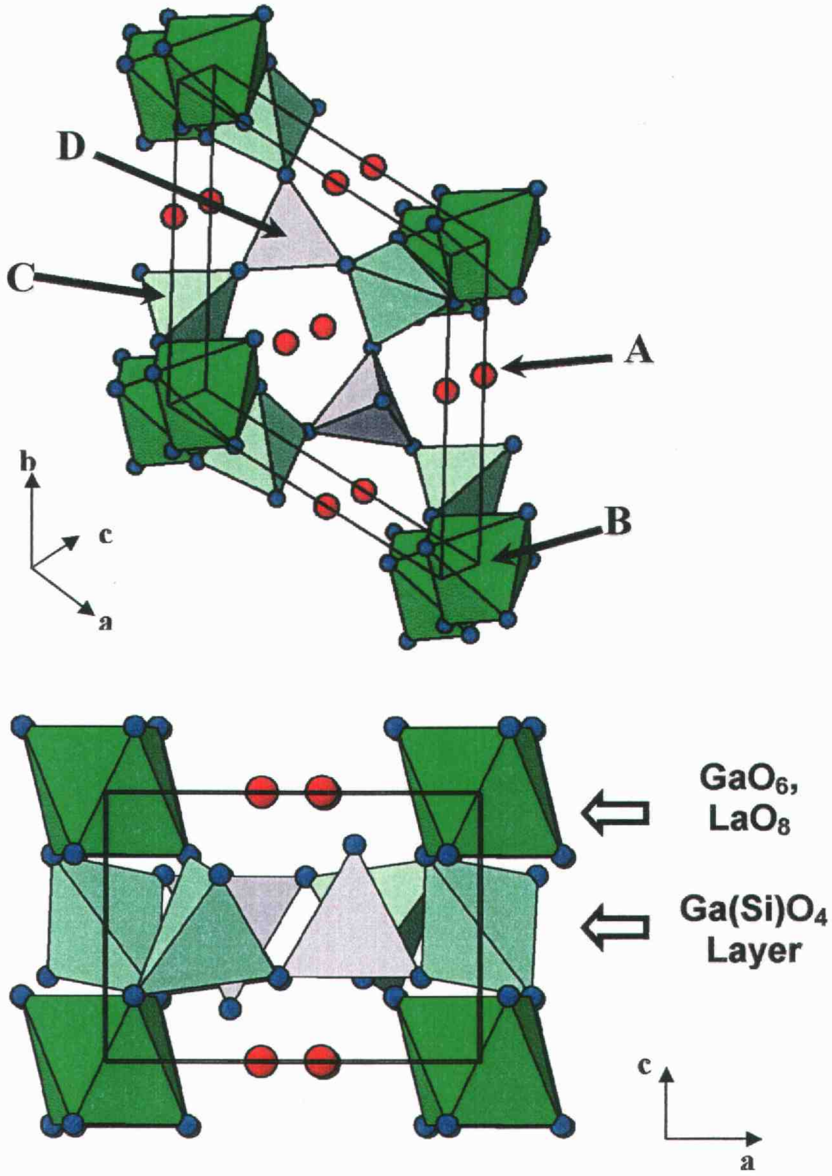

Figure 8.1. Structure of Langasite-type $A_3BC_3\underline{D}_2O_{14}$ ($La_3GaGa_3\underline{GaSi}O_{14}$).

EXPERIMENTAL

Synthesis

Powdered samples of $La_3Sn_{1-x}Ga_5Si_xO_{14}$ ($0 \leq x \lesssim 1$) and $La_3SnGa_{5-x}Al_xO_{14}$ ($0 \lesssim x \lesssim 2$) were prepared by heating stoichiometric mixtures of the reagents La_2O_3 (Cerac 99.99%,) SnO_2 (Cerac 99.9%,) SiO_2 (Alfa 99.995%,) Ga_2O_3 (Cerac 99.995%,) and Al_2O_3 (Alfa 99.997%) at 1623 K for 15 h and at 1698 K for 12 h, respectively. Crystals of $La_3SnGa_5O_{14}$ and $La_3SnGa_3Al_2O_{14}$ were grown in Pt crucibles by using a 5-wt% $LiBO_2$ flux. The melts were cooled from 1700 to 1473 K at 20 K/h for $La_3SnGa_5O_{14}$ and from 1748 to 1623 K at 10 K/h for $La_3SnGa_3Al_2O_{14}$; cooling to room temperature was programmed at 100 K/h.

Crystallographic studies

Clear, colorless crystals were mounted on glass fibers with epoxy and analyzed on a Rigaku AFC6R X-ray diffractometer equipped with monochromatic Mo Kα radiation (λ = 0.71069 Å.)

For $La_3SnGa_5O_{14}$, unit-cell parameters were obtained by automatic centering and least-squares refinement of 25 reflections in the range $34 < 2\theta < 36^o$. Intensity data covering the indices $0 < h < 10$, $-10 < k < 10$, $-6 < l < 6$ and the range $4 \leq 2\theta \leq 55^o$ were collected by using the ω-2θ scan technique and a scan speed of 16^o/min in ω. Three standard reflections measured after every block of 150 data exhibited no significant variations. A check of the Laue symmetry was consistent with group –3m1. The structure was refined by using computer programs from the *TEXSAN* crystallographic software package (6). The La, Sn, and Ga atoms were placed from the results available on the normal Langasite structure (7). The positions of the remaining O atoms were determined by examining subsequent difference electron density maps. Following refinement with isotropic displacement coefficients, the data were corrected for absorption with the program *DIFABS* (8) and averaged (R_{int} = 0.09). Refinement of the Sn occupation factor resulted in no statistically significant deviation from unity, so the parameter was fixed. Following refinement with anisotropic displacement coefficients on all atoms except O1 and O3, a difference electron density map revealed no peak greater than 0.9% of a La atom.

For $La_3SnGa_3Al_2O_{14}$, unit-cell parameters were obtained by automatic centering and least-squares refinement of 25 reflections in the range $26 < 2\theta < 40^o$. Intensity data covering the range of indices $0 < h < 10$, $-11 < k < 11$, $-7 < l < 7$ were collected by using the ω-2θ scan technique and a scan speed of 16^o/min in ω. Three standard reflections measured after every block of 150 data exhibited no significant variations. Initial atomic positions were taken from those of $La_3SnGa_5O_{14}$. An approximate Al stoichiometry was deduced by refining the occupancy factors for the Ga positions. These factors were then used in conjunction with constraints of Al occupation on the Ga sites to ensure unit occupation. Following refinement with isotropic displacement coefficients, the data were corrected for absorption with the program *DIFABS* and averaged (R_{int} =

0.097). Following complete refinement with anisotropic displacement coefficients on atoms Ln, Sn, and O2, a difference electron density map revealed no peak greater than 0.7% of a La atom. Crystallographic details and final atomic parameters for the two structures are given in Tables 8.1 and 8.2, respectively.

Table 8.1

Crystallographic data for $La_3SnGa_5O_{14}$ and $La_3SnGa_3Al_2O_{14}$

Formula	$La_3SnGa_5O_{14}$	$La_3SnGa_{3.10(6)}Al_{1.90(4)}O_{14}$
Space group	P321	P321
a (Å)	8.251(1)	8.210(1)
c (Å)	5.146(1)	5.106(1)
Volume (Å^3)	303.35(4)	298.04(5)
Z	1	1
Temperature (K)	296	296
D_{calc}(g cm^{-3})	6.065	5.697
Crystal dimensions (mm)	0.2 x 0.2 x 0.1	0.2 x 0.2 x 0.2
Aborption coefficient (cm^{-1})	232.8	194.2
Number of reflections collected	1668	1362
Number of unique data, ($F_o^2 > 3\sigma(F_o^2)$)	284	345
Number of variables	29	26
R(F), ($F_o^2 > 3\sigma(F_o^2)$)	0.037	0.037
wR	0.042	0.038

$R(F) = \sum \left| |F_o| - |F_c| \right| / \sum |F_o|$

$wR(F) = [\Sigma(|F_o| - |F_c|)^2 / \Sigma w |F_o|^2]^{1/2}$; $w = 1/\sigma^2(F_o)$

Table 8.2

Atomic positions and equivalent isotropic displacement parameters

$La_3SnGa_5O_{14}$

atom	site	x	y	z	B_{eq}[a]
La(1)	3e	0.57163(8)	0	0	0.72(1)
Sn(1)	1a	0	0	0	0.66(1)
Ga(1)	3f	0.2434(2)	0	1/2	0.86(2)
Ga(2)	2d	1/3	2/3	0.5313(3)	0.59(2)
O(1)	6g	0.4594(8)	0.1511(8)	0.304(1)	1.16(9)
O(2)	2d	2/3	1/3	0.815(2)	1.3(1)
O(3)	6g	0.8568(8)	0.0837(9)	0.7580(9)	0.83(8)

$La_3SnGa_3Al_2O_{14}$

atom	site	x	y	z	B_{eq}[a]
La(1)	3e	0.57145(7)	0	0	0.69(2)
Sn(1)	1a	0	0	0	0.66(2)
Ga(1)[b]	3f	0.2447(2)	0	1/2	0.66(4)
Ga(2)[c]	2d	1/3	2/3	0.5302(3)	0.77(4)
Al(1)[d]	3f	0.2447	0.0000	1/2	0.66
Al(2)[e]	2d	1/3	2/3	0.5302	0.77
O(1)	6g	0.4607(7)	0.1513(8)	0.3143(9)	1.23(7)
O(2)	2d	2/3	1/3	0.816(2)	1.3(1)
O(3)	6g	0.8569(7)	0.0851(7)	0.7574(7)	1.01(8)

[a] $B_{eq} = (8\pi^2/3)\Sigma_i\Sigma_j U_{ij}a_i{}^*a_j{}^*a_i\cdot a_j$ [b] occupancy = 0.69(1) [c] occupancy = 0.52(1)

[d] occupancy = 0.31 [e] occupancy = 0.48

RESULTS

Solution behavior and site occupancies in the series $La_3Sn_xGa_5Si_{1-x}O_{14}$ ($0 < x \leq 1$) were examined by diffraction methods. As shown by the unit-cell volume expansion with increasing Sn content (Figure 8.2,) the larger Sn atom (r = 0.83 Å) readily substitutes for Si^{4+} (r = 0.40 Å) at all compositions. Moreover, the change in the ratio of reflection intensities, I_{201}/I_{111}, with composition (Figure 8.2) is consistent with a selective occupation of the six-coordinate B site by Sn. This result was confirmed with the single-crystal X-ray measurements on $La_3SnGa_5O_{14}$.

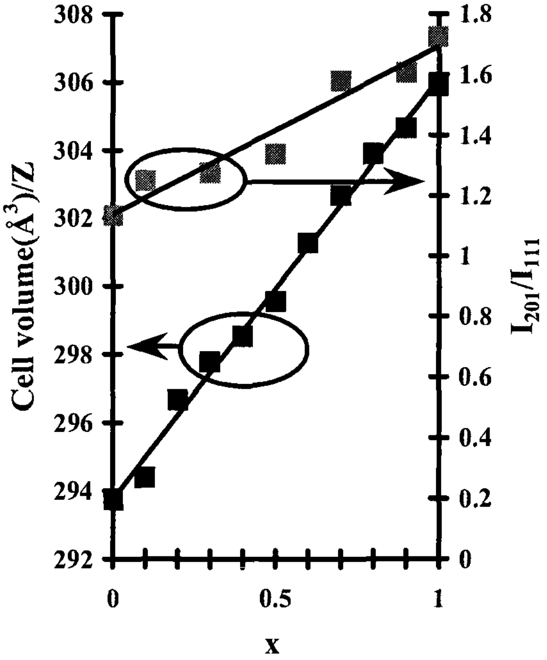

Figure 8.2. Unit-cell volume and intensity ratio I_{201}/I_{111} for solid solution $La_3Si_{1-x}Sn_xGa_5O_{14}$.

This compound adopts an ordered, normal Langasite structure (Figure 8.3) with La and Sn atoms located at z = 0 and Ga atoms at z ~ 0.5. The La-O distances and their distribution (Table 2) are similar to those reported for the parent Langasite structure of $La_3Ga_5SiO_{14}$ (7). The Sn-O distance, 2.059(8) Å, is consistent with the sum of crystal radii, 2.05 Å (9). and similar Sn-O interactions of 2.052, 2.058, and 2.041 Å reported for SnO_2 (10) and $Y_2Sn_2O_7$ (11). The Ga-O distances are also normal, comparing well to an expected value of 1.83 Å (9). Considering these interatomic distances and the results of occupancy refinements, it is clear that $La_3SnGa_5O_{14}$ crystallizes as an ordered compound.

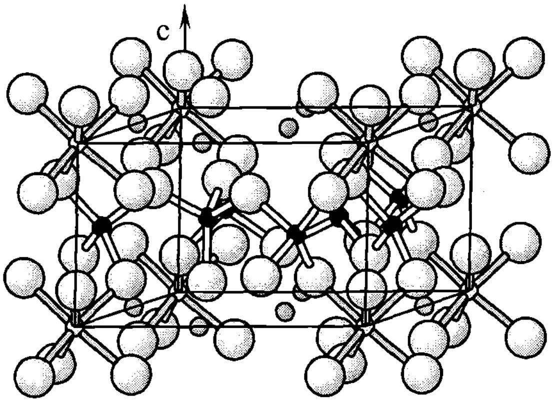

Figure 8.3. Unit-cell drawing of $La_3SnGa_5O_{14}$. La atoms are small shaded circles; Sn atoms small open circles; Ga atoms small dark circles; and O atoms large open circles.

From determination of unit-cell volumes in the series $La_3SnGa_{5-x}Al_xO_{14}$, the maximum substitution of Al for Ga occurs at x = 2 (Figure 8.4). Beyond this value, the unit-cell volume does not change, and diffraction lines attributable to $LaAlO_3$ and SnO_2 become evident in the diffraction patterns. Inspection of the intensity distribution in the patterns also indicated that the Al atom preferentially occupies the smaller, distorted tetrahedral D site over the distorted tetrahedral C site. This result has been verified by the single-crystal results for the composition $La_3SnGa_3Al_2O_{14}$. In this material, we find 50% occupancy of the small D site by Al atoms and 33% occupancy of the C site. The La-O and Sn-O distances are comparable to those of the Al-free compound (Table 2.3). As expected, contraction in the sizes of the C and D sites is evident from the trend of shorter Ga-O distances (Table 8.3) in the Al-substituted phase. These results can be compared with those for the solid-solution series $La_3Ga_{5-x}Al_xSiO_{14}$ (12), wherein the solubility limit of Al has been set at x = 1.5. This lower solubility of Al in comparison with that of the Sn derivative likely arises from the preferred occupation of the Si atom on the D site. From analysis of interatomic distances (12), substitution of Ga by Al was found to occur across each of the B, C, and D sites, i.e., in the absence of a large, highly charged ion, e.g., Sn^{4+}, some Al^{3+} will occupy the distorted octahedral B site. Interestingly, this Al substitution leads to small increases in the electromechanic coupling coefficients and the piezoelectric constant d_{11}, while depressing the coefficient d_{14} (12).

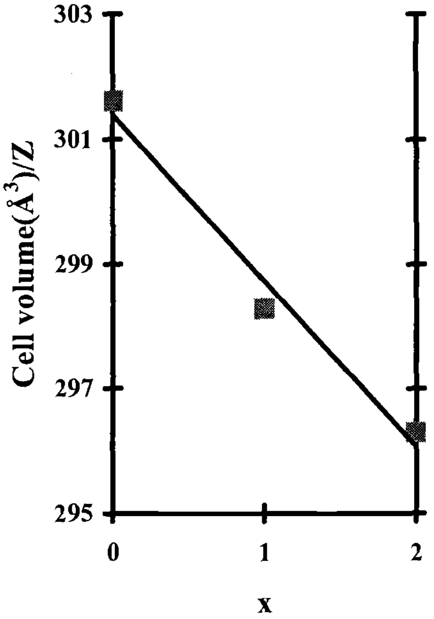

Figure 8.4. Unit-cell volume for solid solution $La_3SnGa_{5-x}Al_xO_{14}$.

Table 8.3.

Selected interatomic distances (Å) and angles (°) for $La_3SnGa_5O_{14}$ and $La_3SnGa_3Al_2O_{14}$

	$La_3SnGa_5O_{14}$	$La_3SnGa_3Al_2O_{14}$
La-O(1) x 2	2.45(1)	2.465(7)
La-O(1) x 2	2.886(9)	2.903(7)
La-O(2) x 2	2.631(5)	2.617(4)
La-O(3) x 2	2.437(8)	2.424(6)
Sn(1)-O3 x 6	2.059(8)	2.055(6)
Ga(1)-O(1) x 2	1.877(9)	1.839(6)
Ga(1)- O(3) x 2	1.827(8)	1.812(6)
Ga(2)-O(1) x 3	1.825(9)	1.788(7)
Ga(2)-O(2) x 1	1.78(1)	1.77(1)
O(1)-La(1)-O(1)	101.6(4)	103.2(3)
O(1)-La(1)-O(2)	91.5(3)	91.3(2)
O(1)-La(1)-O(3)	107.6(3)	106.7(2)
O(2)-La(1)-O(3)	126.3(2)	126.5(2)
O(3)-Sn(1)-O(3)	84.3(4)	84.3(3)
O(1)-Ga(1)-O(1)	103.8(6)	102.4(4)
O(1)-Ga(1)-O(3)	108.3(4)	107.2(3)
O(1)-Ga(2)-O(1)	100.2(3)	101.8(2)
O(1)-Ga(2)-O(2)	117.6(3)	116.4(2)

CONCLUSIONS

The Langasite derivative $La_3SnGa_5O_{14}$ has been synthesized and structurally characterized. Its facile crystallization from a borate flux may provide a means to develop a scalable growth method for incongruent Langasite derivatives. The structural results on this phase are consistent with an ordered arrangement of the cations. In the Al-containing derivatives, the Al atom exhibits a preference for occupation of the D site, although occupation extends to the C site as well.

SUPPLEMENTARY MATERIAL

Further details of the crystal structures may be obtained from the Fachinformationzentrum Karlsruhe, D-76344 Eggenstein-Leopoldshafen, Germany, FAX: (+49)7247-808-666, crysdata@fiz-karlsruhe.de. Depository numbers: CSD-412328 ($La_3SnGa_5O_{14}$) and CSD-412327 ($La_3SnGa_3Al_2O_{14}$)

ACKNOWLEDGMENT

This work was supported by the Solid-state Chemistry Program of the US National Science Foundation, Grant DMR-9617031.

REFERENCES

1. Shimamura K., Takeda H., Kohno T., Fikuda T., J. Crystal Growth 163 (1996) 388.

2. Bohm J., Heimann R. B., Hengst M., Roewer R., Schindler J., J. Crystal Growth 204 (1999) 128.

3. Chai B.H.T., Bustamante A.N.P., Chou M.C., Proc. 2000 IEEE/EIA Int. Freq. Control Symp. Exhib. (2000) 163.

4. Pisarevsky Yu V., Senyushenkov P. A., Mill B. V., Moiseeva, N. A., Proc. IEEE Freq. Control Symp. (1998) 742.

5. Sato J., Takeda H., Morikoshi H., Shimamura K., Rudolph P., Fukuda T., J. Crystal Growth 191 (1998) 746.

6. teXsan for Windows version 1.01. Single Crystal Structure Analysis Software. MSC, 3200 Research Forest Drive, The Woodlands, TX, 77381, USA.

7. Mill B. V., Butashin A. V., Khodzhabagyan, Belokoneva E. L., Belov N. V., Doklady Akad. SSSR 264 (1982) 1385.

8. Walker N., Stuart D. Acta Crystallogr., Sect. A 39 (1983) 158.

9. Shannon R. D., Prewitt C. T., Acta Crystallogr., Sect. B 25 (1969) 925.

10. Baur W. H., Khan A. A., Acta Crystallogr., Sect. B 27 (1971) 2133.

11. Brisse F., Knop O., Can. J. Chem. 46 (1968) 859.

12. Kumatoriya M., Sato H., Nakanishi J. Fujii T., Kadota M., Sakabe Y., J. Crystal Growth 229 (2001) 289.

CHAPTER 9

THE STRUCTURE AND LUMINESCENCE PROPERTIES OF YTTRIUM SILICATE CHLORDIE, $Y_3(SiO_4)_2Cl$

Sangmoon Park, Alexandre Yokochi, and Douglas A Keszler

Modified version submitted to Materials Research Bulletin

ABSTRACT

The silicate chloride $Y_3(SiO_4)_2Cl$ was prepared as both bulk powders and single crystals. It was structurally characterized by single crystal X-ray diffraction and found to crystallize in space group Pnma with cell parameters a = 6.839(7), b = 17.706(3), and c = 6.166(3) Å. The luminescence of Eu^{3+}-doped samples was also studied with excitation into the vacuum ultraviolet. The dominant emission transition is the $^5D_0 \rightarrow {}^7F_2$ at 618.5 nm, and the maximum brightness in the concentration-quenching study of $Y_{3-x}Eu_x(SiO_4)_2Cl$ was observed at x = 0.5.

INTRODUCTION

In 1978, Yamada and co-workers prepared a phosphor of composition $Y_3(SiO_4)_2Cl$:Ce (1) while studying the properties of Y_2SiO_5:Ce. The material was reported to be iso-structural to $Ln_3(SiO_4)_2Cl$ (Ln = Yb, Sm) (2, 3).

Since the previous study of $Y_3(SiO_4)_2Cl$ was rather limited, we decided to undertake the full structural characterization of the pure Y compound and to conduct luminescence studies of Eu-doped materials.

EXPERIMENTAL

Synthesis

The powder sample of $Y_3(SiO_4)_2Cl$ was prepared by heating a stoichiometric mixture of Y_2O_3 (Stanford 99.9%), SiO_2 (Aldrich 99.6%), and YOCl at 1273 K for 1d in an evacuated silica tube. (YOCl was obtained by heating a mixture of Y_2O_3 and excess NH_4Cl (Mallinkrodt, reagent grade) at 1223 K for 20 min in air.) To prevent reaction between Y_2O_3 and the silica tube at high temperature, the powdered mixture was placed in an alumina tube, which was then inserted into the silica tube prior to sealing. Single crystals of $Y_3Si_2O_8Cl$ were grown from such a mixture held at 1273 K for 4 weeks.

Crystallographic studies

A clear, colorless, plate-shaped crystal was mounted on a glass fiber with epoxy and analyzed on a Rigaku AFC6R X-ray diffractometer equipped with monochromatic Mo Kα radiation ($\lambda = 0.71073$ Å). Unit-cell parameters were obtained by automatic centering and least-squares refinement of 25 reflections in the range of $20 \leq \theta \leq 30^{\circ}$. Intensity data were collected for 1/8 of the sphere in the range of $2.30 \leq \theta \leq 30.05^{\circ}$ ($-1 \leq h \leq 9$, $-1 \leq k \leq 24$, $-1 \leq l \leq 8$) by using ω-2θ scans. The structure was solved by using direct methods as programmed in SHELXS-90 and refined by using SHELX-97. Crystallographic details, final atomic parameters, selected interatomic distances and angles, and anisotropic displacement parameters are given in Tables 9.1, 9.2, and 9.3 respectively.

Luminescence studies

Excitation provided by an Oriel 300-W Xe lamp was passed through a 50-cm water filter, focused onto the entrance slits of a Cary model-15 prism monochromator, and then onto the sample. Luminescence was collected at a near right angle to excitation light, dispersed through an Oriel 22500 1/8–m monochromator with interchangeable gratings. A Hamamatsu R636 photomultiplier tube was used for detecting emission. The signal was collected and amplified with a Keithley model 602 picoammeter and then converted to a digital signal for computer acquisition. The emission was corrected with a tungsten lamp. For the brightness measurements, all samples were excited with a low-pressure Hg lamp (254 nm). Emission was detected with the Hamamatsu photomultiplier tube.

Table 9.1.

Crystallographic data for $Y_3Si_2O_8Cl$

Formula	$Y_3Si_2O_8Cl$	
Formula weight	486.36	
Space group	P n m a (#62)	
Unit cell dimensions	a = 6.839(7) Å	α= 90°.
	b = 17.706(3) Å	β= 90°.
	c = 6.166(3) Å	γ = 90°.
Volume	746.6(9) $Å^3$	
Z	4	
Density (calculated)	4.327 Mg/m^3	
Crystal dimension	0.2 x 0.1 x 0.02 mm^3	
Absorption coefficient	23.819 mm^{-1}	
Reflections collected	1570	
Independent reflections	1116 [R(int) = 0.0543]	
Number of unique data	1116	
Number of variables	67	
R(F), $(F_o^2>2\sigma(F_o^2))$	0.0489	
wR2	0.1179	

$$R = \Sigma \mid |F_o| - |F_c| \mid / \Sigma |F_o|$$

$$wR2 = \{ \Sigma [w (F_o^2 - F_c^2)^2] / \Sigma [w(F_o^2)^2]\}^{1/2}$$

Table 9.2.

Atomic positions (x 10^4) and equivalent isotropic displacement parameters ($Å^2$x 10^3) for $Y_3Si_2O_8Cl$. U(eq) is defined as one third of the trace of the orthogonalized U^{ij} tensor.

atom	x	y	z	U(eq)
Y(1)	2062(1)	7500	1167(1)	10(1)
Y(2)	4854(1)	5907(1)	-1269(1)	9(1)
Si(1)	-230(3)	5996(1)	1215(3)	9(1)
Cl(1)	-423(4)	7500	-2629(4)	16(1)
O(1)	1667(7)	6189(3)	-322(6)	13(1)
O(2)	4871(7)	5300(3)	2110(7)	12(1)
O(3)	8025(7)	5954(2)	-534(7)	12(1)
O(4)	4652(6)	6750(2)	2240(7)	11(1)

Table 9.3. Selected interatomic distances (Å) and angles (°) for $Y_3Si_2O_8Cl$.

Y(1)-O(4) x 2	2.310(5)	O(1)-Y(1)-O(1)	135.17(19)
Y(1)-O(4) x 2	2.333(5)	O(1)-Y(1)-O(4)	135.94(16), 69.88(15),
Y(1)-O(1) x 2	2.511(4)		127.15(16), 63.38(15)
Y(1)-Cl	2.778(3)	O(4)-Y(1)-O(4)	70.2(2), 95.40(14),
Y(1)-Cl	2.892(3)		138.42(7), 69.4(2)
		O(1)-Y(1)-Cl(1)	77.26(11) x 2, 68.95(10) x 2
		O(4)-Y(1)-Cl(1)	75.54(13) x 2,140.17(11) x 2
			133.02(12) x 2, 85.72(13) x 2
		Cl(1)-Y(1)-Cl(1)	74.24(7)
Y(2)-O(2)	2.206(5)	O(1)-Y(2)-O(1)	129.72(16)
Y(2)-O(3)	2.217(6)	O(1)-Y(2)-O(2)	83.09(16), 110.46(16),
Y(2)-O(1)	2.311(5)		87.35(16), 147.08(16)
Y(2)-O(3)	2.336(5)	O(1)-Y(2)-O(3)	72.56(15), 149.62(15),
Y(2)-O(2)	2.343(5)		71.19(15), 63.08(18)
Y(2)-O(1)	2.491(4)	O(1)-Y(2)-O(4)	67.68(14), 127.26(14)
Y(2)-O(4)	2.633(5)	O(2)-Y(2)-O(2)	76.40(17)
Y(2)-Cl	2.908(1)	O(2)-Y(2)-O(3)	90.09(17), 83.25(16),
			80.27(15), 140.30(16)
		O(2)-Y(2)-O(4)	138.33(15), 61.95(15)
		O(3)-Y(2)-O(3)	133.99(15)
		O(3)-Y(2)-O(4)	82.06(15), 130.15(15)
		O(1)-Y(2)-Cl(1)	77.74(13), 68.91(12)
		O(2)-Y(2)-Cl(1)	152.86(13), 130.73(13)
		O(3)-Y(2)-Cl(1)	94.25(12), 74.50(12)
		O(4)-Y(2)-Cl(1)	68.79(10)
Si(1)-O(2)	1.610(1)	O(2)-Si(1)-O(3)	115.3(3)
Si(1)-O(3)	1.610(5)	O(2)-Si(1)-O(4)	104.6(3)
Si(1)-O(4)	1.642(4)	O(3)-Si(1)-O(4)	112.9(2)
Si(1)-O(1)	1.643(5)	O(2)-Si(1)-O(1)	119.7(3)
		O(3)-Si(1)-O(1)	102.0(3)
		O(4)-Si(1)-O(1)	101.8(2)

RESULTS

The contents of a unit cell of the title compound are diagrammed in Figure 9.1. The structure is represented by a condensation of YO_6Cl_2, YO_7Cl, and SiO_4 polyhedra. A drawing of the two Y sites is given in Figure 9.2. The Y1 site can be described as a distorted cubic antiprism, while the Y2 is best described as a strongly distorted cubic octahedron. Average distances, Y1-O = 2.38(9) and Y2-O = 2.36(14) Å, are comparable to a Y-O distance of 2.39 Å for a Y atom in an environment of 8 O atoms (4). The two Y1-Cl distances, 2.778(3) and 2.892(3) Å, bracket the value, 2.83 Å, for an 8-coordinate Y site (5), while the Y2-Cl distance, 2.908(1) Å, is slightly longer. Si-O distances and O-Si-O angles are normal.

This structure may be compared to that of Y_2SiO_5, which crystallizes in space group C2/c (6). Writing the formula as $Y_2(SiO_4)O$ leads to the description of the material as a silicate oxide as compared with the silicate chloride of the title compound. Like $Y_3(SiO_4)_2Cl$, the compound $Y_2(SiO_4)O$ contains two crystallographically nonequivalent Y sites, but the coordination numbers are smaller – 6 and 7.

The emission spectrum of $Y_{2.95}Eu_{0.05}(SiO_4)_2Cl$ is given in Figure 9.3. Because the Y sites are noncentrosymmetric, the transition $^5D_0 \rightarrow {}^7F_2$ is expected to dominate the emission, and this line occurs at 618.5 nm. The vacuum ultraviolet-excitation spectrum for $Y_{2.4}Eu_{0.6}(SiO_4)_2Cl$ is given in Figure 9.4. The broad band feature extending from approximately 200 to 260 nm is associated with overlapping

O → Eu and Cl → Eu charge transfer transition, while the band centered near 170 nm is largely associated with absorption by the silicate group (7). Without a more detailed analysis, it is not possible to comment on the distribution of the Eu atoms over the two Y sites. The chromaticity coordinates x = 0.65, y = 0.35 are comparable to the values of x = 0.66, y = 0.34 for $Y_2SiO_5:Eu^{3+}$ and x = 0.65, y = 0.34 for the standard red phosphor $Y_2O_3:Eu^{3+}$ (8). The concentration-quenching curve for $Y_{3-x}Eu_xSi_2O_8Cl$ is given in Figure 9.5; the maximum emission occurs at x = 0.5.

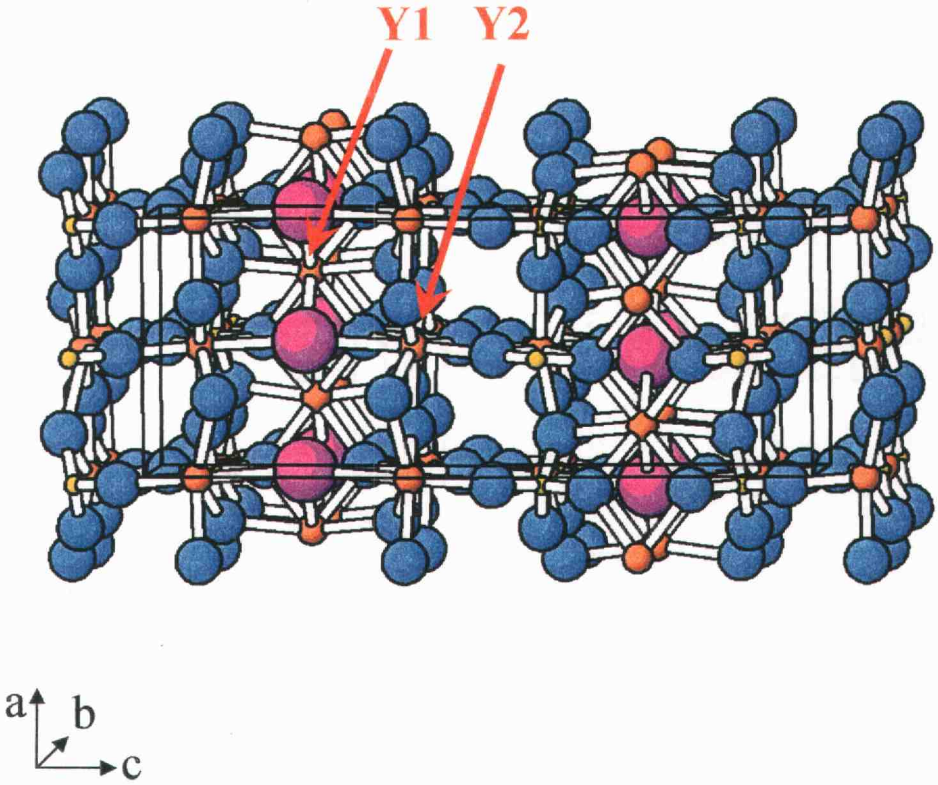

Figure 9.1. Unit-cell drawing of $Y_3(SiO_8)_2Cl$. Y atoms are large shaded circles; Si atoms are small shaded circles; O atoms are small open circles; and Cl atoms are large open circles.

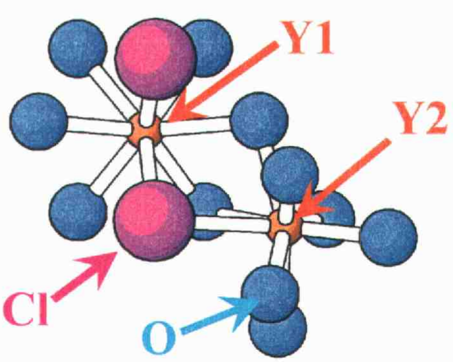

Figure 9.2. Y1- and Y2-centered polyhedra in $Y_3(SiO_4)_2Cl$.

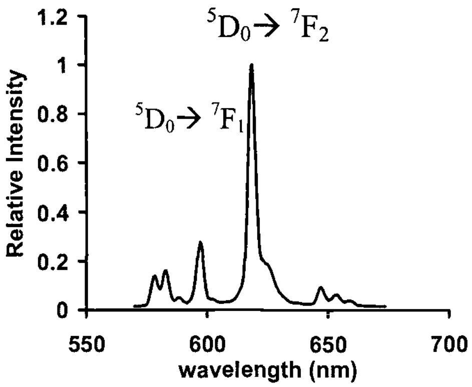

Figure 9.3. Emission spectrum of $Y_{2.95}Eu_{0.05}(SiO_4)_2Cl$ (λ_{exc} = 280 nm).

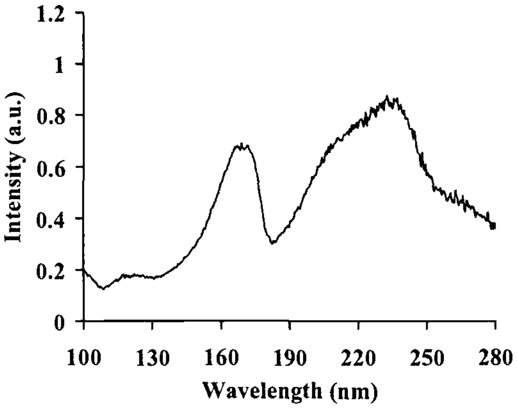

Figure 9.4. Vacuum ultraviolet excitation spectrum of $Y_{2.4}Eu_{0.6}(SiO_4)_2Cl$.

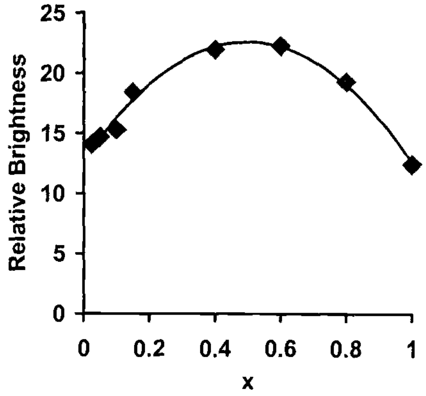

Figure 9.5. Concentration quenching curve for $Y_{3-x}Eu_x(SiO_4)_2Cl$ ($0 \leq x \leq 1$).

SUMMARY

Yttrium silicate chloride, $Y_3(SiO_4)_2Cl$, has been synthesized in both powder and single-crystal forms. It adopts an orthorhombic structure that is the same as$Yb_3(SiO_4)_2Cl$. The luminescence was examined by emission spectroscopy and concentration quenching, revealing a saturated red emission with a maximum brightness at the stoichiometry $Y_{2.5}Eu_{0.5}(SiO_4)_2Cl$.

ACKNOWLEDGMENT. This work was supported by the US National Science Foundation.

REFERENCES

1. H. Yamada, T Kano and M Tanabe, *Mat. Res. Bul.* 13 101-108 (1978).

2. C. Ayasse and H. A. Eick, *Inorg. Chem.*, 12(5) 1140-1143 (1973).

2. L. S. Chi, L. F. Zhou, H. Y. Chen, H. H. Zhang, and J. S. Huang, *Jiegon Huaxue*, 16(3) 219-222 (1997).

4. Dong Li, *Ph.D. Thesis*, Oregon State University, (1999).

5. R. D. Shannon and C. T. Prewitt, *Acta Crystallogr., Sect. B*, 25 925 (1969).

6. R. D. Shannon, *Acta Crystallogr., Sect. A*, 32 751 (1976).

7. A.Mayolet, J.C. Krupa, I. Gerard, and P. Martin, *Mater. Chem. Phys.*, 31, 107-109 (1992).

8. S. Shionoya and W. M. Yen, *Phosphor Handbook*, CRC Press.

CHAPTER 10

SYNTHESIS AND LUMINESCENCE PROPERTIES OF Mn:Zn_2SiO_4 AND Eu:Y_6WO_{12}

Sangmoon Park and Douglas A Keszler

ABSTRACT

$Zn_{1.95}Mn_{0.05}SiO_4$ was synthesized by hydrothermal dehydration of precipitates between Zn^{2+} and SiO_4^{4-} ions at 473 K and heating with $MnCO_3$ at 1473 K in air. The emission spectrum was observed at 530.0 nm with x = 0.261 and y = 0.696 chromaticity coordination. The concentration quenching curve of $Zn_{2-x}Mn_xSiO_4$ ($0.02 \leq x \leq 0.2$) was obtained under 254 nm excitation showing 68 % brightness (x = 0.05) compared to commercial $Mn:Zn_2SiO_4$ phosphor. Scanning electron micrograph (SEM) images of $Zn_{1.95}Mn_{0.05}SiO_4$ and commercial $Mn:Zn_2SiO_4$ phosphor were taken. Y_6WO_{12} was synthesized by solid-state reaction using a 2-wt% Li_2WO_4 flux at 1323 K for 3 h. The excitation and emission spectra of $Y_{5.95}Eu_{0.05}WO_{12}$were observed. The concentration quenching of $Y_{6-x}Eu_xWO_{12}$ ($0.1 \leq x \leq 1.5$) was obtained.

INTRODUCTION

$Mn:Zn_2SiO_4$ is widely being studied as green phosphors in CRT and plasma display panel (PDP) for TV applications.[1,2] Zn_2SiO_4, willemite, has trigonal structure with two different sites of Zn atoms in tetrahedral geometry. The distance of nearest Zn ions is 3.112 Å.[3] The structure of Y_6WO_{12} is known as a fluorite-related structure. Single yttrium and tungsten atom sites exist in this structure. Y and W atoms are coordinated by 7 and 6 oxygen atoms, respectively. Coordination numbers of Y and W sharing one oxygen atom are reduced from 8 to 7 and 6 by oxygen vacancies.[4] The melting point of Y_6WO_{12} was known as at 2073 K. The high temperature solid-state reaction[4-6] and chemical solution process[7] were known as the synthesis methods of Y_6WO_{12}. In previous work[8], hydrothermal dehydration of precipitation of Zn_2SiO_4 was performed. Continuously the luminescent properties of $Mn:Zn_2SiO_4$ was studied and compared to standard $Mn:Zn_2SiO_4$ phosphor in this work. In this work, A 2-wt% Li_2WO_4 was used as a flux to synthesis Y_6WO_{12} at relatively lower temperature as well as Eu^{3+}-activated Y_6WO_{12} was studied.

EXPERIMENTAL

$Zn_{1.95}Mn_{0.05}SiO_4$

Each of 1.9450 g of $ZnSO_4{\cdot}H_2O$ (Aldrich, 99.9%) and 1.0230 g of Na_4SiO_4 (Alfa-Aesar, reagent grade) was dissolved in 20ml H_2O. A precipitation reaction occurred in between Zn^{2+} (aq) and SiO_4^{4-} (aq) solutions. The resulting insoluble solid was stirred and heated approximately at 338K on the hot plate for 30 min. After filtration the wet precipitate was placed in a Teflon-lined high-pressure reaction vessel at 473 K for 12 h. The dehydrated powder was obtained with clear water in the Teflon container and immediately ground with 0.0319 g of $MnCO_3$ (Alfa-Aesar, 99.985%) and the mixture was dried in the warm oven. The dried mixture was pre-heated at 923 K for 1h and then finally cooked at 1473 K for 15h.

Y_6WO_{12}

Powdered samples of Y_6WO_{12} was prepared by heating stoichiometric mixtures of the reagents Y_2O_3 (Stanford, 99.9%) and WO_3 (Cerac 99.99%,) at 1323 K for 3 h using a 2-wt% Li_2WO_4 flux.

RESULTS

For Mn:Zn_2SiO_4, Zn^{2+} (or Mn^{2+}) is coordinated by four oxygen atoms in tetrahedral geometry. As the result of the weak crystal field of the tetrahedrally coordinated Mn^{2+} site the broad green emission was observed at 530.0 nm with $^4T_1 \rightarrow {}^6A_1$ transition in the spectrum of $Zn_{1.95}Mn_{0.05}SiO_4$ in Figure 10.1. To prevent decreasing of luminescence efficiency due to defection Mn:Zn_2SiO_4 was slightly ground and selected the certain particle size (less than 180 μm (0.007inches)) using the Standard Testing Sieve (*gilson* company.INC). The brightness of the $Zn_{2-x}Mn_xSiO_4$ ($0.02 \leq x \leq 0.2$) compounds has been determined relative to a commercial of Mn:Zn_2SiO_4 phosphor. $Zn_{1.95}Mn_{0.05}SiO_4$ was shown 68 % as bright as the commercial material under 254 nm excitation. The chromaticity coordinates of x = 0.261 and y = 0.696 were obtained.

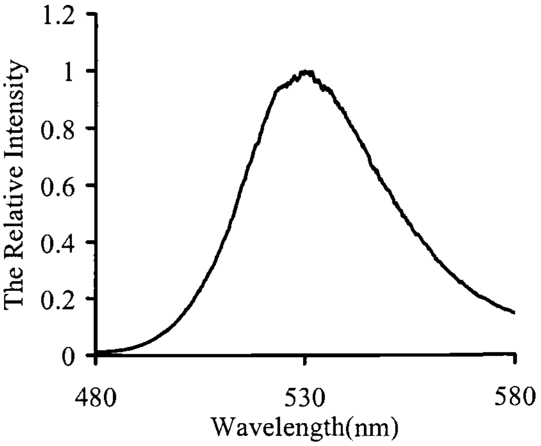

Figure 10.1. The emission spectrum of $Zn_{1.95}Mn_{0.05}SiO_4$.

The concentration dependence of the Mn^{2+} emission intensities under 254 nm excitation was shown in Figure 10.2. The concentration quenching occurs at around 2~3 % Mn^{2+} concentrations (x = 0.04 ~ 0.06) showing efficient energy transfer. After 3% Mn^{2+} concentration, the relative intensity was rapidly decreased due to increase non-radiative centers.

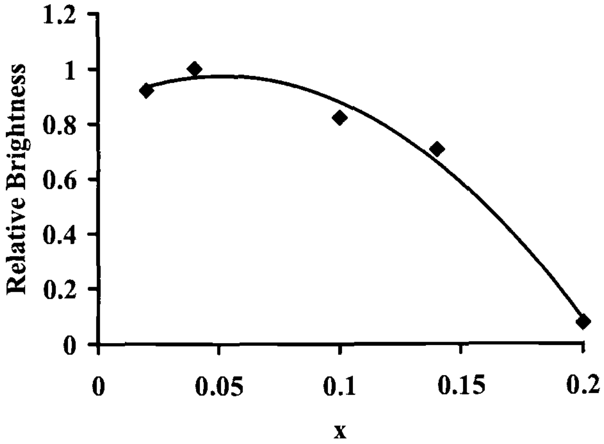

Figure 10.2. The concentration quenching of $Zn_{2-x}Mn_xSiO_4$.

The Figure 10.3 shows the scanning electron microscopic (SEM) images of $Zn_{1.95}Mn_{0.05}SiO_4$ (a), (c) and commercial $Mn:Zn_2SiO_4$ (b), (d). The commercial $Mn:Zn_2SiO_4$ phosphor was obtained from OSRAM SYLANIA chemical/ metals.INC (Type : 2282, Lot : SX750SI). The similarity is shown in particle shape between two samples in Figure 3 (a) and (b). Particles prepared by the precipitation and heating method were observed in the homogenous size distribution around 1μm x 2 μm in Figure 3 (a). The commercial phosphors consists of fine powder in Figure 3 (d). Figure 3 (c), 10 μm scale SEM image, shows the chunk of Mn-doped zinc silicate because particles less than 180 μm size were selected by the sieve.

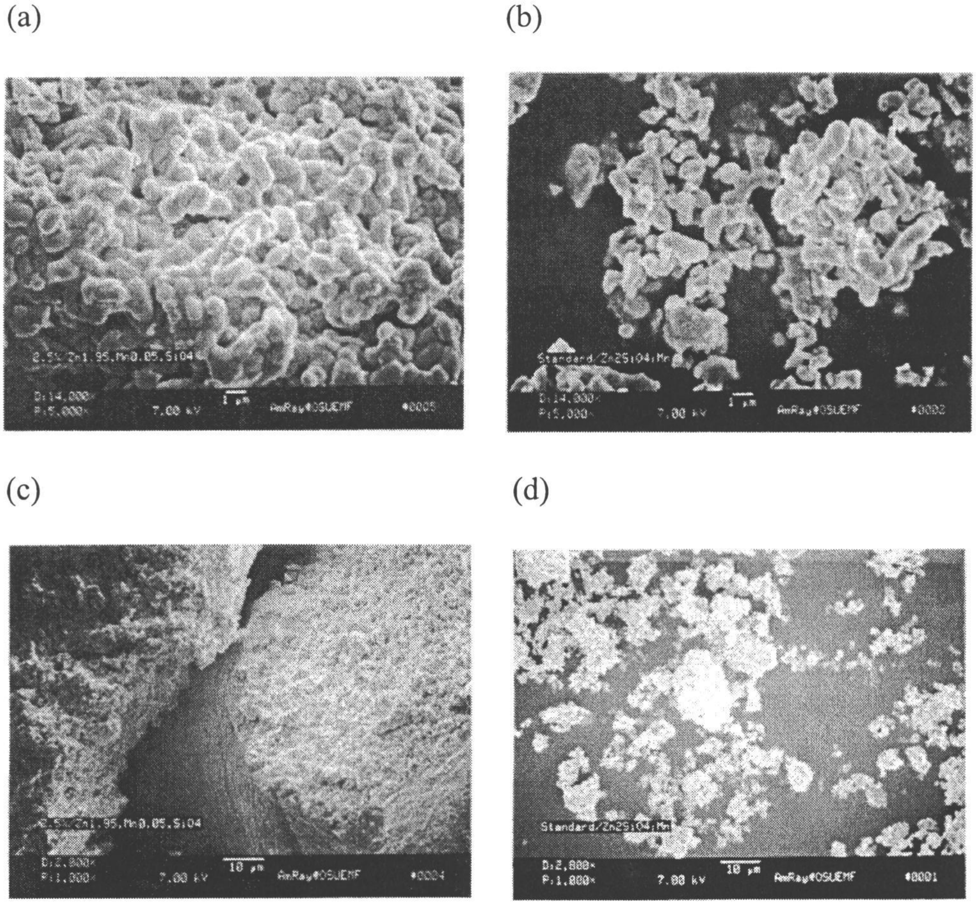

Figure 10.3. Scanning electron micrograph (SEM) images of $Zn_{1.95}Mn_{0.05}SiO_4$ (a), (c) and commercial Zn_2SiO_4:Mn phosphor (b), (d).

The structural study of Eu-doped $3Y_2O_3{\cdot}WO_3$ with was carried out by Beaury and co-workers.[4] It was heated for 24 h at 2023 K by solid state reaction. In this work, $3Y_2O_3{\cdot}WO_3$ single phase was produced at 1323 K for 3h using a 2-wt% Li_2WO_4 flux. The excitation and emission spectra of $Y_{5.95}Eu_{0.05}WO_{12}$ were shown in Figure 10.4. The excitation spectrum shows the broad charge transfer band and f-f transition bands. For Eu:Y_2O_3, the charge transfer band was obtained at 254 nm.[9] On the other hand, the charge transfer band of $3Y_2O_3{\cdot}WO_3{:}0.05Eu^{3+}$ ($Y_{5.95}Eu_{0.05}WO_{12}$) was observed around 311 nm shown in Figure 10.4. Y atoms are coordinated by 6 and 7 oxygen atoms in Y_2O_3 and Y_6WO_{12}, respectively. The electronic transition shift lower energy for increasing covalency. The distances of Y-O are 2.24 (~ 2.31) and 2.650 Å in Y_2O_3 and Y_6WO_{12}, repectively.[4,10] Y atom is coordinated by seven O atoms in a largely distorted geometry. As the result of the lack of the center symmetry for Eu^{3+} site the most intense emission was observed at 604.9 nm with $^5Do \rightarrow {}^7F_2$ transition in the spectrum of $Y_{5.95}Eu_{0.05}WO_{12}$ in Figure 10.4.[11]

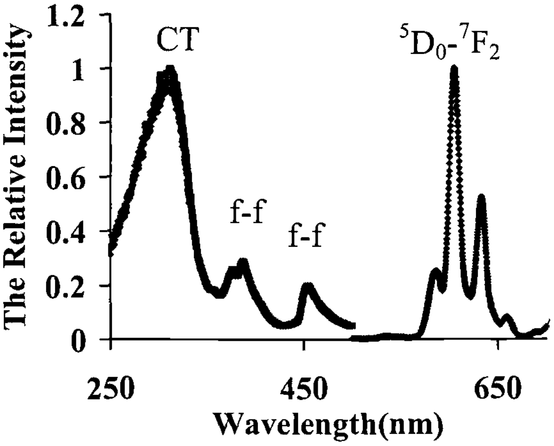

Figure 10.4. The excitation and emission spectra of $Y_{5.95}Eu_{0.05}WO_{12}$.

The concentration quenching curve of solid solution $Y_{6-x}Eu_xWO_{12}$ ($0.1 \leq x \leq 1.5$) was shown in Figure 10.5. The concentration quenching occurs around x = 0.5 in $Y_{6-x}Eu_xWO_{12}$ with low efficient energy transfer. After x = 0.5 concentration the relative intensities were decreased due to increasing non-radiative centers.

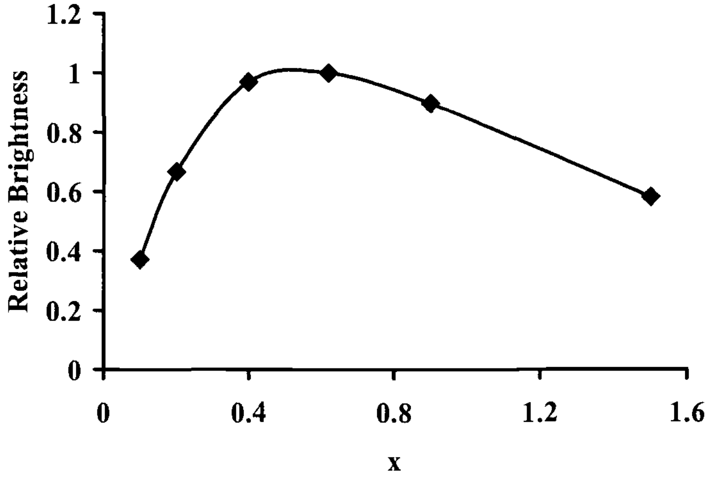

Figure 10.5. Concentration quenching curve of $Y_{6-x}Eu_xWO_{12}$ ($0.1 \leq x \leq 1.5$).

CONCLUSIONS

The hydrothermal dehydration of precipitates and heating method produced relatively good bright luminescence of $Zn_{1.95}Mn_{0.05}SiO_4$ with homogenous particle shape compound in comparison to commercial $Mn:Zn_2SiO_4$ phosphor. The single phase of Y_6WO_{12} was synthesized at 1323 K. The excitation and emission spectra and concentration quenching were performed in $Eu:Y_6WO_{12}$.

REFERENCES

1. X. W. Sun and H. S. Kwok, Appl. Phys A, 69(Suppl.), S39-S43 (1999).
2. A Morell and N. El Khiati, J. Electrochem. Soc., 140(7), 2019-2022 (1993).
3. K. H. Klaska, J. C. Eck, and D. Pohl, Acta Cryst., 1978, B34, 3324-3325.
4. O Beaury, M Faucher, and P Caro, Mat. Res. Bul. 1978, 13, 175-185.
5. H.J. Borchardt, Inorg. Chem., 1963, 2(1), 170-173.
6. K. Kuribayashi, M Yoshimura, T. Ohta, and T. Sata, J. Am. Cerm. Soc. 1980, 61(11-12), 644-646.
7. M. Yoshiro, J. Ma, and M. Kakihana, J. Am. Ceram. Soc., 1998, 81(10), 2721-2724.
8. B. L. Clark and D. A. Keszler, Inorg. Chem. 2001, 40, 1724-1725.
9. L. Ozawa, H. Forest, P. M. Jaffe, and G. Ban, J. Electrochem. Soc. 1971, 118(3), 482-486.
10. H. Ishibashi, K. Shimomoto, and K. Nakahigashi, J. Phys. Chem. Solids, 1994, 55(9), 809-814.
11. Blasse G., Grabmaier B. C., Luminescent Materials, Springer-Verlag, 1994.

CHAPTER 11

CONCLUSIONS AND FUTURE WORK

Crystalline thin films of Zn_2SiO_4, ZrO_2, and MnO_2 were obtained at low temperatures by using SILAR deposition method in conjunction with hydrothermal annealing. This method represents a new, quite general procedure for preparation of crystalline oxide films. Following methods described in this work, film porosity is expected to be significant because of the loss of water in the final dehydration step. Future work should be directed to incorporation of a dehydration step in the cycle of dipping and rinsing to determine if dense, crystalline films can be realized. The work could also be extended to the generation of multilayer and patterned films. The underlying deposition and growth mechanisms could also be monitored by using techniques such as X-ray diffraction and atomic force microscopy. In developing p-type transparent conductors, single phase delafossite oxides, $CuMO_{2+\delta}$ (M = Ga, Sc, In), were synthesized by substitution and flux-assisted methods. Transparent p-type conducting $BaCu_2S_2$ films were deposited on glass and KBr substrate, yielding a conductivity of 17 S/cm, Hall mobility of 3.5 $cm^2/V{\cdot}s$, and an optical transparency approaching 90% in the visible. This work was extended by cursory study of the material BaCuSF. Continued work on the family BaCuQF (Q = S, Se, Te) should provide considerable insight into the potential for generation p-type transparent conductors on the basis of Cu chalcogenides.

Structural and conducting properties of the various polymorphs of In_2Se_3 and the related structure of Sb_2Te_2Se were considered.

Cation ordering has been examined for Langasite derivatives in the solid-solution series $La_3Sn_{1-x}Ga_5Si_{1-x}O_{14}$ $(0 < x \leq 1)$ and $La_3SnGa_{5-x}Al_xO_{14}$ $(0 < x \leq 2.)$ From the single crystal X-ray measurement, the structures of $La_3SnGa_5O_{14}$ and $La_3SnGa_3Al_2O_{14}$ have been refined. It is hoped that these results will prompt others to examine the physical properties of these piezoelectric materials.

$Y_3(SiO_4)_2Cl$ was structurally characterized by single crystal X-ray diffraction and the luminescent property of Eu^{3+}-doped samples was studied.

BIBLIOGRAPHY

Alt M., Lewerenz H. J., and Scheer R., *J Appl. Phys.*, **81(2)**, 956-959 (1997).

Ayasse C. and Eick H. A., *Inorg. Chem.*, 12(5) 1140-1143 (1973).

Baur W. H., *Acta Crystallogr., Sect. B* **32**, 2200 (1976).

Baur W. H., Khan A. A., Acta Crystallogr., Sect. B 27 (1971) 2133.

Beaury O, Faucher M, and Caro P, Mat. Res. Bul. 1978, 13, 175-185.

Benko F. A., and Koffyberg F. P., *J. Phys. Chem. Solids*, **45(1)**, 57-59 (1984); Benko F. A., and Koffyberg F. P., *Can. J. Phys.*, **63**, 1306-1308 (1985); Benko F. A., and Koffyberg F. P., *Phys. Stat. Sol.*, **94**, 231-234 (1986); Benko F. A., and Koffyberg F. P., *Mat. Res. Bull.*, **21**, 753-757 (1986); Benko F. A., and Koffyberg F. P., *J. Phys. Chem. Solids*, **48(5)**, 431-434 (1987).

Blasse G., Grabmaier B. C., Luminescent Materials, Springer-Verlag, 1994.

Bohm J., Heimann R. B., Hengst M., Roewer R., Schindler J., J. Crystal Growth 204 (1999) 128.

Borchardt H.J., Inorg. Chem., 1963, 2(1), 170-173.

Brisse F., Knop O., Can. J. Chem. 46 (1968) 859.

Cava R. J., Zandbergen H. W., Ramirez A. P., Takagi H., Chen C. T., Krajewski J. J., Peck W. F., Waszczak J. V., Meigs G., Roth R. S., and Schneemeyer L. F., *J. Solid, State Chem.*, **104**, 437-452 (1993).

Chai B.H.T., Bustamante A.N.P., Chou M.C., *Proc. 2000 IEEE/EIA Int. Freq. Control Symp. Exhib.*, 163-168 (2000).

Chi L. S., Zhou L. F., Chen H. Y., Zhang H. H., and Huang J. S., *Jiegon Huaxue*, 16(3) 219-222 (1997).

Clark B. L., Keszler D. A., *Inorg. Chem.* **40**, 1724 (2001).

Cox P. A., *The Electronic Structure and Chemistry of Solids* (Oxford University Press, Oxford, 1987).

Dong Li, *Ph.D. Thesis*, Oregon State University, (1999).

Doumerc J.-P., Ammar A., Wichainchai M. P., and Hagenuller P., *J. Phys. Chem. Solids*, **48(1)**, 37-43 (1987).

Draeseke A., Yanagi H., Tucker D., Easley D., McIntyre D. H., Tate J., Li J., Sleight A. W., Bull. Amer. Phys. Soc. 47 (2002) B23/13.

Duan N., Sleight A. W., Jayaraj M. K., and Tate J., *Appl. Phys. Lett.*, **77((9)**, 1325-1326 (2000).

Elazhari M., A. Ammar, M. Elaatmani, M. Trari, J. P. Doumerc, Eur. J. Solid State Inorg. Chem. 34 (1997) 503-509.

Geller S., *Acta Crystallogr., Sect. B* **27**, 821 (1971).

Gordon R. G., MRS Bull. **25**, 52 (2000).

Guseinov, G. G, Amiraslanov I. R., Kuliev A. S., Mamedov K. S., Izv. Akad. Nauk SSSR, Neorg. Mater., **23**, 854 (1987).

Hahn H., Angew. Chem., **65**, 538 (1953).

Hahn H. and Frank G., Naturwissenschaften, **44**, 533 (1957).

Hahn H., and Lorant C., *Z. Anorg. Allg. Chem.*, **279** 281-288 (1955).

Hahn H. and Klingler W., Z. Anorg. Allegm, Chem., **260**, 97 (1949).

Hahn H., and Kordes E., *Zeitschrift fur Kristallographie*, **129** 259-279 (1969).

Hoppe R., Schepers B., Roehrborn H. J., Vielhaber E., Z. Anorg. Allg. Chem. 339 (1965) 130-143.

Hubbert-Paletta E., Hoppe R., Kruezburg G., Z. Anorg. Allg. Chem. 379 (1970) 255-261.

Huster J.and Bronger W., Z. Anorg. Allg. Chem., **625**, 2033-2040 (1999).

Iglesias J. E., Pachali K. E., and Steinfink H., J. Solid State Chem. **9**, 6 (1974).

Ingram B. J., Mason T. O., Asahi R., Park K. J., and Freeman A. J., Phys. Rev. B: Condens. Matter Mater. Phys. **64**, 155114/1 (2001).

Ishibashi H., Shimomoto K., and Nakahigashi K., J. Phys. Chem. Solids, 1994, 55(9), 809-814.

Ishiguro T., Kitazawa A., Mizatani N., Kato M., J. Solid State Chem. **40**, 170 (1981).

Kanniainen T., Lindroos S., Prohaska T., Friedbacher G., Leskela M., Grasserbauer M., Niinisto L., *J. Mater. Chem*, **5(7)**, 985-989 (1995).

Kanniainen T., University of Helsinki, Faculty of Science, Department of Chemistry, Laboratory of Inorganic Chemistry, Helsinki, 2001.

Kawazoe H., Yasukawa M., Hyodo H., Kurita M., Yanagi H., and Hosono H., *Nature*, **389**, 939-942 (1997).

Keir P. D., Fabrication and Characterization of ACTFEL Devices, Ph. D. Dissertation, Oregon State University, 2000.

Klaska K. H., Eck J. C., andPohl D., Acta Cryst., 1978, B34, 3324-3325.

Koffyberg F. P. and Benko F. A., J. Appl. Phys., 53(2), 1173-1177 (1982).

Koretsky M., Electronic Material Processing, Class Notes, Fall, 1999.

Krakauer H., Posternak M., and Freeman A. J., Phys. Rev. B, **19(4)**, 1706 (1979).

Kudo A., Yanagi H., Hosono H., and Kawazoe H., *Appl. Phys. Lett.*, **73(2)**, 220-222 (1998).

Kumatoriya M., Sato H., Nakanishi J. Fujii T., Kadota M., Sakabe Y., J. Crystal Growth 229 (2001) 289.

Kuribayashi K., Yoshimura M, Ohta T., and Sata T., J. Am. Cerm. Soc. 1980, 61(11-12), 644-646.

Landuty J. van, Tendeloo G. van, and Amelinckx S., Phys. Status Solidi A, **26**, K99 (1975).

Lencka, M.M., Oledzka, M., Riman R., *Chem. Mater.*, 12, 1323 (2000).

Likforman A., Carre D., and Hillel R., Acta. Cryst. B, **34**, 1 (1978).

Likforman A., Fourcroy P., Guittard M., Flahaut J., Poirier R., and Szydio N., J. Solid State Chem., **33**, 91 (1980).

Likforman A., Messain D., Guittard M., and Flahaut J., C. R. Acad. Sci., 274, 378 (1972).

Lutz H. D., Fischer M., Baldus H.-P., and Blachnik R., J. Less-Common Met., **143**, 83 (1988).

Marinder D.-O., Wang P.-L., Werner P.-E., Westdahl M., Andresen A. F., and Louer D., *Acta Chemica Scandinavica A*, **41**, 152-157 (1987).

Marezio M., Acta Crystallogr. 18 (1965) 481-484; Mueller H., Hoppe R., Z. Anorg. Allg. Chem. 611 (1992) 73-80.

Martin U., Boysen H., Frey F., *Acta Crystallogr., Sect. B* **49**, 403 (1993).

Mattheiss L. F., *Phys Rev. B*, **48(24)**, 18300-18303 (1993).

Mayolet A., Krupa J.C., Gerard I., and Martin P., *Mater. Chem. Phys.*, 31, 107-109 (1992).

Mill B. V., Butashin A. V., Khodzhabagyan, Belokoneva E. L., Belov N. V., Doklady Akad. SSSR 264 (1982) 1385.

Miyazawa H. and Sugaike S., J. Phys.. Soc. Jpn., **12**, 312 (1957).

Monolikas C., J. Solid State Chem., 33, 91 (1980).

Morell A and El Khiati N., J. Electrochem. Soc., 140(7), 2019-2022 (1993).

Nagarajan R., Duan N., Jayaraj M. K., Li J., Vanaja K. A., Yokochi A., Draeseke A., Tate J., Sleight A. W., Internat. J. Inorg. Mater. 3 (2001) 265-270.

Newman P. C. and Redhill W., Z. Anorg. Chem., **299**, 158 (1959).

Nicolau Y. F. *Appl. Surf. Sci.*, **22/23**, 1061 (1985).

Nicolau Y. F., and Menard J. C., *J. Cryst. Growth*, **92**, 128 (1988).

Oishi K., Kobayashi S., Ohta S.-I., Tsuboi N., and Kaneko F., *J. Cryst. Growth*, **177**, 88-94 (1997); Oishi K., Kobayashi S., and Kaneko F., J *Cryst. Growth*, **153**, 158-163 (1995); Susaki M., Horinaka H., and Yamamoto N., *J. Appl. Phys.*, **30**, 2797-2801 (1991); Susaki M., Horinaka H., and Yamomoto N., *Jpn. J. Appl. Phys.*, **31(Pt. 1, No. 2A)**, 301-304 (1992).

Ohring M., The Materials Science of Thin films, Academic Press, 1992.

Ohtani T., Takeuchi H., Koh K., Kaneko T., J. Alloys Compd. **317/318**, 201 (2001).

Osamura K., Murakami Y., and Tomiie Y., J. Phys. Soc. Jpn., **21**, 1848 (1966).

Ozawa L., Forest H., Jaffe, P. M. and Ban G., J. Electrochem. Soc. 1971, 118(3), 482-486.

Pabst A., Amer. Mineralogist 23 (1938) 175-176.

Park G-T., Choi J-J, Ryu J, Fan H., and Kim H-E, *Appl. Phy. Lett.*, **80(24)**, 4606 (2002).

Park S., Keszler D. A., Valencia M. M., Hoffman R. L., Bender J. P., and Wager J. F., Appl. Phys. Lett., **80(23)**, 4393 (2002).

Parretta A., Jayaraj M. K., Nocera A. D., Loreti S., Quercia L., and Agati A., *Phys. Stat. Sol. (a)*, **155**, 399-404 (1996).

Popovic S., Celustka B., and Bidjin D., Phys. Status Solidi A, **6**, 301 (1971).

Popovic S., Tonejc A., Grzeta-Plenkovic B., Celustka B., and Trojko B., J. Appl. Cryst., **12**, 416 (1979).

Pisarevsky Yu V., Senyushenkov P. A., Mill B. V., Moiseeva, N. A., Proc. IEEE Freq. Control Symp. (1998) 742.

Ritala M., Kukli K., Rahtu A, Räisänen P. I., Leskelä M. , Sajavoara T., J. Keinonen, *Science* **288**, 319 (2001).

Russell P., Batchelor D., Thornton J., SEM and AFM: Complementary Techniques for High Resolution Surface Investigations, Digital Instruments.

Saeki M., Onada M., and Nozaki H., Mater. Res. Bull. **23**, 603 (1988).

Sandonnini C., Gazz. Chem. Ital. 44I (1914) 307.

Sato H., Minami T., Takata S., and Yamada T., *Thin Solid Films*, **236**, 27-31 (1993).

Sato J., Takeda H., Morikoshi H., Shimamura K., Rudolph P., Fukuda T., J. Crystal Growth 191 (1998) 746.

Semiletov S. A., Sov. Phys. Crystallogr., **5**, 673 (1961).

Semiletov S. A., Sov. Phys. Crystallogr., **6**, 158 (1961).

Shannon R. D., *Acta Crystallogr., Sect. A*, 32 751 (1976).

Shannon R. D., Prewitt C. T., Acta Crystallogr. Sect. B 25 (1969) 925-929.

Shannon R. D., Rogers D. B., and Prewitt C. T., *Inorg. Chem.*, **10(4)**, 713-718 (1971); Prewitt C. T., Shannon R. D., and Rogers D. B., *Inorg. Chem.*, **10(4)**, 719-723 (1971); Rogers D. B., Shannon R. D., Prewitt C. T., and Gillson J. L., *Inorg. Chem.*, **10(4)**, 723-727 (1971).

Shimode M., Sasaki M., Mukaida K., J. Solid State Chem. 151 (2000) 16-20.

Shimamura K., Takeda H., Kohno T., and Fukuda T., *J. Cryst. Growth*, **163**, 388-392 (1996).

Shimode M., Sasaki M., and Mukida K., J. *Solid. State. Chem.*, **151**, 16-20, (2000).

Shimamura K., Takeda H., Kohno T., Fikuda T., J. Crystal Growth 163 (1996) 388.

Shionoya S.and Yen W. M., *Phosphor Handbook*, CRC Press.

Shriver D. F., Atkins P., and Langford C. H., Inorganic Chemistry, Second Edition, Freeman.

Sleight A. W., Solid-State Chemistry, Class Notes, Spring, 1999.

Stauber R. E. Parilla., P. A, Perkins J. D., Grinley D. S., Mater. Res. Soc. Symp. Proc. **623**, 265 (2000).

Sun X. W. and Kwok H. S., Appl. Phys A, 69(Suppl.), S39-S43 (1999).

teXsan for Windows version 1.01. Single Crystal Structure Analysis Software. MSC, 3200 Research Forest Drive, The Woodlands, TX, 77381, USA.

Thomas Gordon, *Nature*, **389**, 907-908 (1997).

Thomas P. Niesen and Mark R. De Guire, *J. Electroceramics*, **6**, 169 (2001).

Ueda K., Inoue S., Hosono Hirose S., Kawazoe H., and Hosono., *Appl. Phys., Lett.*, **77(17)**, 2701-2703 (2000).

Ueda K., Inoue S., Hosono H., Sarukura N., and Hirano M., Appl. Phy. Lett., **78(16)**, 2333 (2001).

Ueda K., Hase T., Yanagi H., Kawazoe H., Hosono H., Ohta H., Orita M., and Hirano M., *J. Appl. Phys.*, **89(3)**, 1790-1793 (2001).

Walker N., Stuart D. Acta Crystallogr., Sect. A 39 (1983) 158.

West A. R., *Solid State Chemistry and its Applications*, John Wiley & Sons Ltd, Chapter 14, 1995.

Willardson R. K. and Beer A. C., *Semiconductors and semimetals*, (Academic, New York, 1967),Vol. 3, Chap. 6.

Wimmer E., Krakauer H., Weinert M., and Freeman A. J., Phys. Rev. B, **24(2)**, 864 (1981).

Yamada H., Kano T and Tanabe M., *Mat. Res. Bul.* 13 101-108 (1978).

Yanagi H., Hase T., Ibuki S., Ueda K., and Hosono H., *Appl. Phys. Lett.*, **78(11)**, 1583-1585 (2001).

Yanagi H., Inoue S., Ueda K., Kawazoe H., and Hosono H., *J. Appl. Phys.*, **88(7)**, 4159-4162 (2000).

Yanagi H., Kawazoe H., Kudo A., Yasukawa M., and Hosono H., *J. Electroceramics*, **4(2/3)**, 407-414 (2000).

Ye J., Soeda S., Nakamura Y., and Nittono O., Jpn. J. Appl. Phy., **37**, 4264 (1998).

Yoshiro M., Ma J., and Kakihana M., J. Am. Ceram. Soc., 1998, 81(10), 2721-2724.

Zhang X., Hogan T., Kannewurf C. R., and Kanatzidis M. G., *J Alloys Compd.*, **236**, 1-5 (1996).

Zhu W. Z., and Hor P. H., *Inorg. Chem,*, **36**, 3576-3577 (1997).

Zhu W. J., Huang Y. Z., Wu F., Dong C., Chen H., and Zhao Z. X., *Mat. Res. Bull.*, **29(5)**, 505-508 (1994).

APPENDICES

APPENDIX A. SILAR-DEPOSITED FILMS

As part of a general survey of the capabilities of the SILAR deposition method and in preparation for variety of research projects, thin films of the compounds CeO_2, MnO_2, Mn_2O_3, $Mn:Zn_2SiO_4$, $LaPO_4$, BaF_2, and Y_2O_3 have been make and characterized by X-ray diffraction. Experimental conditions and results for these depositions are summarized on the following pages.

The production for CeO_2 thin films using SILAR method

The selected conditions for production for CeO_2 (cubic) film are summarized.

Cation solution	0.01M $Ce(C_2H_3O_2)_31.5H_2O$ in 40ml, pH=5.10
Anion solution	0.01M NaOH in 40ml + 1ml 3% H_2O_2, pH=9.63
Immersion time	10 second
Rinsing time	10 second
Cycle numbers	100 + 100
Substrate	Si/SiO_2

After annealing at 600°C in air for 25 min + 25 min, the x-ray diffraction pattern reveals that the product has crystallized in cubic form of CeO_2.

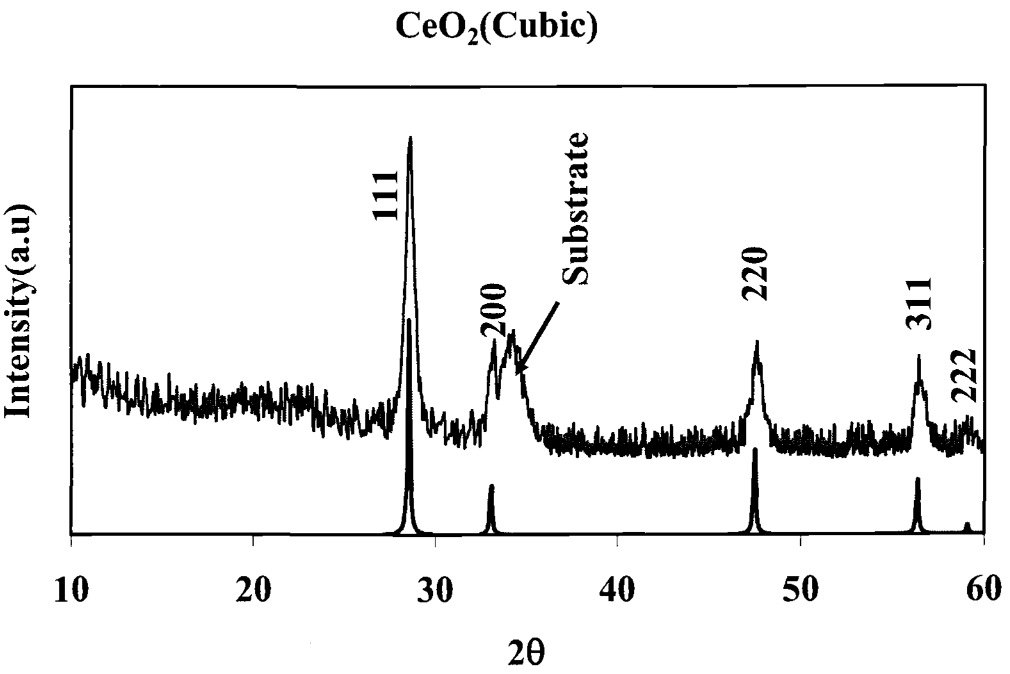

The selected conditions for production for CeO_2 (cubic) film are summarized.

Cation solution	0.06M $Ce(C_2H_3O_2)_3 1.5H_2O$ in 40ml, pH=5.07
Anion solution	0.06M NaOH in 40ml + 2ml 3% H_2O_2, pH=12.26
Immersion time	10 second
Rinsing time	10 second
Cycle numbers	200
Substrate	Si/SiO_2

Annealing: hydrothermal dehydration at 200°C for 15 h

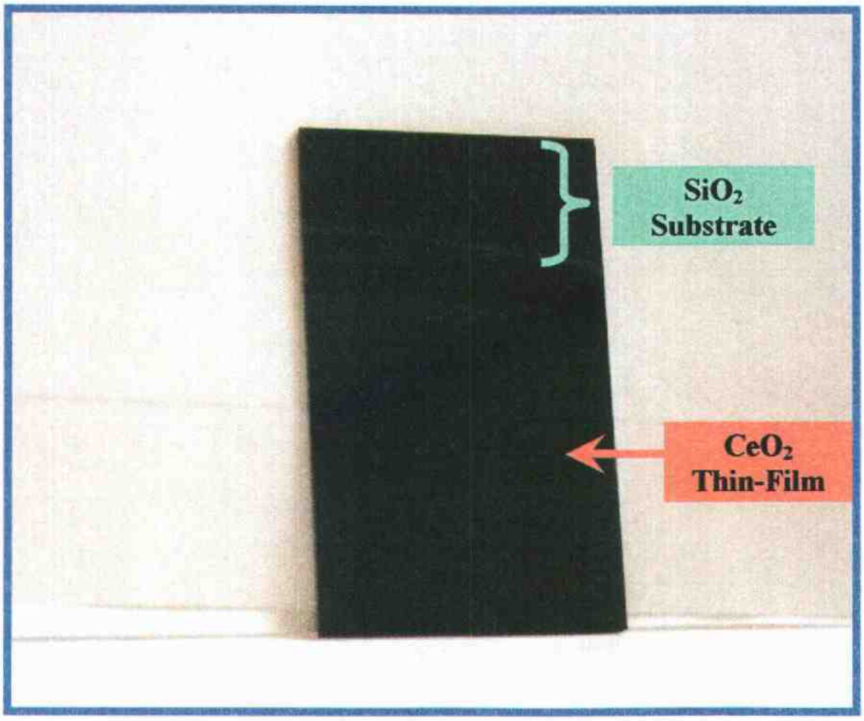

SEM images of CeO_2 thin film

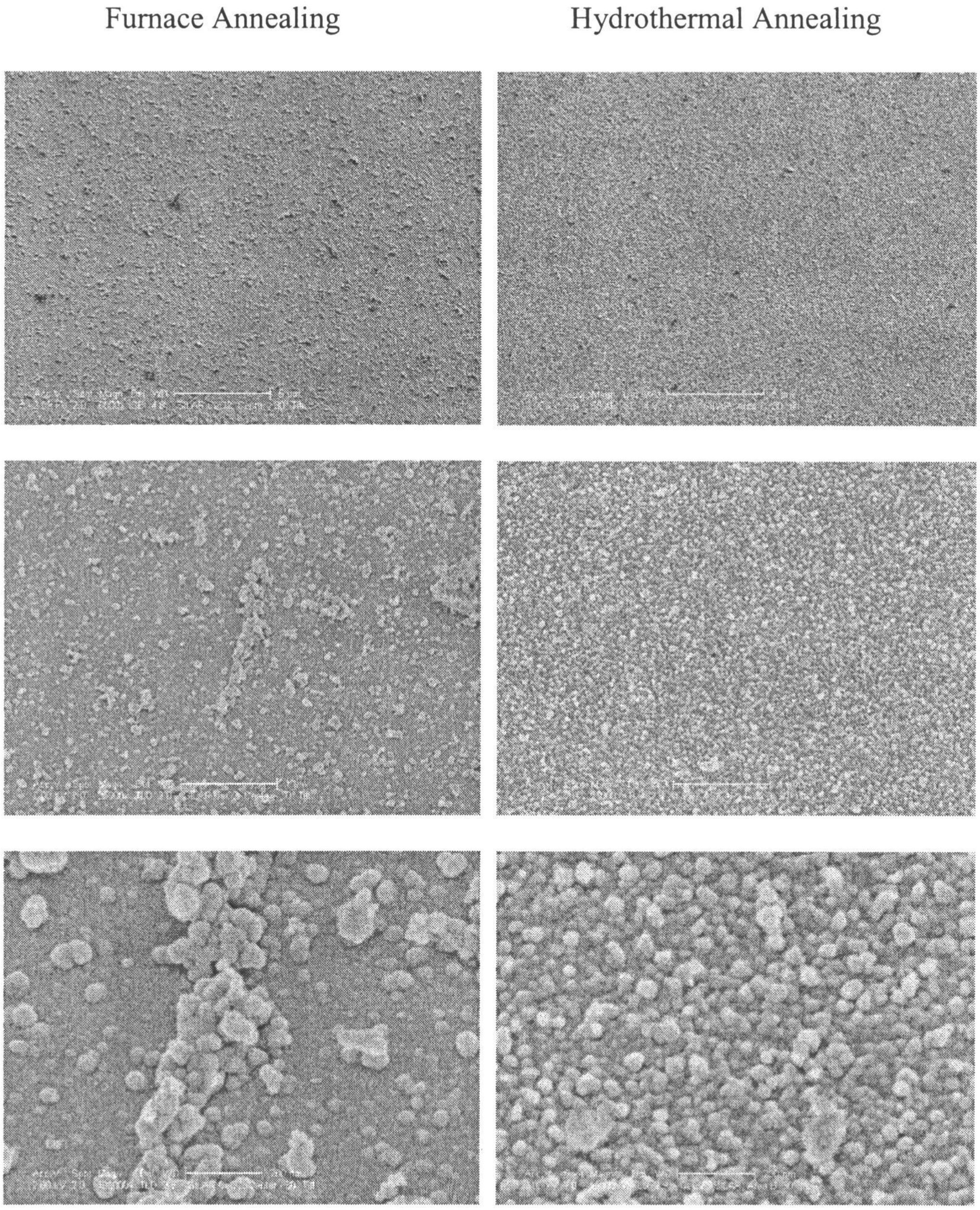

Furnace Annealing

Hydrothermal Annealing

The Production For Mn_2O_3 and MnO_2 Films Using SILAR Method

The selected conditions for production for Mn_2O_3 and MnO_2 films are summarized in Table.

Table. Deposition of Mn_2O_3 and MnO_2 on SiO_2/Si

Cation solution	0.06M $MnSO_4H_2O$ in 40ml, pH=3.77
Anion solution	0.06M NaOH in 40ml, pH=12.26 5ml 30% H_2O_2 was added.
Immersion time	10 second
Rinsing time	30 second
Cycle numbers	700
Substrate	SiO_2/Si

Reagents:

$MnSO_4H_2O$ (Alfa, 98.0-101.0%)

NaOH (Mallinckrodt, Analytical Reagent)

30%H_2O_2 (Mallinckrodt, Analytical Reagent)

1. Following the furnace anneal at 500°C for 1h, the X-ray diffraction pattern reveals that the product has crystallized in cubic form of Mn_2O_3.

Mn_2O_3(Cubic)

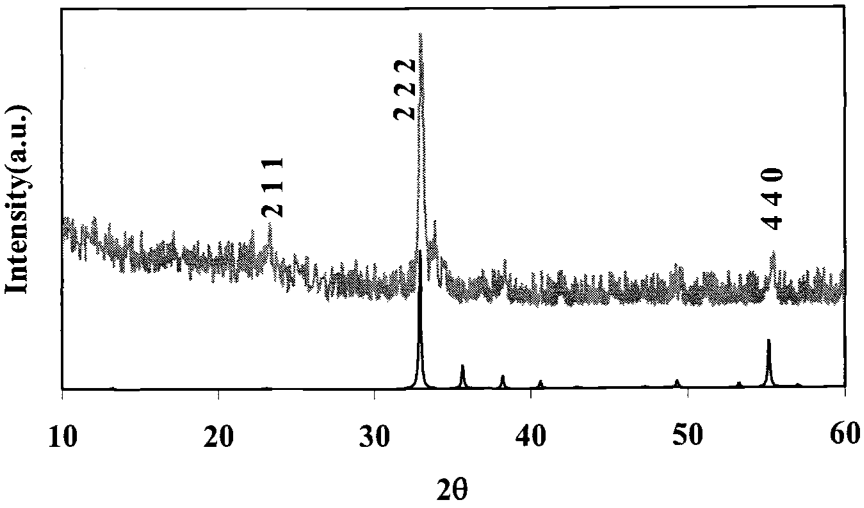

2. Treating the as-deposited film in a closed Teflon container with three drops of water at 200°C results in the crystallization of tetragonal MnO_2 phase. X-ray diffraction of MnO_2 on SiO_2/Si substrate was shown in Figure.

MnO_2(Tetragonal)

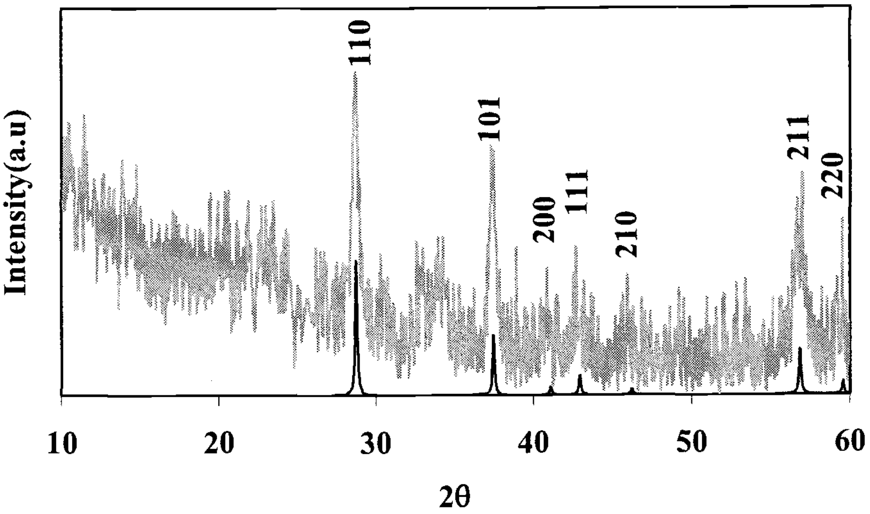

Luminescence of $Mn:Zn_2SiO_4$ Thin Films Using SILAR Method

The selected conditions for production for $Mn:Zn_2SiO_4$ (trigonal) film are summarized.

Cation solution	0.1M 30ml $ZnSO_47H_2O$ + 0.1M 5ml $MnSO_4H_2O$
Anion solution	0.1M Na_4SiO_4 in 40ml
Immersion time	10 second
Rinsing time	10 second
Cycle numbers	700
Substrate	Si/Si_3O_4

After annealing at 1000°C in air, the x-ray diffraction pattern reveals that the product has crystallized in trigonal form of Zn_2SiO_4.

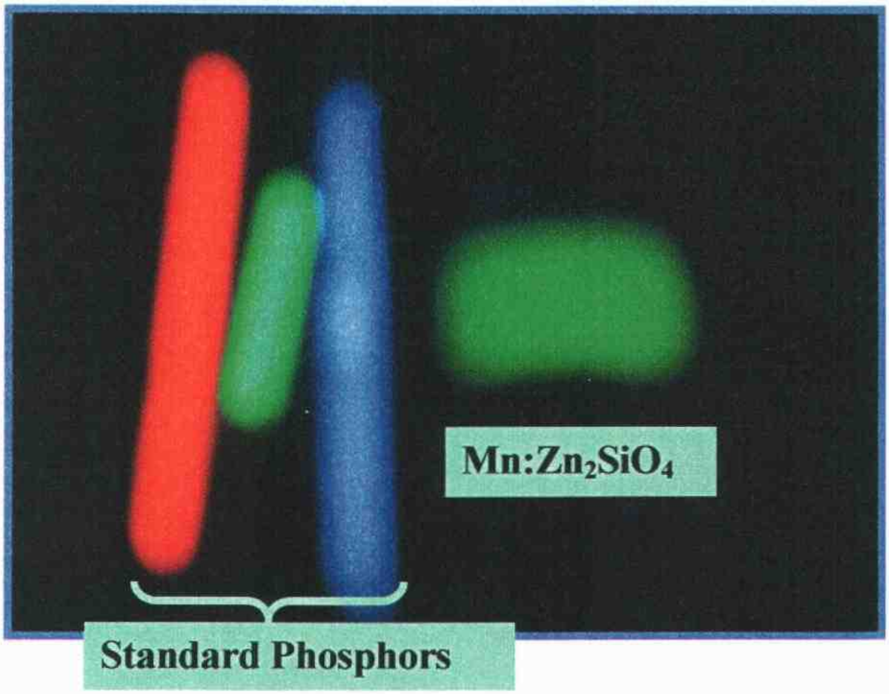

The Production for $LaPO_4$ Films Using SILAR Method

The selected conditions for production for $LaPO_4$ (hexagonal) film are summarized.

Cation solution	0.01M $La(NO_3)_3$ in 40ml
Anion solution	0.01M Na_2HPO_4 in 40ml
Immersion time	10 second
Rinsing time	10 second
Cycle numbers	700
Substrate	Si/SiO_2

After annealing around 150°C in air, the x-ray diffraction pattern reveals that the product has crystallized in hexagonal form of $LaPO_4$.

$LaPO_4$ (Hexagonal)

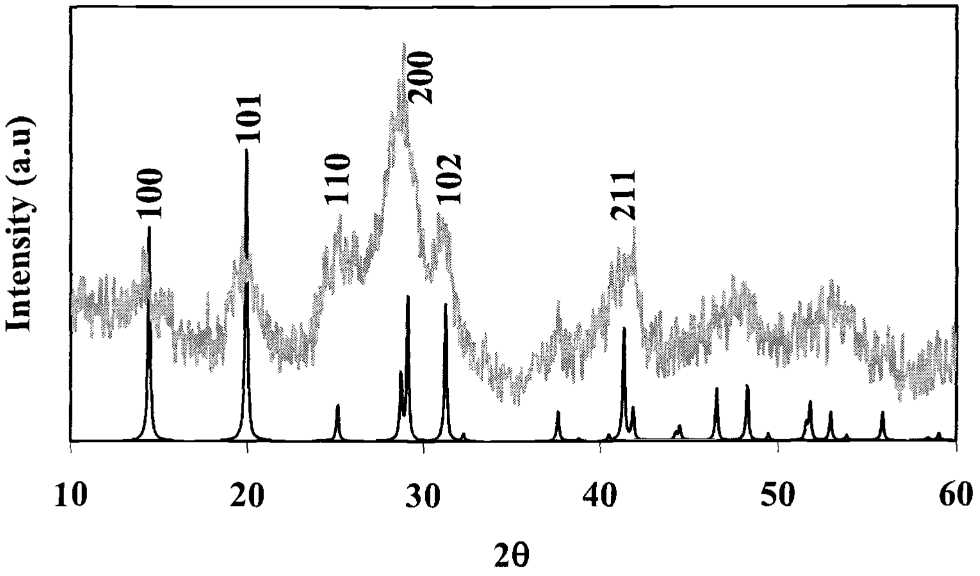

The selected conditions for production for $LaPO_4$ (monoclinic) film are summarized.

Cation solution	0.5M $La(NO_3)_3$ in 40ml
Anion solution	0.5M Na_2HPO_4 in 40ml
Immersion time	10 second
Rinsing time	10 second
Cycle numbers	700
Substrate	Si/SiO_2

For hydrothermal dehydration annealing at 200°C for 1 d, the x-ray diffraction pattern reveals that the product has crystallized in monoclinic form of $LaPO_4$.

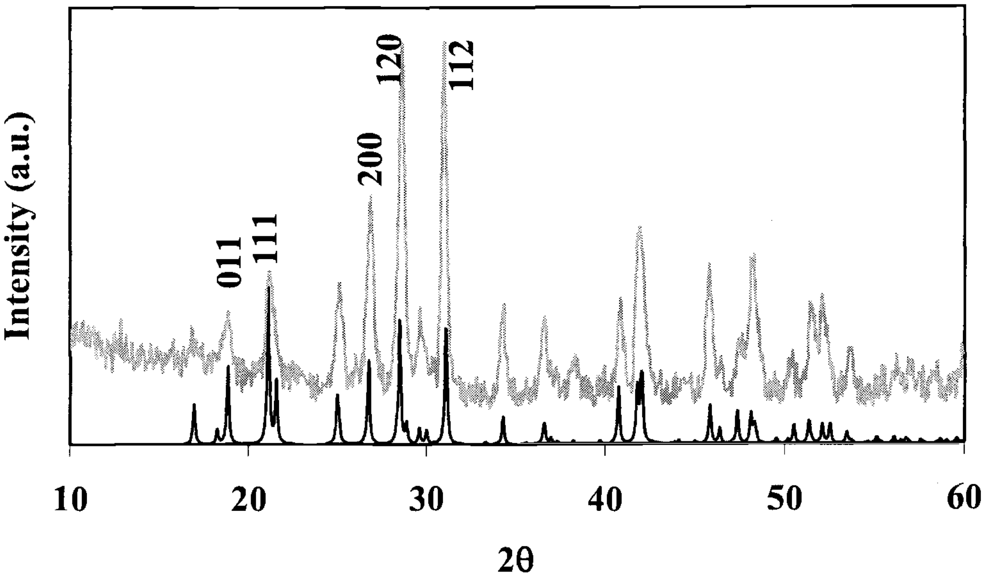

$LaPO_4$ (Monoclinic)

The Production for Y_2O_3 Film Using SILAR Method

The selected conditions for production for Y_2O_3 film are summarized.

Cation solution	0.06M $Y(NO_3)_3$ in 40ml, set pH=5.80
Anion solution	0.06M NaOH in 40ml, pH=12.26
Immersion time	10 second
Rinsing time	10 second
Cycle numbers	700
Substrate	Si/SiO_2

After annealing at 600°C for 2 h in air, the x-ray diffraction pattern reveals that the product has crystallized in cubic form of Y_2O_3.

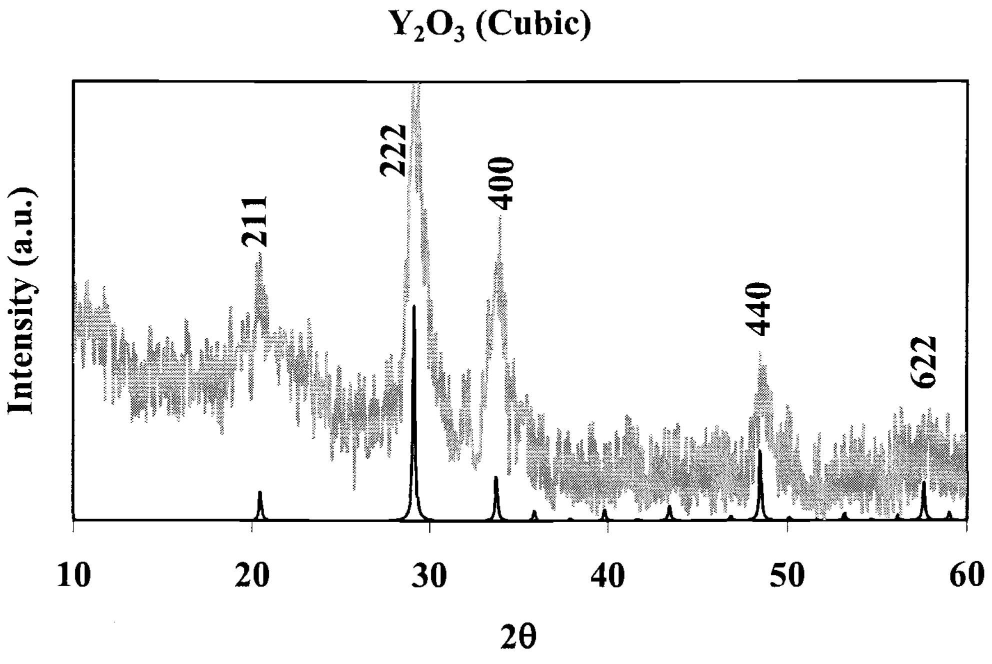

Future work: Eu-doped Y_2O_3 (red luminescence thin films)

The Production for BaF_2 Film Using SILAR Method

The selected conditions for production for BaF_2 film are summarized.

Cation solution	0.5M $Ba(NO_3)_2$ in 40ml
Anion solution	1M NaF in 40ml
Immersion time	10 second
Rinsing time	10 second
Cycle numbers	700
Substrate	Glass

For drying in air, the x-ray diffraction pattern reveals that the product has crystallized in cubic form of BaF_2.

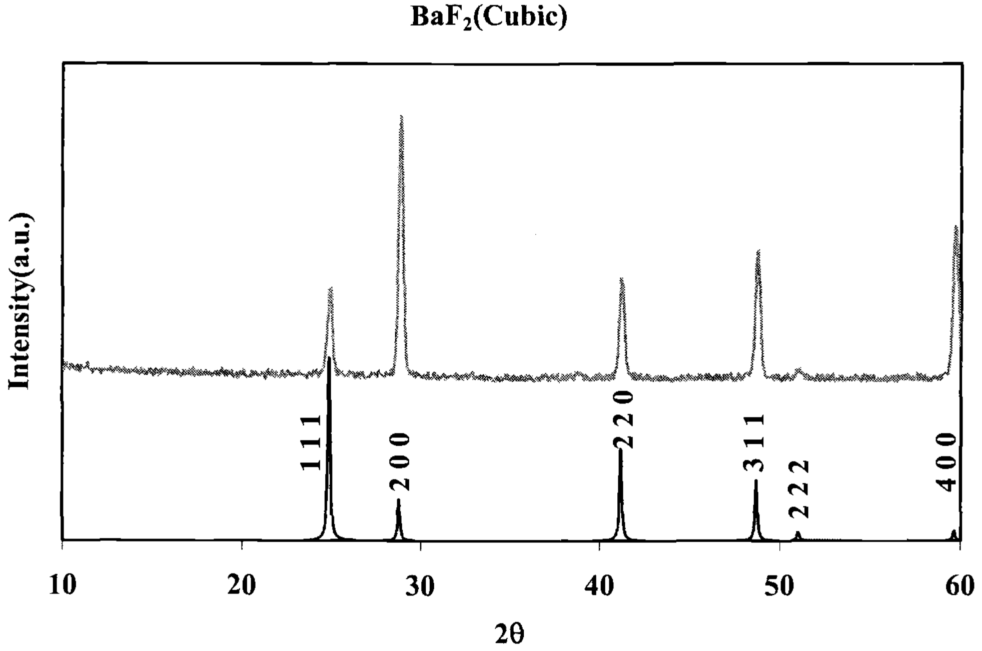

Future work: multi layer thin films and BaCuSF thin film.

ZrO_2 Photography

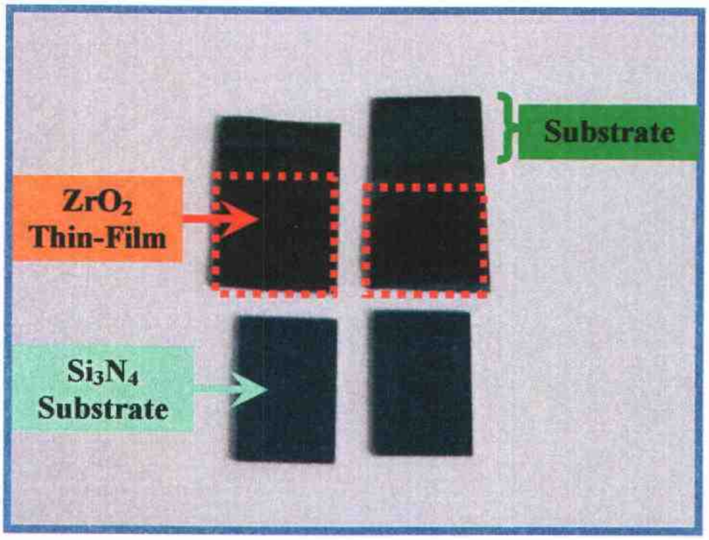

APPENDIX B. Unfinished $Sr_3MgSi_2O_8$ Project

The powdered samples of $Sr_{3-x}Eu_xMgSi_2O_8$ (x = 0, 0.04) and $Sr_{2.55-x}Eu_xBa_{0.45}Si_2O_8$ ($0 < x \leq 0.1$) were prepared by heating the reagents $SrCO_3$ (Aldrich, 99.995%), $Mg(NO_3)_2xH_2O$ (Alfa 99.999%), and SiO_2 (Alfa 99.99%) in the correct molar ratios. 0.4mol% NH_4Cl was used to promote phase formation. A series of grinding and heating steps was executed and final anneals at 1473 K for 2 h for $Sr_3MgSi_2O_8$ and at 1423 K for 1d under 2%H_2-98%Ar gas for Eu^{2+}-doped compounds. The crystal of $Sr_3MgSi_2O_8$ was grown in an alumina crucible by mixing and heating with 33-wt% NaF. The melt was cooled from 1423 to 1133 K at 6 K/h and then to room temperature by turning off the power to the furnace.

Luminescence

Emission Spectra of $Sr_{2.55-x}Ba_{0.45}Eu_xMgSi_2O_8$ (x = 0.02 ~ 0.10) and $Sr_{2.96}Eu_{0.04}MgSi_2O_8$

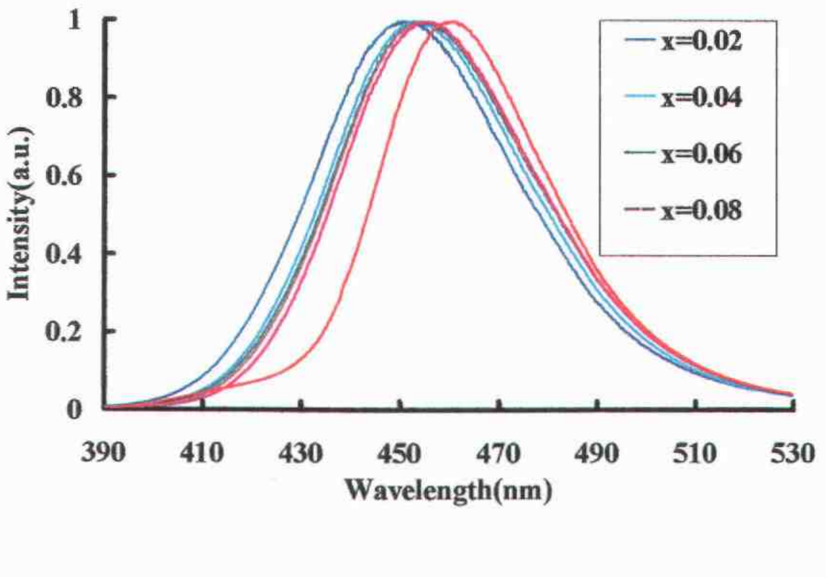

APPENDIX C. VITA

Education

Ph.D. Chemistry and Materials Science, Oregon State University, July 2002

M.S. Chemistry, Inje University, Korea, February 1996

B.S. Chemistry, Inje University, Korea, August 1993

Experience

Graduate Research Assistant

Oregon State University-Hewlett-Packard

Description: Materials development and study of wide band-gap semiconductors

Description: Application of SILAR/hydrothermal dehydration to preparation of oxide thin films

Oregon State University

Description: p-type Transparent Semiconductor Research

Graduate Teaching Assistant, Oregon State University, Department of Chemistry

Publications

1. **Sangmoon Park, Benjamin L. Clark, Douglas A. Keszler, Jeffry Bender, John F. Wager, and Gregory Herman, "Low-Temperature Thin-Film Deposition and Crystallization", *Science*, 297, 65(2002).**
2. Sangmoon Park, Douglas A. Keszler, Melinda Valencia, Randy Hoffmann, Jeffrey P. Bender and John F. Wager, "Transparent p-type conducting $BaCu_2S_2$ films", *Appl. Phys. Lett.*, **80(23)**, 4393 (2002).
3. Sangmoon Park and Douglas A. Keszler "Cation Ordering in Langasite Structure types", *Solid-State Science*, **4(6)**, 799 (2002).
4. Sangmoon Park and Douglas A. Keszler, "Synthesis of 3R-$CuMO_{2+\delta}$ (M = Ga, Sc, In)", J. Solid State Chem., submitted.
5. Sangmoon Park, Alexandre Yokochi, and Douglas A. Keszler, "Structure and luminescence properties of Yttrium Chloroorthosilicate, $Y_3(SiO_4)_2Cl$", Materials Research Bulletin, submitted.